



**Low energy electron-induced reactions
of model compounds for nano-scale
fabrication and for application in
chemoradiotherapy**

Maicol Cipriani



**Faculty of Physical Sciences
University of Iceland
2022**

Low energy electron-induced reactions of model compounds for nano-scale fabrication and for application in chemoradiotherapy

Maicol Cipriani

Dissertation submitted in partial fulfillment of a
Philosophiae Doctor degree in Chemistry

Supervisor
Prof. Oddur Ingólfsson

Doctoral Committee
Dr. Ragnar Björnsson
Prof. Armin Gölzhäuser

Opponents
Prof. Janina Kopyra
Dr. Márcio Teixeira do Nascimento Varela

Faculty of Physical Sciences
School of Engineering and Natural Sciences
University of Iceland
Reykjavik, June 2022

Low energy electron-induced reactions of model compounds for nano-scale fabrication and for application in chemoradiotherapy
(Low energy electrons in nanotechnology and cancer therapy)

Dissertation submitted in partial fulfillment of a *Philosophiae Doctor* degree in Chemistry

Faculty of Physical Sciences
School of Engineering and Natural Sciences
University of Iceland
Dunhaga 3
107 Reykjavik
Iceland

Telephone: 525-4000

Bibliographic information:

Maicol Cipriani (2022) *Low energy electron-induced reactions of model compounds for nano-scale fabrication and for application in chemoradiotherapy*, PhD dissertation, Faculty of Physical Sciences, University of Iceland, 119 pp.

ISBN 978-9935-9647-6-2

Copyright © 2022 Maicol Cipriani

Printing: XXPrinter
Reykjavik, Iceland, June 2022

Abstract

The interaction of low-energy electrons (LEEs) with neutral molecules plays an important role in various applications. In focused electron beam induced deposition (FEBID), a direct-write 3D nanofabrication technique, a high-energy focused electron beam is used to induce nanostructured deposition from precursor molecules (usually organometallic complexes) adsorbed onto a surface. At the current stage, this technique faces some challenges in regard to deposit purity and resolution. These limitations are mainly attributed to the low-energy secondary electrons generated by the impact of the primary electron beam on the surface. They are emitted with a large spatial distribution and can initiate electron-induced reactions that lead to incomplete fragmentation of the precursor molecules.

Low-energy electron interactions are expected to play an important role also in chemoradiotherapy, i.e., concomitant chemotherapy and radiotherapy. In this cancer treatment, radiosensitizing agents are used to sensitize cancer cells to radiation. It has been shown that LEEs, generated by the interaction of ionizing radiation with biological tissues, can interact with a radiosensitizer producing radicals that can induce DNA damage.

In order to improve the performance of FEBID precursors and radiosensitizers, it is important to study the energy dependence of the electron-induced processes.

Low-energy electrons (LEEs) can induce fragmentation through four distinct processes: dissociative electron attachment (DEA), dissociative ionization (DI), dipolar dissociation (DD) and neutral dissociation (ND). Low-energy electron interactions are commonly investigated in gas phase experiments, under single electron-molecule collision conditions, with crossed molecular/electron beam instruments.

In this Ph.D. project, the LEE-induced decomposition of FEBID precursors and some model compounds for application in chemoradiotherapy was investigated in the gas-phase, specifically focusing on DEA and DI processes.

The FEBID precursors that have been selected for this work are $(\eta^3\text{-C}_3\text{H}_5)\text{Ru}(\text{CO})_3\text{Br}$ and $\text{cis-Pt}(\text{CO})_2\text{Br}_2$. For $(\eta^3\text{-C}_3\text{H}_5)\text{Ru}(\text{CO})_3\text{Br}$, an extensive DI study was conducted as a follow-up of previous studies of this compound. For $\text{cis-Pt}(\text{CO})_2\text{Br}_2$, both DEA and DI were investigated, with more emphasis on DEA, and the results were compared with previous gas-phase DEA studies on $\text{cis-Pt}(\text{CO})_2\text{Cl}_2$ and $\text{cis-Pt}(\text{NH}_3)_2\text{Cl}_2$, with surface studies on $\text{cis-Pt}(\text{CO})_2\text{Cl}_2$ and with FEBID experiments on $\text{cis-Pt}(\text{CO})_2\text{Br}_2$ and $\text{cis-Pt}(\text{CO})_2\text{Cl}_2$.

With the aim of enhancing the susceptibility of radiosensitizers towards LEEs, extensive DEA studies on the model compounds pentafluorothiophenol, 2-fluorothiophenol and pentafluorobenzoic acid, were conducted, where we explored the perfluorination and neutral HF formation as potential means to promote DEA reactions. The results were compared with previous work on DEA to pentafluorophenol and benzoic acid.

Útdráttur

Vixverkun lagorkurafeinda (LEEs) við óhlaðnar sameindir er mikilvæg á mörgum sviðum. Örprenntun með skörpum rafeindageisla (en: focused electron beam induced deposition (FEBID)) er eitt slíkt, en það eru útbúnir strúktúrar á nanómetraskala úr undanfarasameindum, sem eru yfirleitt á formi lífrænna málmkomplexa, sem eru aðsogaðir á yfirborð. Á núverandi stigi stendur þessi tækni frammi fyrir áskorunum hvað varðar hreinleika og upplausn. Þessar áskoranir eru aðallega raktar til óæskilegra lagorkurafeinda sem myndast þegar háorku rafeindageisli fellur á yfirborð. Óæskilegu rafeindirnar dreifast vítt og breytt og geta framkallað óæskileg hliðarhvorf og niðurbrots undanfarasameindanna.

Víxlverkun lágorkurafeinda getur einnig gegnt mikilvægu hlutverki í geislalyfjameðferð krabbameins, en þá eru geislanæmisefni notuð til þess að gera krabbameinsfrumur næmari fyrir geislun. Sýnt hefur verið fram á að víxlverkun lágorkurafeinda, sem myndast við samspil jonandi geislunar við líkamsvefi, við geislanæmisefni getur mynað sindurefni sem aftur geta valdið DNA skemmdum.

Til þess að bæta FEBID undanfarasameinda og geislanæmisefna er mikilvægt að rannsaka hvernig fareinda drifin sundrun þeirra er háð orku. Lagorkurafeindir geta framkallað sundrun með fjórum mismunandi ferlum: Rjúfandi rafeindaralagningu (en: dissociative electron attachment (DEA)), rjúfandi jónun (en: dissociative ionization (DI)), tvískautsrof (en: dipolar dissociation (DD)) eða hlutlausu rofi (en: neutral dissociation (ND)). Lagorkurafeinda víxlverkanir hafa oft verið rannsakaðar í gasfasatílraunum við arekstra stakra rafeinda og sameinda, með tækjum þar sem sameinda- og rafeindageislar eru látnir skarast.

Í þessu doktorsverkefni er lágorkurafeinda framkallað niðurbrot FEBID undanfarasameind og nokkurra efnasambanda sem nýst gætu í frekari þróun geislalyfjameðferðar, skoðuð á gasformi. Sérstök áherslu rjúfandi rafeindaalagningu (DEA) og jufandi jónun (DI).

FEBID forverarasameindir sem hafa verið valdir fyrir þetta verkefni eru $(\eta^3\text{-C}_3\text{H}_5)\text{Ru}(\text{CO})_3\text{Br}$ og $\text{cis-Pt}(\text{CO})_2\text{Br}_2$. Fyrir $(\eta^3\text{-C}_3\text{H}_5)\text{Ru}(\text{CO})_3\text{Br}$ var gerð umfangsmikil rannsókn á sundrandi jónun í framhaldi af fyrri rannsóknum á þessu efnasambandi. Fyrir $\text{cis-Pt}(\text{CO})_2\text{Br}_2$ voru bæði sundrandi rafeindaalagning og sundrandi jónun skoðuð, með meiri áherslu á sundrandi rafeindaalagningu. Niðurstöðurnar bornar saman við fyrri gasfasa rannsóknir á $\text{cis-Pt}(\text{CO})_2\text{Cl}_2$ og $\text{cis-Pt}(\text{NH}_3)_2\text{Cl}_2$, rannsóknir á rafeindadrifnu niðurbroti á $\text{cis-Pt}(\text{CO})_2\text{Cl}_2$ á yfirborði fastefnis og FEBID þar sem $\text{cis-Pt}(\text{CO})_2\text{Br}_2$ og $\text{cis-Pt}(\text{CO})_2\text{Cl}_2$ voru notuð sem undanfarasameindir.

Með það að markmiði að auka næmni geislanæmisefna gagnvart lágorku rafeindum voru gerðar rannsóknir á efnasamböndunum pentafluorothiophenol, 2-fluorothiophenol og pentafluorobenzoic acid, þar sem könnuð notkun flúors og HF myndun sem hugsanlegar leiðir til að stuðla að sundrandi rafeindaalagningu. Niðurstöðurnar voru bornar saman

við fyrri rannsóknir á rafeindaálagningu á pentaflúorfenól og bensósýru.

To my family and to the love of my life.

*"You wanna know how I did it?
This is how I did it Anton. I never saved anything
for the swim back"*

Gattaca. Directed by Andrew Niccol, Columbia Pictures, 1997

*"To live, to err, to fall, to triumph,
to recreate life out of life."*

James Joyce, A Portrait of the Artist as a Young Man

*"My hand tore at the snake and tore in vain;
it did not tear the snake out of his throat.
Then it cried out of me: "Bite! Bite its head off! Bite!" "*

*Friedrich Nietzsche, Thus Spoke Zarathustra: A Book for All and None
Translated by Walter Kaufmann*

Contents

Abstract	iii
Útdráttur	v
Dedication	vii
Contents	ix
List of Figures	xiii
List of Tables	xv
List of Original Publications	xvii
Abbreviations	xix
Acknowledgments	xxi
1 Introduction	1
2 Theoretical Overview	5
2.1 Negative Ions: formation and decay	5
2.1.1 Autodetachment	8
2.1.2 Dissociative Electron Attachment	9
2.2 Classifications of Negative Ion resonances	10
2.2.1 Shape Resonances	10
2.2.2 Core-excited Feshbach resonances	11
2.2.3 Vibrational Feshbach resonances	12
2.3 Positive ions formation through Electron Impact	12
2.3.1 Ionization and appearance energy determination	13
3 Methods	15
3.1 Experimental setup	15
3.1.1 Normalization and appearance energies determination	17
3.2 Computational Methods	18
3.2.1 Hatree Fock (HF) method	19
3.2.2 Density Functional Theory	21
3.2.3 Time dependent density functional theory	21

3.2.4	Equation-of-motion coupled cluster theory	22
3.2.5	Thermochemical Threshold Calculations	22
3.2.6	Reaction path calculations	23
4	Results and Discussion	25
4.1	Low-energy interaction with focused electron beam induced deposition precursors	25
4.1.1	Motivation and Previous Work	25
4.1.2	Dissociative ionization of (η^3 -C ₃ H ₅)Ru(CO) ₃ Br	27
4.1.3	cis-Pt(CO) ₂ Br ₂ : dissociative electron attachment and dissociative ionization	31
4.2	Dissociative electron attachment to model compounds for application in chemoradiotherapy	36
4.2.1	Motivation and previous work	36
4.2.2	Comparison between Pt(CO) ₂ Br ₂ and Pt(NH ₃) ₂ Cl ₂ in DEA	38
4.2.3	HF formation from pentafluorothiophenol and 2-fluorothiophenol upon dissociative electron attachment	39
4.2.4	Dissociative electron attachment to pentafluorobenzoic acid	46
5	Summary and outlook	51
	References	52
	Article I	65
	Article II	73
	Article III	87
	Article IV	107

List of Figures

2.1	DEA quasi-diatomic model	7
3.1	Schematic of SIGMA	16
3.2	[RuCO ₂ Br] ⁺ formation ion yield fit	18
4.1	(η^3 -C ₃ H ₅)Ru(CO) ₃ Br	27
4.2	Positive mass spectrum of η^3 -C ₃ H ₅)Ru(CO) ₃ Br	27
4.3	Positive ion yield curves from (η^3 -C ₃ H ₅) Ru(CO) ₃ Br	28
4.4	Pt(CO) ₂ Br ₂	31
4.5	Negative ion yield for [Pt(CO)Br ₂] ⁻ and [PtBr ₂] ⁻	32
4.6	Fit of two Gaussian to [Pt(CO)Br ₂] ⁻ and [PtBr ₂] ⁻ ion yield curves	33
4.7	SOMO and SOMO+1 of [Pt(CO) ₂ Br ₂]	33
4.8	Positive ion mass spectrum of Pt(CO) ₂ Br ₂	34
4.9	PFTP and 2-FTP	39
4.10	Negative ion yields from PFTP	40
4.11	Negative ion yields from 2-FTP	41
4.12	PFTP rearrangement	42
4.13	LUMO and LUMO+1 of PFTP	44
4.14	Combined fit of a Gaussian and skewed Gaussian to the ion yield curve of [M – HF] ⁻ from DEA to PFTP	44
4.15	LUMO and LUMO+1 of 2-FTP	45
4.16	PFBA	46
4.17	Negative ion yields from PFBA	47
4.18	Combined fit of a Gaussian and skewed Gaussian to the ion yield curve for [M – HF – CO ₂] ⁻ formed upon DEA to PFBA	48
4.19	SOMO and SOMO+1 of PFBA	49
4.20	Optimized pentagonal structure of PFBA after HF loss upon DEA	49

List of Tables

4.1	Experimental AEs and the calculated threshold values for the DI of $\eta^3\text{-C}_3\text{H}_5\text{Ru}(\text{CO})_3\text{Br}$	29
4.2	VAEs for $\text{Pt}(\text{CO})_2\text{X}_2$ (X=F,Cl,Br,I).	34
4.3	Relative fragment contributions in DI and DEA to $\text{Pt}(\text{CO})_2\text{Br}_2$	35
4.4	Calculated thresholds in DEA to PFTP and 2-FTP	42
4.5	Calculated thresholds for DEA to PFBA	49

List of Original Publications

- Article I:** **Dissociative ionization of the potential focused electron beam induced deposition precursor π -allyl ruthenium(II) tricarbonyl bromide, a combined theoretical and experimental study**
Maicol Cipriani, Rachel M. Thorman, Christopher R. Brewer, Lisa McElwee-White and Oddur Ingólfsson
The European Physical Journal D, 2019, 73, 227
- Article II:** **The Role of Low-Energy Electron Interactions in cis-Pt(CO)₂Br₂ Fragmentation**
Maicol Cipriani, Styrmir Svavarsson, Filipe Ferreira da Silva, Hang Lu, Lisa McElwee-White and Oddur Ingólfsson
International Journal of Molecular Sciences, 2021, 22(16), 89984
- Article III:** **HF Formation through Dissociative Electron Attachment—A Combined Experimental and Theoretical Study on Pentafluorothiophenol and 2-Fluorothiophenol**
Maicol Cipriani and Oddur Ingólfsson
International Journal of Molecular Sciences, 2022, 23(5), 2430
- Article IV:** **HF and CO₂ loss from pentafluorobenzoic acid upon Dissociative Electron Attachment.**
Maicol Cipriani and Oddur Ingólfsson
Submitted to International Journal of Molecular Sciences for possible open access publication

Publications not included in the thesis:

- Article V:** **The role of the dihedral angle and excited cation states in ionization and dissociation of mono-halogenated biphenyls; a combined experimental and theoretical coupled cluster study**

Michael Barclay, Ragnar Björnsson, Maicol Cipriani, Andreas Terfort, D. Howard Fairbrother and Oddur Ingólfsson
Physical Chemistry Chemical Physics, 2019, 21, 4556-4567

Article VI: Relative cross sections and appearance energies in electron impact ionization and dissociation of mono-halogenated biphenyls

Maicol Cipriani, Ragnar Björnsson, Michael Barclay, Andreas Terfort, D. Howard Fairbrother and Oddur Ingólfsson
International Journal of Mass Spectrometry, 2021, 459, 116452

Article VII: Extreme Ultraviolet-Printability and Mechanistic Studies of Engineered Hydrogen Silsesquioxane Photoresist Systems

Ashish Rathore, Ivan Pollentier, Maicol Cipriani, Harpreet Singh, Danilo De Simone, Oddur Ingólfsson, and Stefan De Gendt
CS Applied Polymer Materials, 2021, 3, 4, 1964–1972

Article VIII: Electron-induced fragmentation mechanisms in organic monomers and their implications on photoresist optimization for EUV Lithography

Ashish Rathore, Maicol Cipriani, Ching-Chung Huang, Lionel Amiaud, Céline Dablemont, Anne Lafosse, Oddur Ingólfsson, Danilo De Simone and Stefan De Gendt
Physical Chemistry Chemical Physics, 2021, 23, 9228-9234

Article IX: Low-energy electron interaction and focused electron beam-induced deposition of molybdenum hexacarbonyl ($\text{Mo}(\text{CO})_6$)

Po-Yuan Shih[‡], Maicol Cipriani[‡], Christian Felix Hermanns, Jens Oster, Klaus Edinger, Armin Götzhäuser and Oddur Ingólfsson

Beilstein Journal of Nanotechnology. 2022, 13, 182–19

[‡] Equal contributors

Article X: Dissociative ionization and electron beam induced deposition of Tetrakis(dimethylamino)silane, a precursor for silicon nitride deposition

Po-Yuan Shih, Reza Tafrishi, Maicol Cipriani, Christian Felix Hermanns, Jens Oster, Armin Götzhäuser, Klaus Edinger and Oddur Ingólfsson

Physical Chemistry Chemical Physics, 2022, 24, 9564-9575

Abbreviations

2-FTP	2-flurothiophenol
AD	Autodetachment
AE	Appearance energy
BA	Benzoic acid
DD	Dipolar dissociation
DEA	Dissociative electron attachment
DFT	Density functional theory
DI	Dissociative ionization
DLPNO-CCSD(T)	Domain-based local pair natural orbital coupled cluster theory with perturbative triple excitations
EA	Electron affinity
EOM-EA-CCSD	Electron attachment equation of motion coupled cluster
EOM-CC	Equation of motion coupled cluster
FCF	Frank-Condon factor
FEBID	Focused electron beam induced deposition
FWHM	Full width at half maximum
HF	Hartree Fock
IE	Ionization energy
IVR	Intramolecular vibrational energy distribution
LEE	Low-energy electron
LUMO	Lowest-unoccupied molecular orbital
MO	Molecular orbital
ND	Neutral dissociation
NEB-TS	Nudged elastic band method with transition state optimization
NI	Negative ion
PFBA	Pentafluorobenzoic acid
PFP	Pentafluorophenol
PFTP	Pentafluorothiophenol
SOMO	Single occupied molecular orbital
TDDFT	Time-dependent density functional theory
TNI	Transient negative ion
VFR	Vibrational Feshbach resonance
ZPVE	Zero-point vibrational energy

1 Introduction

I remember that in my youth I had a book entitled “Chemistry, the nature changes itself”. That title suggests chemistry investigates the transformations of matter, its structure and composition. Historically, chemistry has seen a lot of evolutions. Modern chemistry endeavors to understand the structure and transformations of matter at the atomic and molecular levels. To this end, the study of the electron-molecule interactions is a matter of great importance. In fact, low energy electrons (LEEs) can cause significant structural changes and transformations in molecules [1; 2]. In my thesis, I focus on the role of LEEs in focused electron beam induced deposition (FEBID) and chemoradiotherapy. These two apparently different fields have in common the LEEs generated by irradiation. In FEBID, precursor molecules (usually organometallic complexes), physisorbed onto a surface, are exposed to a focused high energy electron beam [3–5]. Electron-molecule interactions induce their fragmentation, leading to nanostructured deposition. In an ideal case, this technique can give pure deposits of the target metal with high spatial resolution [6]. In practice, the depositions are limited in purity and resolution. These limitations have been attributed to the dissociation of precursor molecules induced by the interactions with LEEs generated by the inelastic scattering of primary electrons (PEs) [7]. Therefore, in order to improve the performance of FEBID precursors, it is crucial to investigate the physical chemistry behind LEE interactions with these compounds through gas-phase experiments in comparison with surface science studies [7].

In chemoradiotherapy, i.e. the concomitant administration of chemical radiosensitizers and radiotherapy, LEEs are expected to play an important role in sensitizing cancer cells to radiation through their reactions with the respective radiosensitizers. Similar to FEBID, the interaction of ionizing radiation with biological tissues generates a lot of LEEs with energy distribution peaking at or below 10 eV and with appreciable contribution close to 0 eV [8]. Before solvation, LEEs may interact with radiosensitizers generating radical species that can damage DNA.

Over the last few years, several studies have been conducted on LEE interactions with DNA and radiosensitizers [9–15]. In particular, it has been found that LEEs interactions with halogenated radiosensitizers play a central role in enhancing the cancer-killing effect of radiotherapy. Therefore, a radiosensitizer designed in such a way to be more susceptible to electron-induced reactions may be more efficient.

Other than in FEBID and chemoradiotherapy, LEEs interactions with molecules are of central importance also in many other fields, such as astrochemistry [16], plasma processing [17] and cancer treatment [18]. LEEs can induce fragmentation through four distinct processes: dissociative electron attachment (DEA), dissociative ionization (DI), neutral dissociation (ND) and dipolar dissociation (DD) [1].

In the first place, the nature of these interactions depends on the energy of the incoming electron. DEA is generally active at low electron energies (< 20 eV), below the ionization limit of the target molecule. In this process, an electron attaches to the molecules producing a transient negative ion (TNI). TNIs are unstable and may decay through autodetachment (AD), i.e., by reemitting the attached electron, or by dissociating into an anionic fragment and one or more neutral species.

Generally, DEA processes have the highest cross-sections at electron energies close to 0 eV, where the electron attachment is most efficient. However, for DEA reactions involving a single bond rupture, the prerequisite for this process to occur close to 0 eV incident electron energy, is that the electron affinity of the charge retaining fragment must exceed the dissociation energy of the bond that is ruptured.

Dissociative electron attachment reactions can also involve molecular rearrangements and formation of new bonds. These processes may promote DEA reaction channels, otherwise inaccessible, by feeding additional energy to the system.

Dissociative ionization, on the other hand, takes place at electron energies at or above the ionization limit of molecules. At these energies, the impacting electron ionizes the molecule. If the collision occurs with sufficient energy, the ionized molecule dissociates into a cation and one or more neutral fragments.

An incoming electron, with energy above the first excitation energy of the molecule, can also induce an electronic excitation. The resulting excited molecule can dissociate into neutral fragments through ND or positive and negative ion fragments through DD. The current work investigated LEE interactions with FEBID precursors and model compounds for application in chemoradiotherapy.

In regard to LEE interactions with FEBID precursors, DI of the potential FEBID precursor η^3 -allyl ruthenium tricarbonyl bromide ($(\eta^3\text{-C}_3\text{H}_5)\text{Ru}(\text{CO})_3\text{Br}$) and DEA and DI of $\text{Pt}(\text{CO})_2\text{Br}_2$ were investigated.

The DI study on $(\eta^3\text{-C}_3\text{H}_5)\text{Ru}(\text{CO})_3\text{Br}$ is an extension of previous studies where DEA to this compound was studied in the details [19; 20] and compared with surface data [21]. In the current study, the appearance energies (AEs) are determined by fitting the DI relative cross section with a Wannier type function. These are then compared to theoretical values obtained from quantum chemical calculations. In chapter 4.1, the results of this study are presented and compared with previous work on this compound. For the study on $\text{Pt}(\text{CO})_2\text{Br}_2$, the relative DEA cross sections for the observed negative ion fragments and the positive ion mass spectrum at 70 eV incident electron energy were recorded. To aid the interpretation of the experimental data, the threshold energies were calculated and the nature of the SOMOs involved in the DEA processes was investigated. Additionally, the DEA and DI contributions were calculated for the individual fragmentation channels and the average CO and Br loss upon DEA and DI was estimated.

In the context of enhancing the susceptibility of radiosensitizers to DEA towards very low energy electrons, the effects of perfluorination and neutral HF formation in lowering the thermochemical DEA threshold to three model compounds were investigated: 2-fluorothiophenol (2-FTP), pentafluorothiophenol (PFTP) and pentafluorobenzoic acid (PFBA). In these studies, the relative DEA cross sections for the observed fragmentation channels were recorded and the thermochemical thresholds were calculated. In addition,

the nature of the molecular orbitals involved in the DEA processes was investigated. For 2-FTP and PFTP, the minimum energy path for the HF formation upon DEA was computed. The thesis is organized as follow. In chapter II, a detailed overview of the fundamental principles behind these electron-molecule interactions in the gas phase is given. In Chapter 3, the experimental setup and the main computational methods used for quantum chemical calculations are discussed. In Chapter 4.1, the results of the DI study on (η^3 -C₃H₅)Ru(CO)₃Br are presented. These are compared with surface data [21] and a DEA and DI study on Pt(CO)₂Br₂ as well as with previous surface science, FEBID studies on Pt(CO)₂Br₂ and Pt(CO)₂Cl₂ [22; 23] and with a previous study on DEA to Pt(CO)₂Cl₂ [24]. In Chapter 4.2, the results of the studies on PFTP, 2-FTP and PFBA are presented and compared with previous studies on HF formation upon DEA to pentafluorophenol (PFP) [25; 26] and DEA to benzoic acid (BA) [27]. In this chapter, a comparison with DEA to cisplatin (cis-Pt(NH₃)₂Cl₂) [28] is also offered,- widely used chemotherapeutic agent also in the concomitant administration of radiotherapy.

2 Theoretical Overview

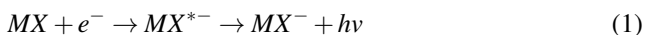
2.1 Negative Ions: formation and decay

Gas-phase negative ions (NIs) commonly occur during the interaction of low energy electrons (LEE, energy <15 eV) with gas-phase molecules. The formation of negative ions and their chemical reactions are relevant in a wide area of science and technologies, including fundamental atomic molecular processes (such as thermonuclear reaction [29; 30], plasma generation [31]), nanofabrication [7], cancer research/radiation damage studies [32; 33] and controlled tandem accelerators [34].

When a LEE attaches to an isolated molecule (MX) in the gas-phase, it forms a Transient Negative Ion (TNI), also called resonance because this is not a continuous process but occurs only within certain electron energy ranges [35; 36; 2]; i.e., a transition from a continuum state to a discrete state of the TNI.

An important parameter that determines the formation of a thermodynamically stable negative ion (MX^-) is the electron affinity (EA) of its neutral parent molecule. It is defined as the energy difference between the ground state of a neutral molecule and the ground state of its corresponding anion.

In order to form a thermodynamically stable negative ion (through non-dissociative electron attachment), the EA of the neutral molecule must be positive. However, a TNI is generally formed in an excited state (vibrational or electronic); therefore, the formation of a stable negative ion is only realized after the excess energy is released through radiation or by collision with a third body. In the interstellar medium negative molecular ions are generally formed through radiative attachment. In this process, the excess energy is released as radiation:

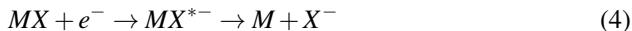
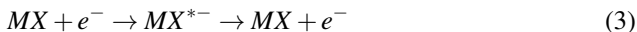


where MX^{*-} is the TNI formed in a vibrational or electronic excited state. The longest wavelength of the emitted radiation is given by:

$$\lambda = \frac{hc}{EA} \quad (2)$$

This process occurs with very low probability and on a timescale in the ranges of 10^{-9} to 10^{-8} s [37].

Because of the very small cross sections of radiative attachment, in absence of a third body that removes some of the internal energy, a TNI (MX^{*-}) is more likely to relax by releasing the attached electron through Auto-Detachment (AD) or by breaking into a thermodynamically stable anion and a neutral counter fragment through dissociation (DEA). These processes are shown in the Equations 3 and 4, respectively.

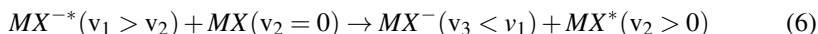


In some cases, if a parent molecule with positive EA has suitable size and symmetry, a TNI can also be stabilized through intramolecular vibrational energy redistribution (IVR). Examples of molecules that form long-lived metastable negative ions through IVR are SF₆ [38], C₆F₆ [39] and C₆₀[40]. In such cases, the electron attachment proceeds through s-wave electron capture [38; 41], where the angular momentum l of the incoming electron is zero. According to the Vogt-Wannier (VW) model [42], the cross section for this process close to electron energy of 0 eV can be written as:

$$\sigma_{E \rightarrow 0} = 4\pi \left(\frac{\alpha}{2E} \right)^{1/2} \quad (5)$$

where E is the energy of the incident electron and α is the polarizability of the molecule. Due to the inverse proportion to the electron energy, the cross section rises sharply at electron energies close to 0 eV.

In the presence of a third-body, for example in clusters, the TNI can transfer some of its internal energy through collisional stabilization, the so-called Bloch-Bradbury mechanism, forming a stable molecular anion, as shown in equation 6.



In dense gasses or plasma, ternary collisions between electrons and molecules are the most efficient in producing negative ions at low electron energies. These processes are shown in Equations 7 and 8.



If the molecule has negative EA, the electron attachment occurs above the parent ground state, and the TNI can only relax through AD or DEA.

The electron trapping mechanisms are in general classified into two categories (see section 2.2): shape resonance, if the electron is constrained by a centrifugal potential barrier, and Feshbach resonance if the electron is trapped in an induced electronic or vibrational excited state. To reduce the complexity of the LEEs interactions with molecules, the electron attachment is often described using quasi-diatomic molecules, the so called quasi-diatomic model. Within this simplification, the electron capture process is generally represented as a vertical transition from the respective neutral ground state of the molecule to an accessible anionic state within the Franck-Condon region of overlap.

This process occurs with transition probability proportional to the Franck-Condon factor (FCF), i.e. the square of the vibrational overlap integral:

$$P_{trans} \propto |\langle \Psi_n | \Psi_a \rangle|^2 \quad (9)$$

2.1.1 Autodetachment

The AD process is described by terms in the Schrodinger equation that couple the bound-state of the TNI to the continuum ($\text{MX} + e^-$ [43]). The transition rate to the continuum can be calculated using the Fermi's golden rule [43; 44]:

$$r_{\text{autodetachment}} = \frac{2\pi}{\hbar} |\langle \phi_f | Q | \phi_i \rangle|^2 \rho \quad (10)$$

Where ϕ_f and ϕ_i are the wavefunctions for the final state ($\text{MX} + e^-$) and the initial state (TNI), respectively, Q is the coupling operator and ρ is the density of states in the continuum. The form assumed by Q , depends on the mechanism that couples the bound state to the continuum.

The breakdown of the Born-Oppenheimer approximation allows the rotational and vibrational AD [43; 44]. Both mechanisms are described by the nuclear kinetic energy operator, which is given by the sum of a radial term, responsible for the vibronic coupling, and an angular term responsible for the rotational-electronic coupling [43; 44]. It can be shown that the autodetachment rate for processes that are mostly driven by the vibronic coupling term, is proportional to the square of the inverse of the nuclear energy [44]. If the electronic ground state of the neutral molecule lies below the anionic state, the driving force for AD can be given by the electron-electron repulsion (configuration-interaction). Another possible mechanism is the spin-orbit autodetachment [43; 44]. After the detachment, if the molecule retains some quanta of the electron's initial energy, in the form of vibrational or rotational energy, the electron is inelastically scattered. This is representatively shown in Figure 2.1, with vertical arrows going from the repulsive potential (MX^{-*}) to several vibrational states of the neutral molecule.

The width of the resonance (Γ) is finite, so the autodetachment lifetime (τ_{AD}) is given by Heisenberg's uncertainty principle [37]:

$$\tau_{AD} = \frac{\hbar}{\Gamma(r)} \quad (11)$$

This relationship between τ_{AD} and (Γ) implies that resonances with long lifetimes (e.g., Feshbach resonances) will appear in a very narrow incident electron energy range, while resonances with a short lifetime (e.g., shape resonances) will appear in a broad energy range.

If the lifetime of the TNI is on the order of the vibrational period, then the TNI is stable against autodetachment and can relax into a metastable NI through IVR. In the case of small molecules like N_2^- , the lifetime of TNIs is in the order of 10^{-14} s [45]. However, in the case of large symmetric molecules like SF_6 the lifetime can be on the order of micro or milliseconds [46].

2.1.2 Dissociative Electron Attachment

When the TNI is formed, the extra electron can be located in a previously unoccupied molecular orbital (LUMO) with M–X anti-bonding character. Due to the repulsive nature of the LUMO orbital, during the lifetime of the TNI, the $[M-X]^-$ bond length will begin to stretch. As can be seen in Figure 2.1, during the relaxation of the TNI along the repulsive curve, if the separation between the nuclei (r) exceeds the crossing of anionic and neutral curves (r_c), AD will no longer be available, and the TNI will dissociate into a neutral atom (M) and a negative ion (X^-) fragments through the DEA process. The excess energy after dissociation could be redistributed into the kinetic energy of the fragments. In the case of a quasi-diatomic molecule, the kinetic energy of the charge retaining fragment (X^-) after DEA is given by [2]:

$$K_X = \left(1 - \frac{m_X}{m_{MX}}\right)[E + EA(X) - BDE(MX) - E_{exc}] \quad (12)$$

where m_X and m_{MX} are the masses of the anion and the parent molecule, E is the energy of the captured electron, $EA(X)$ is the electron affinity of X, $BDE(MX)$ is the bond dissociation energy of MX and E_{exc} is the excitation energy of the fragments. When available, the DEA channel strongly competes with AD and, in general, occurs in the timescale of 10^{-14} to 10^{-12} s [47]. The DEA cross section is given by the product between the electron attachment cross section (σ^{EA}) and the probability of the TNI surviving past the crossing point r_c , which is given by the autodetachment lifetime (τ_{AD}) and the time (t) necessary for the internuclear separation to exceed r_c [48]:

$$\sigma^{DEA} = \sigma^{EA} e^{-t/\tau_{AD}} \quad (13)$$

Towards higher energies the cross section for DEA will drop quickly as the attachment cross section decreases and the probability of AD increases. As a result, the DEA ion yield curves exhibit a non-Gaussian profile and their maximum is shifted toward lower energies as compared to the underlying resonance. This is shown in Figure 2.1, where the attachment and DEA cross sections are compared on the right-hand axis.

Vibrational Feshbach resonances, characterized by a very high cross section, are observed at very low incident electron energies (see section 2.2). However, in order to have fragmentation by DEA, the respective channels must be energetically accessible. The thermochemical threshold for DEA is given by the reaction enthalpy (ΔH_r), which for a single bond rupture can be estimated by subtracting the EA of the charge retaining fragment (X) from the bond dissociation energy ($BDE(M-X)$):

$$\Delta H_r = BDE(M-X) - EA(X) \quad (14)$$

In order to have fragmentation at 0 eV incident electron energy, the electron affinity of the charge retaining fragment must thus exceed the energy required to break the M–X bond; i.e., the asymptotic limit $M + X^-$ must lie below the vibrational ground state of the neutral molecule (see Figure 2.1). If this condition is met, DEA is exothermic and generally occurs through s-wave attachment ($l = 0$) with very high cross (see section 2.2). Examples of molecules with exothermic DEA channels are CCl_4 [49; 50], $CHCl_3$ [49; 50] and HI [51].

If the asymptotic limit $M + X^-$ lies above the vibrational ground state of the neutral

molecule, the dissociative channel is not accessible at electron energies close to 0 eV. In these conditions, single diatomic molecules will autodetach the electron, unless a collision with a third body stabilizes the TNI by removing the excess energy. For example, O_2 has a positive electron affinity of 0.44 eV [52], however, the asymptotic limit $O + O^-$ lies above the vibrational ground state of the neutral molecule and therefore DEA is not energetically accessible at electron energies close to 0 eV. In this molecule, the DEA channel $O + O^-$ occurs through a higher lying shape resonance with an onset at about 4.4 eV and peak intensity at 6.7 eV [53]. It's worth mentioning that if a DEA channel proceeds through a reaction barrier that lies above the respective thermochemical threshold, the resulting ion yield curve will be shifted towards higher energies.

Some DEA reactions in polyatomic molecules don't proceed directly via single bond dissociation along the repulsive potential. They can involve multiple bonds rupture and bond formation(s). In case of such DEA reactions, it's necessary to sum over all the broken and new formed bonds:

$$\Delta H_r = \sum^N BDE(broken) - \sum^M BDE(formed) - EA(X) \quad (15)$$

The formation of new bonds feeds additional energy to the system and the thermochemical threshold will be shifted to lower values. This can be exploited to promote DEA reaction channels at low electron energies, otherwise inaccessible. An example is given by the exothermic HF formation [25; 26; 54; 55]

2.2 Classifications of Negative Ion resonances

Negative Ion resonances (NIR) are classified according to the trapping mechanism by which the incident electron attaches to the molecule.

In a simplified model, the electron attachment process can be seen as a temporary occupation of one of the previously unoccupied molecular orbitals (MO) and according to Koopmans' theorem [56], the electron attachment energy is given by the energy of the occupied virtual MO. In this case, the resulting resonance is named single-particle resonance [57].

At electron energies equal to or above the lowest electronic excitation, the electron capture can induce an electronic excitation and create a hole in one of the previously occupied MOs. Since two electrons are involved in this electron capture process, the resultant resonance is called two-particle resonance. It is also called core-excited resonance [57]. The deeper physical understanding of the trapping mechanisms behind electron attachment is more complicated [2; 58]. Further details are discussed below.

2.2.1 Shape Resonances

In shape resonances, the incident electron is trapped by a potential barrier. When the electron approaches a non-polar neutral molecule that is polarizable, i.e., it has non-zero polarizability (α), a temporary dipole will be induced in the molecule. The charged-induced dipole weakly attracts the electron through a polarization potential,

$V_{\alpha(r)} = -\alpha/2r^4$. However, a particle in motion in a central potential experiences also a repulsive centrifugal potential given by the angular momentum of the particle. Considering a free electron as a wave-packet with contributions of individual partial waves with angular momentum, l , this centrifugal potential is given by:

$$V_{l(r)} = \frac{l(l+1)}{2r^2} \quad (16)$$

Thus, the sum of the two potentials gives the effective potential:

$$V_{eff(r)} = V_{\alpha(r)} + V_{l(r)} = -\frac{\alpha}{2r^4} + \frac{l(l+1)}{2r^2} \quad (17)$$

In addition, at very short electron-molecule distances, when the electron gets closer to the valence electrons of the molecule, a strong repulsive potential arises between the molecule's electron cloud and the trapped electron due to the Pauli repulsion. The sum of this repulsion and the effective potential results in a potential well. For $l \neq 0$, $V_{eff(r)}$ estimated from equation 17 results in a potential barrier that can trap the incoming electron. Some of the incident electrons with $l \neq 0$ will be reflected by the centrifugal barrier; however, one electron may tunnel through the barrier and get trapped by its potential. If the electron has angular momentum components that "fit" the symmetry of an energetically accessible unoccupied orbital, then a shape resonance is formed [35; 36; 59]. For example, in the case of the shape resonance ${}^2\Pi_g$ in N_2 , the incident electron tunnels through a d-wave centrifugal barrier [36; 45].

Shape resonances are quasi-bound states formed energetically above their corresponding parent state; thus, the decay through AD is an open channel. In order to detach the trapped electron must tunnel back through the potential barrier. However, shape resonances may also decay via dissociation (DEA). Typical lifetimes of shape resonances are on the order of $10^{-15} - 10^{-10}$ s [2; 60], thus, the width of these resonances is generally broad, see Equation 11. Single particle shape resonances usually occur in the energy range 0 - 4 eV [36; 60]. In the case of s-wave electrons, the centrifugal potential is zero and there is no potential barrier, so the electron attachment does not proceed through the shape resonance. If the incident electron has enough energy to induce an electronic excitation, i.e. two electrons will occupy previously unoccupied MOs, and the extra electron is trapped by the shape of the potential, the resultant resonance is called core excited shape resonances.

2.2.2 Core-excited Feshbach resonances

Core-excited Feshbach resonances occur when the captured electron simultaneously induces an electronic excitation in the parent molecule with positive electron affinity [58; 60]. They commonly occur at energies 0 - 0.5 eV below their parent states [60], so AD is a closed channel and the electron-molecule system can be considered as a bound state. In this case, the reemission of the captured electron is only possible by gaining some energy from the system or by undergoing electronic configuration change in the resonance. Therefore, such resonances have considerable lifetimes and they present narrow features.

2.2.3 Vibrational Feshbach resonances

Vibrational Feshbach resonances (VFRs), also called nuclear-excited Feshbach resonances, are formed when the kinetic energy of the incident electron is transferred into the vibrational modes of the parent neutral molecule [58; 60]. This is possible due to the breakdown of the Born-Oppenheimer approximation. These resonances lie below their parent states and decay through AD is thus a closed channel [60; 61]. Consequently, VFRs are expected to have a considerable lifetime and usually occur at very low energies with narrow features [61]. These resonances predominantly occur through s-wave attachment and are commonly observed in molecules possessing permanent dipole moment, such as HF [62] and HCl [63], or sufficient polarizability, such as CO₂ [64].

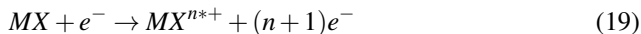
2.3 Positive ions formation through Electron Impact

Positive ionization occurs when the energy of the incident electron is equal to or greater than the ionization potential of the molecule (IE) [65]. If the incoming electron directly ejects a bound electron from the molecule and both electrons leave the molecule, the ionization process is called direct ionization and is shown in Equation 18.

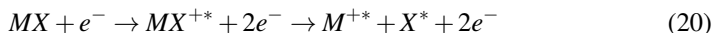


Here, (*) indicates that the fragment may be in a vibrationally and/or electronically excited state.

If the impacting electron has sufficient energy to eject more than one electron, multiple ionization will occur from the molecule:



Since the ionization process occurs on a timescale faster than the nuclear motion, according to the Franck-Condon principle the ejection of an electron can be described as a vertical transition from the ground state of the neutral parent molecule to one of its cationic state. Similar to negative ion formation, the transition probability is proportional to the Franck-Condon factor (FCF). In general, the removal of an electron from a molecule results in weaker and longer bonds as compared to the neutral parent molecule. Therefore, it is very unlikely that after ionization a molecular cation is formed in its vibrational ground state. If the impacting electron transfers sufficient energy, the ionized molecule can dissociate into a positive ion and one or more neutral fragments:

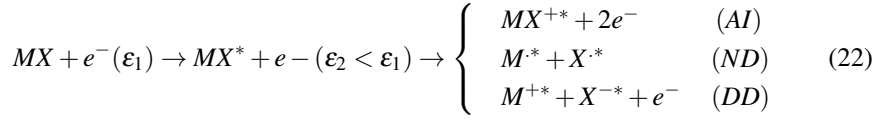


This process is called dissociative ionization (DI). The energetic threshold for the formation of a positive ion, $E_{th}(M^+)$, via DI can be obtained by the following equation:

$$E_{th}(M^+) = BDE(MX) + IE(M) \quad (21)$$

where $BDE(MX)$ is the bond dissociation energy of MX and $IE(M)$ is the ionization energy of M.

Other competing channels are autoionization AI, neutral dissociation (ND) and dipolar dissociation (DD):



AI is a resonant process, while ND and DD are non-resonant processes. Also in these processes, the products may be formed in vibrational or electronic excited states.

2.3.1 Ionization and appearance energy determination

The ionization cross section (σ_{ion}) increases above the ionization threshold and has a maximum at around 70 eV. For the H atom, Wannier [66] found out that, the ionization cross section, at energies close to the threshold, rises according to an exponential law (Wannier law):

$$\sigma_{ion} = E^{1.127} \quad (23)$$

Where E is the energy above the ionization energy. At higher energies above the threshold, the cross section is affected by the formation of excited states. In addition, the competitive reaction channels mentioned above may also affect the behavior of the cross section. The Wannier law can be extended to molecules and DI processes. In that case, the exponent is treated as an additional variable and the value is obtained by fitting the experimental data with the Wannier-like function [67]:

$$f(E) = \begin{cases} b & E < E_1 \\ b + c(E - E_1)^p & E \geq E_1 \end{cases} \quad (24)$$

Where E_1 is the IE of the parent molecule or the appearance energy (AE) of the DI process, b is the constant background, p is the poly-atomic Wannier exponent and c is a coefficient. The parameters E_1 , b, c and p are obtained through a weighted nonlinear least-squares fitting of the experimental data, usually using the Marquart–Levenberg algorithm (MLA)[68]. Typical values of the exponent p are in the range 1.1 – 4.0 [67].

3 Methods

3.1 Experimental setup

All the DEA and DI measurements presented in this work were carried out on a crossed electron-molecule beam apparatus, SIGMA, at the University of Iceland (UI). Figure 3.1 shows a schematic of SIGMA. An exhaustive description of SIGMA and its operative principles is given in Bjarnason et al.[69].

The instrument consists of a trochoidal electron monochromator (TEM), a stainless steel effusive gas inlet system and a HIDEN EPIC 1000 quadrupole mass spectrometer. The TEM is used to generate a quasi mono-energetic electron beam. The electrons are emitted from a tungsten filament, labeled as M1 in Figure 3.1, and guided to the deflection region (M5 and M6) by the electric field generated by the electrostatic lens components M2 – M4. In the deflection region, the electrons experience a crossed electric field between M5 and M6 and a uniform magnetic field of about 50 Gauss, generated by the Helmholtz coils located outside the vacuum chamber. The magnetic field is orthogonal to the crossed electric field. As a result, an electron traveling in this region will drift in the x-direction on a trochoidal trajectory with constant drift velocity v_x given by:

$$\vec{v}_x = \frac{\vec{E} \times \vec{B}}{|\vec{B}|^2} \quad (25)$$

Since \vec{E} and \vec{B} are orthogonal, the equation can be rewritten as:

$$\vec{v}_x = \frac{E}{B} \quad (26)$$

As the drift velocity is constant, the displacement of the electrons depends on their residence time in the deflection region. Slower electrons will be displaced more than faster electrons.

At the end of the deflection region, the electrons exit through the aperture of M7, which is offset by 2.4 mm from the aperture on M4 that defines the entrance to the deflection region.

Consequently, only the electrons with a certain initial velocity along the z-direction and a narrow energy spread will exit through M7. After the deflection region, the selected electrons are guided towards the collision region, where they cross the effusive molecular beam of the target gas. The ions generated from the electron-molecule interactions are then extracted by applying a weak electric field ($\approx 1\text{V/cm}$) between the plate-electrodes C2 and C3 and subsequently focused into the quadrupole mass spectrometer with an Einzel lens configuration of three electrodes (F1-F3).

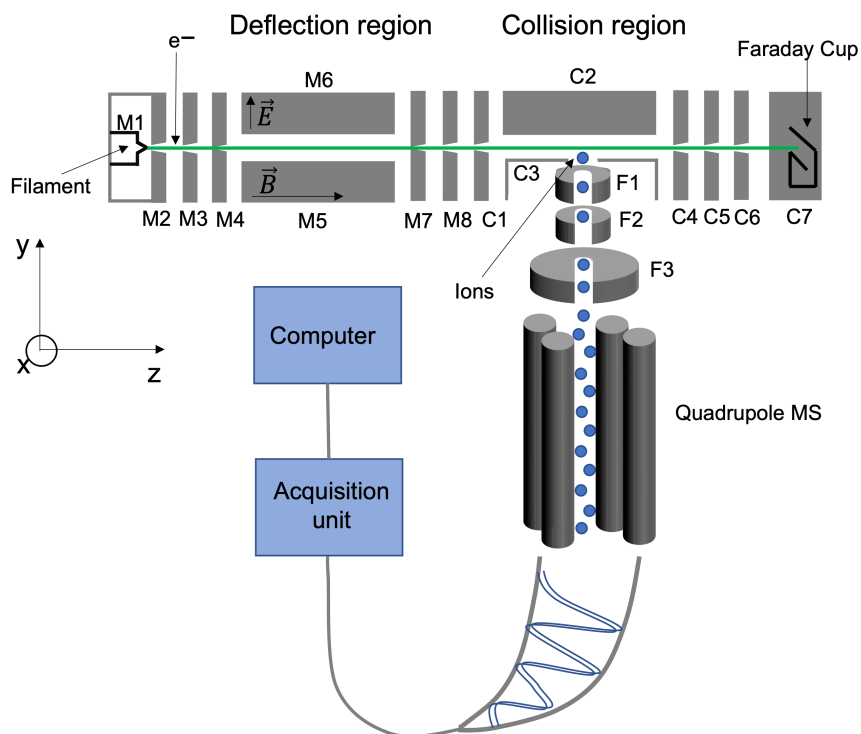


Figure 3.1. Simplified schematic of SIGMA, the crossed electron-molecule beam apparatus used for the DI and DEA measurements in this work. The electron beam is represented with a green line. The magnetic and electric field point along the z-axis and y-axis, respectively. As a result, in the deflection region, the electrons drift in the x-direction.

To avoid back-scattering of the electrons into the collision region, the excess electrons are guided towards a Faraday cup using the C4 and C5 electrodes. The current in the Faraday cup is monitored with a model 6485 Pico-Ammeter (Keithley Instrument, Cleveland, OH, US). The monochromator is heated to 120 °C by two fluorescent lamps to minimize the condensation of target gas on the electrostatic lenses components.

The background pressure of the instrument is approximately 1×10^{-8} mbar, and the sample gas pressures in the conducted experiments were in the range $0.2-4 \times 10^{-6}$ mbar.

With this instrument, it is possible to conduct both DEA and DI measurements. DEA or DI ion yield curves are recorded by ramping the electron energy at a fixed mass (m/z). Mass spectra are obtained through a mass (m/z) scan at fixed energies. The electron energy scale is calibrated using the 0 eV resonance of SF_6^- formation from SF_6 [70; 71] as a reference. It has been reported that the full width at half maximum (FWHM) of this resonance is less than 1 meV [71], therefore the energy resolution of the electron beam can be estimated from the FWHM of the SF_6^- resonance at 0 eV. For the DI measurements, the energy scale is re-calibrated using the appearance energy (AE) of Ar^+ from Ar (i.e., the first ionization of Ar) [72].

3.1.1 Normalization and appearance energies determination

To allow better comparison between measurements recorded on different days at different pressures, the intensities of the ion yields ($I_{m/z}$) are normalized to the respective target gas pressures $p_{m/z}$ and, in the case of DEA measurements, to the intensity of SF_6^- formation ($I_{\text{SF}_6^-}$) at 0 eV electron energy, divided by the SF_6 pressure (p_{SF_6}). In the case of DI measurements the reference used is the intensity of Ar^+ formation (I_{Ar^+}) at 70 eV incident electron energy divided by the pressure of Ar (p_{Ar}). This normalization is shown in Equation 27.

$$I_{\text{Norm.}} = \left(\frac{I_{m/z}}{I_{\text{SF}_6^-}(\text{Ar}^+)} \right) \left(\frac{p_{\text{SF}_6}(\text{Ar})}{p_{m/z}} \right) \quad (27)$$

In this work, the AEs of positive ion formation in the DI process was obtained by fitting the onset of the DI ion yield curves with the Wannier-like function shown in (Equation 24) in the previous Chapter. An example of this procedure is shown in Figure 3.2.

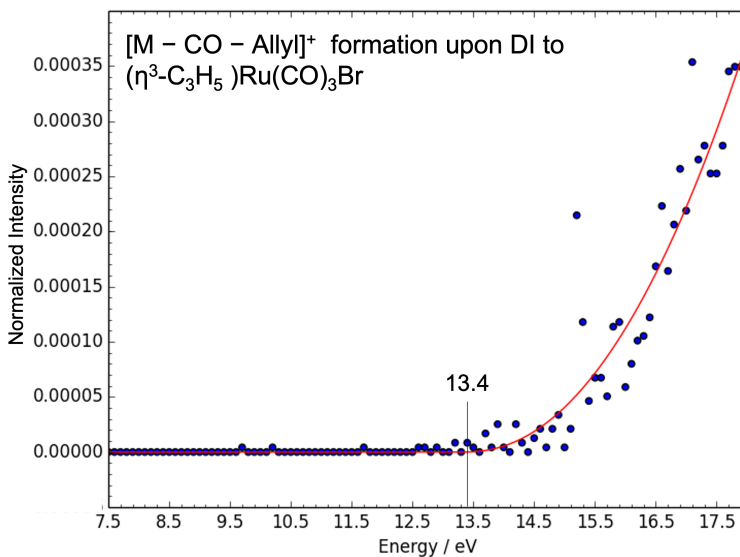


Figure 3.2. Example of appearance energy determination (AE) through a fit with the Wannier-like function (Equation 24) to the onset of the DI ion yield curve for $[\text{RuCO}_2\text{Br}]^+$ formation from the parent molecule $(\eta^3\text{-C}_3\text{H}_5)\text{Ru}(\text{CO})_3\text{Br}$. The intensity was normalized according to equation 27. In the figure, M is the parent molecule. The fitting is shown with the red line.

3.2 Computational Methods

In this thesis, quantum chemical calculations are performed using the computational chemistry software ORCA [73], on $(\eta^3\text{-C}_3\text{H}_5)\text{Ru}(\text{CO})_3\text{Br}$, $\text{Pt}(\text{CO})_2\text{Br}_2$, pentafluorothiophenol (PFTP), 2-fluorothiophenol (2-FTP) and pentafluorobenzoic acid (PBA). The quantum chemical calculations were used to calculate the thermochemical thresholds for DI of $(\eta^3\text{-C}_3\text{H}_5)\text{Ru}(\text{CO})_3\text{Br}$ and DEA to $\text{Pt}(\text{CO})_2\text{Br}_2$, PFTP, 2-FTP and PFBA.

Geometry optimization of all molecules and ions were performed and the relative harmonic vibrational frequencies were calculated at the density functional theory (DFT) level using different functionals and basis sets. In particular, the hybrid functionals, PBE0 [74; 75] for $(\eta^3\text{-C}_3\text{H}_5)\text{Ru}(\text{CO})_3\text{Br}$ and B3LYP [76–78] for PFTP, 2-FTP and PFBA were used, and the range separated hybrid functional $\omega\text{97X-D3}$ [79; 80] for $\text{Pt}(\text{CO})_2\text{Br}_2$ was used. For positive ions, def2-TZVP basis set [81] was used, while for negative ions ma-def2-TZVP [81; 82] and aug-cc-pVTZ [83; 84] were used. From the harmonic vibrational frequency calculations, it was assured that the geometry optimization had effectively reached a minimum and the zero-point vibrational energy (ZPVE) and thermal energy corrections were extracted.

For $(\eta^3\text{-C}_3\text{H}_5)\text{Ru}(\text{CO})_3\text{Br}$ and $\text{Pt}(\text{CO})_2\text{Br}_2$, single-point energy (SPE) calculations were performed on the optimized structures using domain-based local pair natural orbital

coupled cluster theory with perturbative triple excitations (DLPNO-CCSD(T)) [85–88] with different basis sets. In these calculations, for $(\eta^3\text{-C}_3\text{H}_5)\text{Ru}(\text{CO})_3\text{Br}$, DZ/TZ extrapolation (def2-SVP [81] and def2-TZVP) with auxiliary def2-QZVPP/C basis set [89] was used. For $\text{Pt}(\text{CO})_2\text{Br}_2$, aug-cc-pVQZ [83; 84; 90] and aug-cc-pVQZ-PP basis sets and associated pseudopotential for Pt [91] were used. For PFTP, 2-FTP and PFBA, SPE calculations were performed at the same level of theory as used for the geometry optimizations.

In order to understand the nature of anionic resonances in DEA to $\text{Pt}(\text{CO})_2\text{Br}_2$, PFTP, 2-FTP and PFBA, the anionic excited states were calculated through different methods. For $\text{Pt}(\text{CO})_2\text{Br}_2$ and PFBA, a ΔSCF approach was used, for $\text{Pt}(\text{CO})_2\text{X}_2$ ($\text{X} = \text{F}, \text{Cl}, \text{Br}, \text{I}$), time-dependent density functional theory (TDDFT), for PFTP and 2-FTP, the electron attachment equation of motion coupled cluster (EOM-EA-CCSD) method and, finally, for PFBA a ΔSCF approach.

To explore the dynamics involved in neutral HF formation upon DEA to PFTP and 2-FTP, the relative minimum energy path was calculated using the nudged elastic band method with transition state (TS) optimization (NEB-TS) implemented in ORCA [92] at B3LYP/aug-cc-pVTZ level of theory.

A brief overview of the fundamental principles behind the main calculation methods is given below.

3.2.1 Hatree Fock (HF) method

A fundamental postulate of quantum mechanics states that there exists a function, called wavefunction, that contains all the information of a system composed of small particles, such as atoms and molecules (also larger objects can in principle exhibit quantum behavior). In order to extract that information, we need to solve the Schrödinger equation. The time-independent form of the Schrödinger equation is:

$$H\Psi = E\Psi \quad (28)$$

where Ψ is the wavefunction, H is the Hamiltonian operator and E is the energy eigenvalue. For a molecular system the Hamiltonian operator contains the nuclear kinetic energy (T_n), the kinetic energy of all the electrons (T_e), the nuclear-electron coulomb attraction (V_{ne}), the electron-electron repulsion (V_{ee}) and the nuclear-nuclear repulsion (V_{nn}):

$$H_{molecule} = T_n + T_e + V_{ne} + V_{ee} + V_{nn} \quad (29)$$

Due to the interelectron terms and the interdependency of electrons and nuclei in the Hamiltonian, the Schrödinger equation is analytically unsolvable. In order to make a solvable equation, several approximations are used.

Using the Born-Oppenheimer approximation, it is possible to separate electronic and nuclear motion. This is possible because the mass of the nuclei is significantly higher than the mass of the electrons, which implies that the electrons follow the nuclear motion adiabatically.

The Hamiltonian operator can be seen as the sum of the kinetic energy of the nuclei and the electronic Hamiltonian operator H_e :

$$H_{molecule} = T_n + H_e \quad (30)$$

$$H_e = T_e + V_{ne} + V_{EE} + V_{nn} = T_e + V(R, r) \quad (31)$$

Here, R represents the nuclear coordinates and r the electronic coordinates.

Under the Born Oppenheimer approximation, we can neglect the term of the kinetic energy of the nuclei in the molecular Hamiltonian and solve the problem by focusing first on the electronic Hamiltonian for a fixed nuclear configuration:

$$H_e \phi_{(i)}(R, r) = E_i(R) \phi_{(i)}(R, r) \quad (32)$$

The potential that appears in H_e and the electronic eigenfunctions ($\phi_{(i)}(R, r)$) depend parametrically on the nuclear coordinates. We can repeatedly vary the nuclear geometries and solve the electronic Schrödinger equation for each set of nuclear coordinates. The solutions constitute the potential energy surface (PES) of the molecule.

It can be proved that H_e is Hermitian and self-adjoint; therefore, its associated eigenfunctions are orthonormal and form a complete set. They represent the molecular electronic states

The total wavefunction can be expanded as a linear combination of eigenfunctions of the electronic Hamiltonian:

$$\Psi(R, r) = \sum_{i=1}^{\infty} \phi_{ni}(R) \phi(R, r) \quad (33)$$

Here, $\phi_{ni}(R)$ is the nuclear wavefunction. The Born-Oppenheimer approximation simplifies the electron-nuclei and nuclei-nuclei interaction contributions but, unfortunately, it doesn't solve the mutual dependency of the electrons in the V_{ee} term. Therefore, to deal with the electron-electron repulsion we must use another approximation, the independent electron approximation; i.e., the electrons do not interact with each other. Under this assumption, the electronic wavefunction can be expressed as a product of independent single-electron wavefunctions:

$$\phi_i(R, r) = \prod_{i=1}^n \phi_i(R, r_i) \quad (34)$$

This is the so-called Hartree product. However, the Hartree approximation does not include the antisymmetric nature of electrons. An antisymmetric multi-electron wavefunction can be obtained from a single Slater determinant.

The energy of the system, $\langle \Psi | H | \Psi \rangle$, can be obtained by applying the variation principle to the antisymmetric wavefunction. This is the Hartree-Fock (HF) method. The implementation of HF algorithms requires an initial guess for the multi-electron wavefunction. The solution of the HF equations gives a new wavefunction that is used as a new initial guess. This is done iteratively until the convergence is reached, i.e. the wavefunction doesn't change and the energy is minimized according to the variational principle. The single-electron wavefunctions are approximated with a linear combination of basis functions (basis set). Common basis functions are Slater-type orbitals (STO) and Gaussian-type orbitals (GTO).

While the HF method accounts for the exchange energy, the correlation in the motion of electrons with opposite spins is missing. Post-HF wavefunction-based methods, such as coupled cluster, have been developed to correct the missing correlation energy. However

high-level wavefunction-based methods, in general, are computationally expensive. An alternative approach is the density functional theory (DFT), which describes the potential as a functional of the electron density. In principle, this approach is computationally cheaper because it reduces the $3N$ dimensional problem to the 3-dimensional problem of the electron density.

3.2.2 Density Functional Theory

The heart of the DFT method resides in the Hohenberg–Kohn (HK) theorems [93; 94]. According to the theorems there exists a functional of the electron density which fully determines the ground state of an interacting many-particle system in a static potential and for each electron density is always possible to apply the variational principle. Therefore, if the functional form of the electron density is known, the minimization of the functional leads to the full solution of the Schrodinger equation.

However, the exact form of the functional for the electron density is unknown and needs to be approximated. Kohn-Sham derived a first approximation for an electron gas [94]:

$$G(\rho_0) = T_e(\rho_0) + E_{xc}(\rho_0) \quad (35)$$

The energy functional for the kinetic energy term is obtained with molecular orbitals that are described with basis functions. The exchange-correlation is approximated with different methods. The most common functional approximations are the local density approximation (LDA) and the general gradient approximation (GGA). LDA functionals assume that the electron density is homogeneous and evaluate the density only in one point. GGA functionals take into account the inhomogeneity of the electron density introducing a density gradient. These functionals have good accuracy and are computationally cheap. However, their implementation of the exchange-correlation fails in describing some systems such as transition metals [95–97], anions [98], and dissociation limits [99]. This is due to the self-interaction error. In the HF method the unphysical self-interaction of one electron in the Hartree term (the potential generated by the distribution of the electrons) is eliminated by the exact exchange term. In hybrid functionals the exchange-correlation energy is constructed as a linear combination of the exact HF exchange and the DFT exchange-correlation term. The mixing parameters are obtained by fitting experimental data sets. However, hybrid functionals do not eliminate completely the self-interaction error.

A subgroup of hybrid functionals is constituted by the range separated functionals. In these functionals, the coulomb operator in the HF-DFT exchange-correlation is split into two parts which account for the short-range (SR) interaction and long-range (LR) interaction. The exchange energy in SR is handled by the local DFT exchange while the LR part includes the HF exchange.

3.2.3 Time dependent density functional theory

The HK theorems refer to stationary states. For non-stationary states, time-dependent density functional theory (TDDFT) has been developed. The heart of TDDFT resides in the Runge-Gross theorem (RG) [100], which is the time-dependent version of the HK theorem. The RG theorem states that there is a map between the time-dependent external

potential of a system and its time-dependent density. In other words, the time-dependent external potential is uniquely determined by the time-dependent density.

TDDFT is an important tool to obtain stationary excited states. In general, improved wavefunction-based methods, such as equation-of-motion coupled-cluster theory (EOM-CCSD), are more accurate than TDDFT. However, they are computationally expensive. TDDFT is formally exact, however, since it relies on the exchange-correlation functionals, approximations are unavoidable. It's worth mentioning that while excited states are physically observable, it is not possible to directly observe the transition between stationary states due to the collapse of the wavefunction. The implementation of TDDFT consists in solving iteratively the Casida eigenvalue equations [101; 102] til the lowest excitation energies is found. The Casida equations can be simplified by neglecting of the so-called "B" matrix, according to the Tamm-Dancoff (TDA) approximation [103].

3.2.4 Equation-of-motion coupled cluster theory

In EOM-CC formalism [104] the excited wavefunction can be written as:

$$|\Psi_{exc}\rangle = Re^T |\phi_0\rangle \quad (36)$$

Where R and T are excitation operators and $|\phi_0\rangle$ is a single Slater determinant for the ground state.

Consequently, the Schroedinger equation for excited states can be formulated as:

$$He^T R |\phi_0\rangle = ER e^T |\phi_0\rangle \quad (37)$$

Since the excitation operators commute and R is a linear parametrized operator, we can reformulate 3.12 as an eigenvalue problem:

$$[e^{-T} H e^T - E] R |\phi_0\rangle = 0 \quad (38)$$

The problem of finding the energies and properties of excited states is thus reduced to diagonalization of the effective Hamiltonian $\bar{H} = e^{-T} H e^T$. While EOM-CC is formally exact, the R and T operators need to be truncated. The parameters for the T operator are obtained from the ground state coupled-cluster calculations ($R=1$), while the parameters for the R operator are obtained by diagonalization of the effective Hamiltonian.

3.2.5 Thermochemical Threshold Calculations

The reaction enthalpy at 0 K for a DI or DEA process is given by:

$$\Delta H_{0K} = \sum_{i=1}^N (E_i^{SPE} + ZPVE_i) - (E_{parent}^{SPE} + ZPVE_{parent}) \quad (39)$$

In the expression above, E_i^{SPE} and $ZPVE_i$ are the single point energies and zero-point vibrational energies, respectively, of the resulting fragments from the DI or DEA process; E_{parent}^{SPE} and $ZPVE_{parent}$ are the single point energy and zero-point vibrational energy of the parent molecule, respectively; N is the number of fragments produced.

However, also the thermal energy of the neutral ($E_{therm,neu}$) parent molecule can be

used up in DEA and DI processes. Therefore, the corrected thermochemical threshold is given by:

$$E_{th} = \Delta H_{0K} + E_{therm,neut} \quad (40)$$

As previously discussed, single point energy calculations were conducted on the optimized molecular structures. ZPVEs and thermal energy corrections were obtained from harmonic vibrational frequency calculations.

3.2.6 Reaction path calculations

In this thesis, in order to further explore the dynamics of HF formation from PFTP and 2-FTP through DEA, the respective reaction paths were computed using the nudged elastic band method with transition state (TS) optimization (NEB-TS). The NEB method is a chain-of-states method that is used for finding the minimum energy path and saddle point between two optimized geometries, i.e., the local minima reactant and product. The calculation starts by discretizing the reaction path with a chain of images that are arrays containing the Cartesian coordinates of the system. Usually this is done through a linear interpolation of the Cartesian coordinates between the initial and final images. At least 3 images are necessary. The minimum energy path is then found with an optimization algorithm by iteratively moving the images along the opposite direction of the gradient of the energy. The shape of the path is modified according to the normal component of the atomic forces. Harmonic springs between adjacent images are employed in order to control the distribution of the images along the path and prevent them from sliding down to the initial or final local minima. More specifically, this is done by replacing the tangential components of the atomic forces with the tangential component of the spring force. In the climbing image-nudged elastic band (CI-NEB), in order to drive the reaction path to the saddle point, for the highest energy image the spring forces are removed and the tangential components of the atomic forces are inverted. As a result, the image will be forced to climb up along the path and it will converge to an saddle point. In NEB-TS method, implemented in ORCA package version 4.2.1, NEB-CI is used to find an approximated saddle point which is then rigorously optimized through eigenvector-following calculation

4 Results and Discussion

4.1 Low-energy interaction with focused electron beam induced deposition precursors

4.1.1 Motivation and Previous Work

Focused electron beam induced deposition (FEBID) is a nanofabrication technique that allows direct-writing of patterns on a substrate by the desired material with a focused, high-energy electron beam [3; 4; 105]. Deposition occurs due to electron-induced fragmentation of previously adsorbed precursors, usually organometallic complexes. In an ideal case, the dissociation of FEBID precursors creates pure deposits under the area exposed to the electron beam. However, at the current stage, the depositions exceed the spatial resolution of the electron beam and the metal purity is generally poor. This is mainly attributed to the interactions of the precursors with scattered electrons and low-energy SEs generated by the interaction of the primary electron beam with the surface [7]. The energy distribution of these SEs peaks below 10 eV, has a substantial contribution close to 0 eV and a high energy tail [106; 107]. Low-energy electrons (LEEs) can induce fragmentation through four distinct processes, DI, DEA, ND and DD, and it has been found that these low-energy electron interactions play an important role in the deposition processes. [7; 108; 109].

Surface science studies do not allow to investigate the energy dependency of the these LEEs interactions. Therefore, in an effort to develop FEBID precursors with high performance, gas-phase studies are conducted with the aim of characterizing the low-energy electron interactions with FEBID precursors. The comparison of gas-phase studies on FEBID precursors with their electron- induced decomposition on surfaces allows to identify the initial electron-induced mechanism of precursor decomposition in FEBID.

In the context of investigating the energy dependence and the extent of LEE interactions with FEBID precursors, gas-phase studies on DI to $(\eta^3\text{-C}_3\text{H}_5)\text{Ru}(\text{CO})_3\text{Br}$ and DEA/DI to $\text{Pt}(\text{CO})_2\text{Br}_2$ were conducted.

In EUVL masks repair, ruthenium-based organometallic complexes can be used as precursors for the deposition of Ru capping layer through FEBID [110]. In fact, due to its high transparency in the EUV, Ru does not negatively affect the EUV reflectivity [111]. However, to our knowledge, there is only one commonly used Ru precursor, (ethylcyclopentadienyl)ruthenium(II), and it produces deposits with high carbon content during its electron-induced decomposition [110]. A further electron-irradiation of the deposit in the presence of O_2 is necessary for the removal of carbon. However, O_2 oxidizes the metal.

Therefore, in order to obtain pure Ru deposits, it is necessary to explore the electron-induced chemistry with different ligand architectures. In this context, a number of studies have been conducted on $(\eta^3\text{-C}_3\text{H}_5)_3\text{Ru}(\text{CO})_3\text{Br}$ in the gas-phase [19; 20], on surfaces [21] and in FEBID deposition [112]. The current DI study on $(\eta^3\text{-C}_3\text{H}_5)_3\text{Ru}(\text{CO})_3\text{Br}$, presented in Article I, is a follow up of previous gas-phase studies where DEA to this compound has been studied [19; 20] and compared with a surface science study on this compound [21]. In the current study, the electron impact ionization energy and the appearance energies (AEs) of the DI channels are estimated by fitting the respective ion yield curves with a Wannier type function [67] and comparing them with the theoretical values obtained from quantum chemical calculations at the PBE0 and DLPNO-CCSD(T) level of theory. In addition, a comparison with the results of the previous surface science study [21] and FEBID study [112] is offered.

Platinum-based complexes are used as chemotherapeutic anticancer drugs and in synchronous combination with radiation (chemoradiation) [113–115] as well as precursors for FEBID [116–118]. In both applications, fragmentation induced by LEEs plays an important role. The role of LEEs in FEBID has been discussed here above and the relevance of the LEEs interactions in chemoradiation therapy will be discussed in section 4.2.

In the context of FEBID, LEE interactions with platinum-based organometallic compounds have been investigated in several studies [24; 119–121]. In the previous gas phase study on LEEs interactions with, $\text{Pt}(\text{CO})_2\text{Cl}_2$ [24], it appeared that single and double CO loss, observed close to 0 eV, are the most efficient DEA channels. It was also found that CO loss is the dominant DI process, even though Cl loss and the bare Pt^+ ion were observed with significant intensity. This compound had been subject of a recent UHV surface study [22], where the authors exposed monolayers of $\text{Pt}(\text{CO})_2\text{Cl}_2$ to 500 eV electrons. They observed a rapid CO loss, during the initial electron irradiation step, and a PtCl_2 deposit. With prolonged electron irradiation, the chlorine was also removed nearly quantitatively. Therefore, according to the results of the previous gas-phase study, it appears that in the UHV surface study the rapid CO loss, during the initial electron irradiation step, is promoted by DEA.

In a very recent comparative deposition study [23] of $\text{Pt}(\text{CO})_2\text{Cl}_2$ and $\text{Pt}(\text{CO})_2\text{Br}_2$, the authors found a significant amount of halogens in the UHV deposits but little or no traces of carbon. However, under HV conditions, they found a high carbon content in the deposits and only small amounts of halogens.

This can be explained following the observations of Rohdenburg et al. [122] in electron-induced reactions of $(\eta^3\text{-C}_3\text{H}_5)_3\text{Ru}(\text{CO})_3\text{Cl}$, in the presence of NH_3 , and in cisplatin [123], where they suggested that proton transfer from NH_3 to Cl^- or Cl, assists the removal of the Cl ligands through the formation of HCl. In the case of the HV study on $\text{Pt}(\text{CO})_2\text{Cl}_2$, it may be possible that traces of water assists the removal of Cl through proton transfer leading to formation of HCl.

Motivated by the previous gas-phase study on $\text{Pt}(\text{CO})_2\text{Cl}_2$, gas-phase DEA and DI studies on $\text{Pt}(\text{CO})_2\text{Br}_2$ were conducted within the framework of this thesis and compared with previous work on electron-induced decomposition of $\text{Pt}(\text{CO})_2\text{Cl}_2$ and $\text{Pt}(\text{CO})_2\text{Cl}_2$. Furthermore, a comparison to DEA to cisplatin [28] is also offered. This comparison, which is relevant for chemoradiotherapy, will be discussed in the next chapter.

4.1.2 Dissociative ionization of $(\eta^3\text{-C}_3\text{H}_5)\text{Ru}(\text{CO})_3\text{Br}$

Figure 4.1.2 shows the optimized ground state geometry of $(\eta^3\text{-C}_3\text{H}_5)\text{Ru}(\text{CO})_3\text{Br}$ at the PBE0 D3BJ/def2-TZVP level of theory.

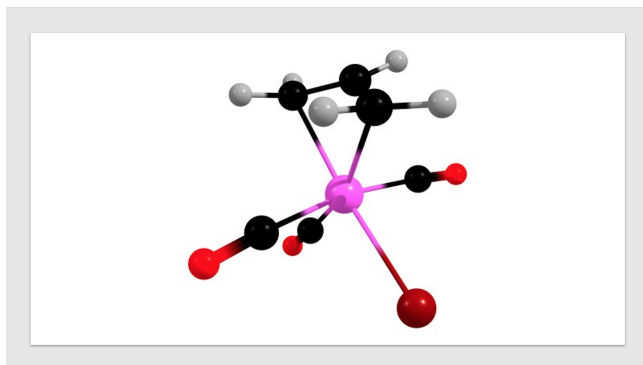


Figure 4.1. Optimized ground state geometry of $(\eta^3\text{-C}_3\text{H}_5)\text{Ru}(\text{CO})_3\text{Br}$ at the PBE0 D3BJ/def2-TZVP level of theory. The colors of the atoms are assigned as follow: Ru: Pink, C: Black, H: gray, O: red, Br: dark red

The positive ion mass spectrum of $(\eta^3\text{-C}_3\text{H}_5)\text{Ru}(\text{CO})_3\text{Br}$ at 75 eV incident electron energy, shown in Figure 4.2, has been reported in the previous gas phase study on this compound [19] and also in Article I.

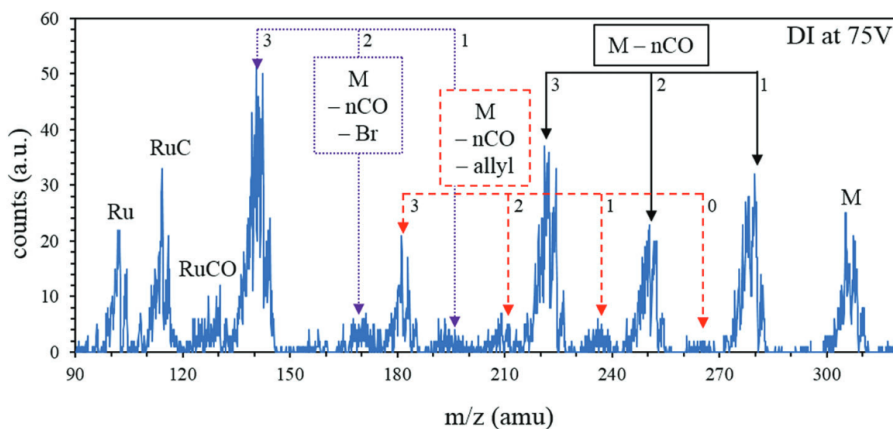


Figure 4.2. Positive mass spectrum of $(\eta^3\text{-C}_3\text{H}_5)\text{Ru}(\text{CO})_3\text{Br}$ recorded at 75 eV incident electron energy. The main DI channels are the progressions: $[M - n\text{CO}]^+$, $[M - n\text{CO} - \text{allyl}]^+$ and $[M - n\text{CO} - \text{Br}]^+$. Furthermore, also the parent cation and Br^+ appear with significant intensity. Reprinted with permission from refs [19]

As can be seen from the mass spectrum, DI to $(\eta^3\text{-C}_3\text{H}_5)\text{Ru}(\text{CO})_3\text{Br}$ leads to sequential losses of 1-3 CO ligands, the allyl group and 0-3 CO ligands, and the bromine and 0-3

CO ligands.

The loss of the CO ligands is the dominant progression. Other fragments, observed with fair intensity, are $[\text{RuCO}]^+$, $[\text{RuC}]^+$ and the bare ion $[\text{Ru}]^+$.

Figure 4.3 shows the positive ion yield curves recorded in the incident electron energy range 0-70 eV for (a) the loss of 1-3 CO units and (b) the loss of the allyl group and 0-3 CO units. The respective experimental AEs and the calculated threshold values at the PBE0 D3BJ/def2-TZVP and DLPNO-CCSD(T)/Extrapolate (2/3,def2) def2-TZVP/C levels of theory are reported in Table 4.1. The AEs were obtained by fitting the onset of the ion yield curves with the Wannier-like function shown in the methods section (Equation 24).

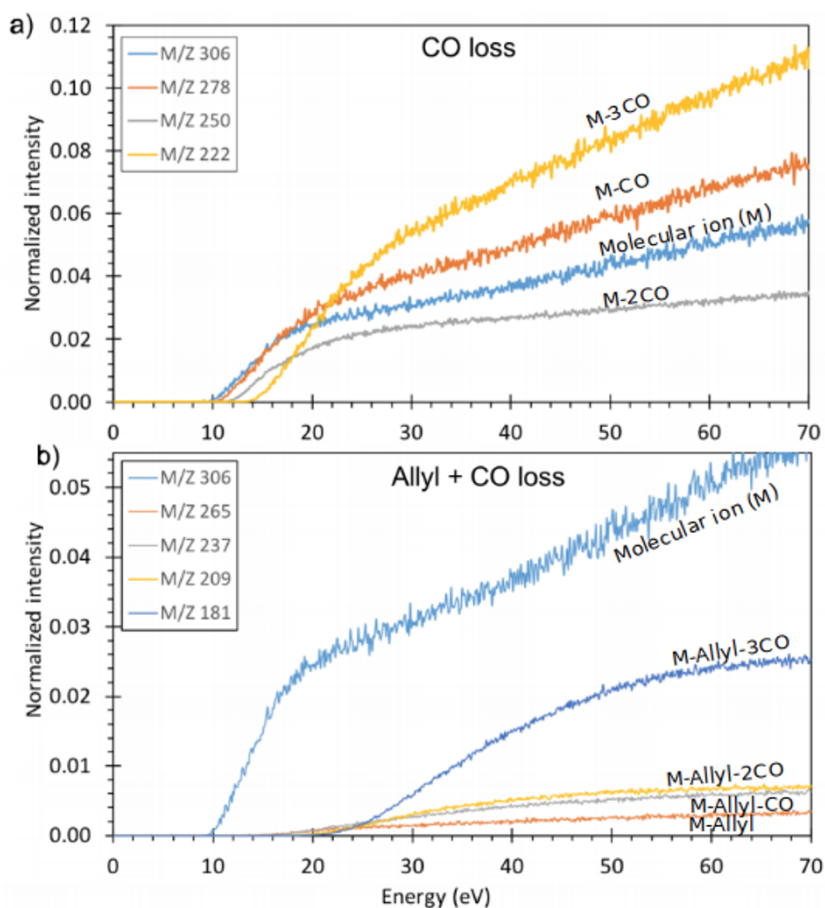


Figure 4.3. Positive ion yield curves for (a) the sequential loss of 1-3 CO ligands and (b) the sequential loss of the allyl group and 1-3 CO ligands from $(\eta^3\text{-C}_3\text{H}_5)_2\text{Ru}(\text{CO})_3\text{Br}$. The ion yield curves are normalized to the target gas pressure and Ar^+ intensity at 70 eV as described in the methods section (Equation 27). Adapted with permission from ref [124]

Table 4.1. Experimental IE and AEs and calculated thresholds at the PBE0 D3BJ/def2-TZVP and DLPNO-CCSD(T)/Extrapolate (2/3,def2) def2-TZVP/C levels of theory for the main fragments observed. Geometry optimizations were performed at the PBE0 D3BJ/def2-TZVP level of theory. The values are from ref [124].

Fragment	m/z	AE	PBE0	DLPNO-CCSD(T)
$[(\eta^3\text{-C}_3\text{H}_5)\text{Ru}(\text{CO})_3\text{Br}]^+$	306	8.6 ± 0.6	7.99	8.20
$[(\eta^3\text{-C}_3\text{H}_5)\text{Ru}(\text{CO})_2\text{Br}]^+$	278	9.9 ± 0.5	9.43	9.57
$[(\eta^3\text{-C}_3\text{H}_5)\text{Ru}(\text{CO})\text{Br}]^+$	250	10.8 ± 0.5	10.76	10.58
$[(\eta^3\text{-C}_3\text{H}_5)\text{RuBr}]^+$	222	13.3 ± 0.5	12.77	12.34
$[\text{Ru}(\text{CO})_3\text{Br}]^+$	265	12.9 ± 0.6	10.13	10.40
$[\text{Ru}(\text{CO})_2\text{Br}]^+$	237	13.4 ± 0.5	12.24	12.29
$[\text{Ru}(\text{CO})\text{Br}]^+$	209	15.7 ± 0.5	15.31	15.59
$[\text{RuBr}]^+$	181	16.6 ± 0.6	17.65	17.02
$[(\eta^3\text{-C}_3\text{H}_5)\text{Ru}]^+$	143	15.9 ± 0.5	15.15	14.33
$[\text{RuC}]^+$	114	17.4 ± 0.5	18.6	17.11
Ru^+	102	18.8 ± 0.5	18.74	17.81

Taking into account the confidence limit of the experimental values, it can be seen that there is a good agreement with the theoretical values in the cases of the ionization energy (m/z 306), loss of 1 and 2 CO units, and loss of the allyl group and 2 CO units. Also for the formation of $[\text{RuCO}]^+$, $[\text{RuC}]^+$ and the bare ion $[\text{Ru}]^+$ there is a fair agreement. However, for $[\text{RuC}]^+$ assuming that the carbon originates from the allyl group and that H_2 is formed, we derived a threshold of 21.96 eV, at the DFT level, and 20.44 eV at the coupled cluster (DLPNO-CCSD(T)) level. These values are far above the experimental AE. Assuming that in this process a dipolar dissociation takes place, leading to Br^- formation, the threshold was found to be 18.6 eV at the DFT level and 17.11 eV at the coupled cluster level. The latter is in good agreement with the experimentally determined AE, as is discussed in Article I.

The calculated thresholds for the loss of the allyl group and the loss of the allyl group and one CO unit, are much lower than the respective experimental values. This can be due to the excess energy required for the dissociation of the allyl group in order for these two DI channels to be observed within our experimental time frame. An effect that is commonly referred to as kinetic shift. As can be seen in the mass spectrum and in the ion yield curves, in the allyl and CO loss sequence, the intensity progressively increases with further CO losses and the loss of the allyl group and 3 CO units has the most intensity. This can be rationalized if the excess energy needed for allyl loss is channeled into further loss of the CO ligands. This is in line with the π -facial interaction of the allyl carbons with the central Ru atom. Hence, confirming that this ligand is a poor leaving group and not suitable as ligand for FEBID precursors for pure metal deposition.

Previous surface studies have shown that CO ligands in FEBID precursors are very labile under electron irradiation [21; 125; 126]. In surface experiments on $(\eta^3\text{-C}_3\text{H}_5)\text{Ru}(\text{CO})_3\text{Br}$, Spencer et al. [21] found that the allyl and bromide ligands are poor leaving group. This correlates with our observations.

In the previous surface study, a nanometer-thick film of $(\eta^3\text{-C}_3\text{H}_5)\text{Ru}(\text{CO})_3\text{Br}$ was

absorbed onto amorphous carbon and polycrystalline gold substrates. In order to achieve molecular adsorption of the precursors, the substrates were cooled to $-168\text{ }^{\circ}\text{C}$. The films were incrementally electron irradiated, using a 500 eV flood gun, under controlled UHV conditions.

X-ray photoelectron spectroscopy (XPS) revealed that 80% of the CO is lost already after an electron irradiation of about $4 \times 10^{16}\text{ e}^{-}\text{ cm}^{-2}$, while the allyl and bromine remained on the surface. However, bromine loss was observed with further electron irradiation of about $5 \times 10^{18}\text{ e}^{-}\text{ cm}^{-2}$, but the carbon from the allyl group remained on the surface.

In the FEBID study [112], the authors observed the loss of all three CO ligands and a partial allyl loss. However, they did not observe bromine loss. This is understandable since bromine loss is observed in the surface experiments after prolonged irradiation, while FEBID experiments are conducted under quasi steady-state conditions.

As mentioned in the previous gas-phase study [19], DI of $(\eta^3\text{-C}_3\text{H}_5)_3\text{Ru}(\text{CO})_3\text{Br}$ leads to a weighted average loss per incident of 2.1 for the CO ligands, 0.3 for the Allyl group and 0.4 for Br. Dissociative electron attachment leads to a weighted average CO loss per incident of 0.9 and other channels are insignificant.

Comparing the gas-phase average losses per incident with the deposits from the surface science study and FEBID experiments does not offer a good correlation. However, as is clear from our study, the allyl group is a poor leaving group in both DEA and DI, which is reflected in the previous surface and deposition studies.

4.1.3 cis-Pt(CO)₂Br₂: dissociative electron attachment and dissociative ionization

Figure 4.4 shows the optimized ground state geometry of Pt(CO)₂Br₂ at the ω B97X-D3/ma-def2-TZVP level of theory.

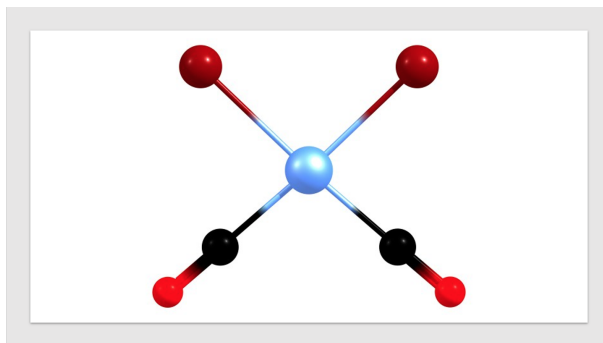


Figure 4.4. Optimized ground state geometry of Pt(CO)₂Br₂ at the ω B97X-D3/ma-def2-TZVP level of theory. The colors of the atoms are assigned as follow: Pt: light blue, C: Black, O: red, Br: dark red

The most efficient DEA processes for Pt(CO)₂Br₂ are the formations of [Pt(CO)Br₂]⁻ and [PtBr₂]⁻, i.e., the loss of one and two CO ligands, respectively. These ion yield curves are shown in Figure 4.5. The ion yield curve of [Pt(CO)Br₂]⁻ has a contribution peaking at 0 eV, while that for [PtBr₂]⁻ shows maximum intensity at about 0.07 eV and a higher-lying contribution close to 3 eV.

This is consistent with the previous observations on DEA to Pt(CO)₂Cl₂ [24], where the ion yield curves for [Pt(CO)Cl₂]⁻ and [PtCl₂]⁻ have their maximum intensity at or close to 0 eV and a higher-lying contribution is also present in the [PtCl₂]⁻ ion yield curve. This was attributed to the fact that the loss of a single CO ligand from Pt(CO)₂Cl₂ is exothermic, so the excess energy after the first CO loss is channeled into a further CO loss, making the survival probability of the [Pt(CO)Cl₂]⁻ fragment low above the threshold.

We found that in DEA to [Pt(CO)₂Br₂]⁻ the single and double losses of the CO ligands are both exothermic. At the DLPNO-CCSD(T)/aug-cc-pVQZ level of theory, the threshold for single CO loss was found to be -1.57 eV and that for the double CO loss was found to be -0.48 eV. Therefore, already at 0 eV sufficient excess energy is available in the [Pt(CO)Br₂]⁻ fragment to be channeled into the further CO loss and the survival probability of [Pt(CO)Br₂]⁻ drops rapidly above threshold.

As is apparent in Figure 4.5, the low-energy contributions in the [Pt(CO)Br₂]⁻ and [PtBr₂]⁻ ion yield curves are asymmetric towards higher energies. We attributed this to a overlapping higher energy contribution. This is shown with a fit of two Gaussians to the ion yield curves in Figure 4.6. In the case of [Pt(CO)Br₂]⁻, the higher energy contribution peaks at 0.18 eV, while for [PtBr₂]⁻ it peaks at 0.33 eV.

The anionic ground state of Pt(CO)₂Cl₂ was found to be formed by electron occupation of the LUMO of the neutral, which is a mixture of contribution from the π^* CO orbitals

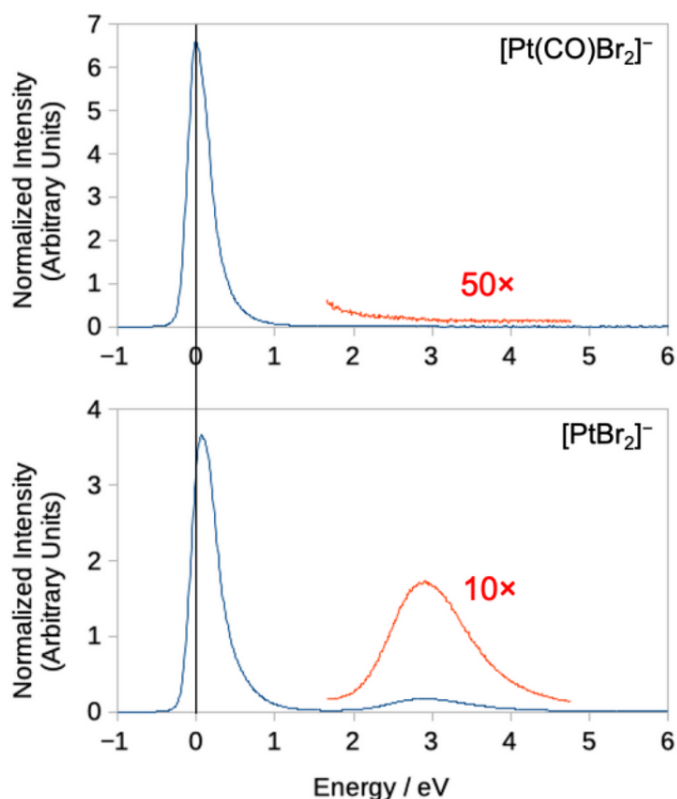


Figure 4.5. Negative ion yields for $[\text{Pt}(\text{CO})\text{Br}_2]^-$, the loss of one CO ligand, and $[\text{PtBr}_2]^-$, the loss of two CO ligands. Both the ion yield curves have a low energy contribution peaking at or close to 0 eV. The ion yield curve for $[\text{PtBr}_2]^-$ presents an additional higher-lying contribution with much less intensity. Reprinted from ref. [127] under open access Creative Commons CC BY 4.0 license.

and the $\text{Pt } 5d_{xy}\pi^*$. The first excited anionic state, on the other hand, is consistent with electron occupation of the LUMO+1, which is composed of the $\text{Pt } d_{x^2-y^2}$ orbital and σ^* P–L antibonding (L = CO or Br). The contour plot of the corresponding SOMO and SOMO+1 are shown in Figure 4.7. The vertical attachment energy (VAE) for the anionic ground state was calculated to be 1.14 eV at the $\omega\text{B97X-D3}$ level of theory. With a ΔSCF approach at the same level of theory, we derived a VAE for the first excited anionic state of -0.99 eV. Accordingly, the low-energy contributions in the $[\text{Pt}(\text{CO})\text{Br}_2]^-$ and $[\text{PtBr}_2]^-$ ion yield curves can be attributed to electron capture in to the LUMO, while the higher-lying overlapping contributions can be attributed to electron occupation of the LUMO+1.

Direct CO loss from the first excited anionic state is in line with the repulsive nature of the σ^* SOMO+1. The same process is, however, symmetry forbidden from the SOMO and requires effective coupling of the CO π^* orbital with the respective σ^* P–L. In the

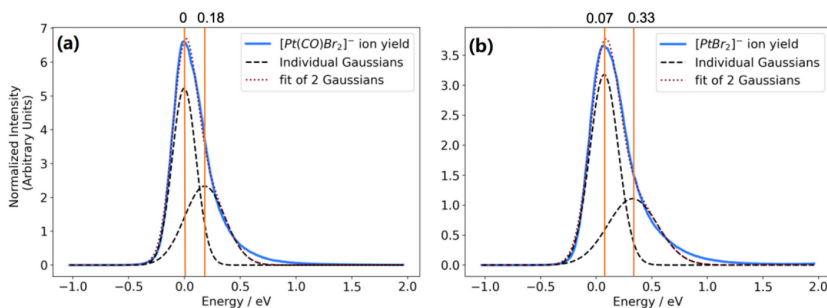


Figure 4.6. Combined fit of two Gaussian functions to the $[Pt(CO)Br_2]^-$ ion yield (on the left) and $[PtBr_2]^-$ ion yield (on the right). The individual Gaussians show the two underlying resonances in the low energy contribution in these ion yield curves. The first individual Gaussian represents contributions from dissociation from the anionic ground state, while the second individual Gaussian represents these from the first excited anionic state. Reprinted from ref. [127] under open access Creative Commons CC BY 4.0 license.

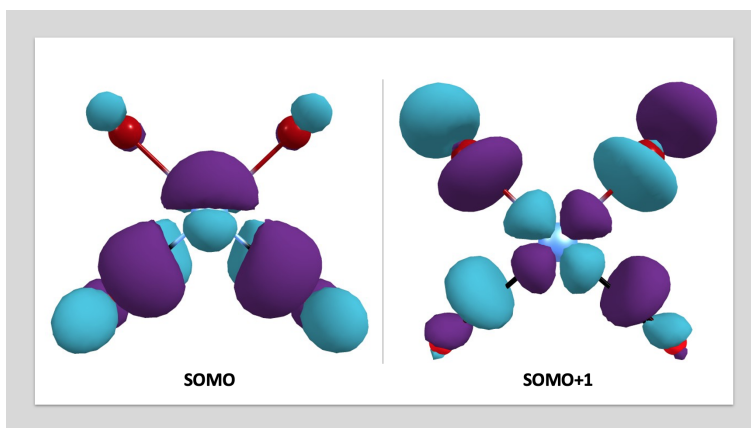


Figure 4.7. Contour plot of the SOMO and SOMO+1 of $[Pt(CO)_2Br_2]$. The SOMO was calculated at the $\omega B97X-D3/ma-def2-TZVP$ level of theory. The SOMO+1 was obtained with a ΔSCF approach at the same level of theory. Redrawn from the original source in ref. [127] under open access Creative Commons CC BY 4.0 license

previous study on $Pt(CO)_2Cl_2$ [24], it was suggested that this coupling can be provided by the out-of-plane bending of the CO ligands.

However, we found the dipole moment of $Pt(CO)_2Br_2$ to be 5.0 D at the $\omega B97X-D3$ level of theory. This value is significantly above the threshold limit for the electron capture into a dipole bound state [128]. Therefore, for the lower-lying resonances, it is possible that an initially formed dipole-bound state provides a doorway for DEA by coupling with the nuclear motion and promoting a vibrational Feasbch resonance. This process was discussed by Sommerfeld [129] for uracil and cyanoacetylene and by

Stepanović et al.[130] for ethylene carbonate and ethylene carbonate-d4.

To explore the influence of halogen substitution to the VAE, we calculated vertical excitation energies $\text{SOMO}+1 \leftarrow \text{SOMO}$ at the TDDFT $\omega\text{B97X-D3/ma-def2-TZVP}$ level of theory for $\text{Pt}(\text{CO})_2\text{X}_2$ ($\text{X} = \text{F}, \text{Cl}, \text{Br}, \text{I}$). They are reported in Table 4.2. As can be seen the values decrease according to the trend: $[\text{Pt}(\text{CO})_2\text{F}_2]^- > [\text{Pt}(\text{CO})_2\text{Cl}_2]^- > [\text{Pt}(\text{CO})_2\text{Br}_2]^- > [\text{Pt}(\text{CO})_2\text{I}_2]^-$. This is in line with the increased destabilization of the σ^* SOMO+1 with increasing electronegativity of the halogen.

Other observed DEA fragments with much lower intensity are $[\text{Pt}(\text{CO})\text{Br}]^-$, $[\text{PtBr}]^-$ and Br^- . All the respective ion yield curves and threshold calculations are reported in Article II.

Table 4.2. Calculated vertical excitation energies $\text{SOMO}+1 \leftarrow \text{SOMO}$ at the TDDFT $\omega\text{B97X-D3/ma-def2-TZVP}$ level of theory for $\text{Pt}(\text{CO})_2\text{X}_2$ ($\text{X} = \text{F}, \text{Cl}, \text{Br}, \text{I}$)

Anions	Vertical Excitation $\text{SOMO}+1 \leftarrow \text{SOMO}$
$[\text{Pt}(\text{CO})_2\text{F}_2]^-$	0.58
$[\text{Pt}(\text{CO})_2\text{Cl}_2]^-$	0.44
$[\text{Pt}(\text{CO})_2\text{Br}_2]^-$	0.27
$[\text{Pt}(\text{CO})_2\text{I}_2]^-$	0.13

Dissociative ionization to $\text{Pt}(\text{CO})_2\text{Br}_2$ leads to significantly more fragmentation than DEA. Figure 4.8 shows the positive ion mass spectrum of $\text{Pt}(\text{CO})_2\text{Br}_2$ recorded at 70 eV electron energy. The parent ion $[\text{Pt}(\text{CO})_2\text{Br}_2]^+$ has the highest intensity and also the bare Pt^+ ion is observed with significant intensity. Other fragments with appreciable intensity are $[\text{Pt}(\text{CO})\text{Br}_2]^+$, $[\text{PtBr}_2]^+$, $[\text{Pt}(\text{CO})_2]^+$ and $[\text{PtBr}]^+$.

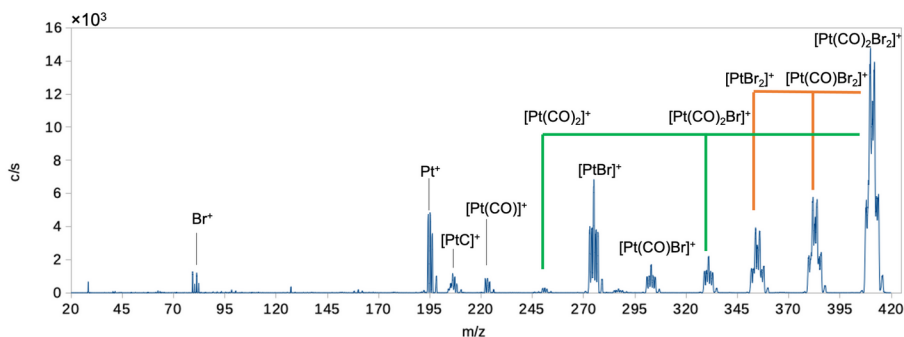


Figure 4.8. Positive ion mass spectrum of $\text{Pt}(\text{CO})_2\text{Br}_2$ recorded at 70 eV incident electron energy. The sequential loss of two Br ligands is shown with green lines, while the sequential loss of two CO ligands is shown with orange lines. Reprinted from ref. [127] under open access Creative Commons CC BY 4.0 license.

Table 4.3 shows the normalized relative contributions of the individual fragments, in DEA and DI, and the weighted average loss per incident for bromine and carbonyl. The relative DEA contributions were calculated by integrating the ion yield curves from

about 0 to 10 eV. The relative DI contributions were obtained by integrating over the isotope distribution of the respective fragment peaks in the positive ion mass spectrum. In table 4.3, the DEA and DI relative contributions are normalized to the integrated intensities of $[\text{Pt}(\text{CO})\text{Br}_2]^-$ and the parent ion ($[\text{Pt}(\text{CO})_2\text{Br}_2]^+$), respectively. The average CO and Br loss per incident in DEA and DI was calculated by weighting the respective relative contributions of the CO-loss or Br-loss fragments by the number of carbonyls or Br ligands lost in the respective incidents.

Table 4.3. Relative fragment contributions in DI and DEA to $\text{Pt}(\text{CO})_2\text{Br}_2$, average weighted CO loss per DEA and DI incident and average weighted Br loss per DI incident. The values are taken from ref. [127] under open access Creative Commons CC BY 4.0 license.

Fragments	Relative DI contributions	Relative DEA Contributions
$[\text{Pt}(\text{CO})_2\text{Br}_2]^+$	1	-
$[\text{Pt}(\text{CO})\text{Br}_2]^{+/-}$	0.38	1
$[\text{PtBr}_2]^{+/-}$	0.23	0.76
$[\text{Pt}(\text{CO})_2\text{Br}]^+$	0.10	-
$[\text{Pt}(\text{CO})\text{Br}]^{+/-}$	0.07	0.02
$[\text{PtBr}]^{+/-}$	0.25	0.004
$[\text{Pt}(\text{CO})_2]^+$	0.01	-
$[\text{Pt}(\text{CO})]^+$	0.02	-
$[\text{PtC}]^+$	0.04	-
$[\text{Pt}]^+$	0.11	-
$[\text{Br}]^{+/-}$	0.01	0.05
Average CO loss	0.7	1.4
Average Br loss	0.3	0.04

From the relative DEA contributions, we estimated an average CO loss of 1.4 and an average Br loss of only 0.04. From the relative DI contributions, we estimated an average CO loss of 0.7 and an average Br loss of 0.3. These values are in agreement with the average CO and Cl losses calculated for $\text{Pt}(\text{CO})_2\text{Cl}_2$ in the previous study.

In the electron-induced decomposition study on $\text{Pt}(\text{CO})_2\text{Cl}_2$ on surfaces [22], it was found that at low electron doses, CO loss is the dominating process and the average CO loss was estimated to be around 1-2.

In the comparative deposition study [23] on $\text{Pt}(\text{CO})_2\text{Cl}_2$ and $\text{Pt}(\text{CO})_2\text{Br}_2$, the deposits in the UHV electron-induced deposition experiments contained 1:2 platinum halogen ratio. Therefore, it appears that DEA rather than DI is the dominating process in the initial decomposition step in the surfaces and deposition studies.

4.2 Dissociative electron attachment to model compounds for application in chemoradiotherapy

4.2.1 Motivation and previous work

In recent years there has been a considerable progress in cancer treatment. However, hypoxic tumors, i.e., tumors poorly supplied with oxygen, still represent a challenge in anticancer therapy. The low supply of O₂ in malignant tissues makes chemotherapy and radiotherapy less effective [131–133]. Chemoradiotherapy, i.e., the concomitant administration of radiosensitizers and radiation, is a common way to more effectively treat hypoxic tumors. Such radiosensitizers are electron-affinic chemotherapeutic agents that sensitize cancer cells to radiation. In the sensitization process, LEEs are expected to play an important role [134; 135]. In fact, when ionizing radiation interacts with biological tissues, a significant amount of LEEs (<20 eV) are generated. The energy distribution of these LEEs peaks at or below 10 eV and has an appreciable contribution close to 0 eV and a long high energy tail [8]. Such LEEs, before undergoing solvation, which occurs in about 10⁻¹² s [136], can interact with DNA or a radiosensitizer producing radical fragments that can cause bond ruptures in DNA. In 2000, Boudaiffa et al. [9] showed that DEA processes can trigger single and double-strand breaks in DNA.

In this context, in the last decade, there have been several studies on LEE interactions with DNA components [12; 137–140] and radiosensitizers [11; 13–15; 141–143].

It has been found that halogenated nucleobases present high DEA cross-sections at low electron energies and significantly sensitize DNA to radiation induced damaged [14; 15; 142; 143]. Rackwitz et al. [143] have shown that substitution of adenine with 2-fluoro adenine in DNA oligonucleotides significantly enhances the strand-brake efficiency through DEA. This molecule is the key component in fludarabine, an important chemotherapeutic that has also been suggested for use in chemoradiotherapy as a radiosensitizer [144]. Furthermore, it was found that DEA to the oxygen-mimetic radiosensitizers 2-nitroimidazole and 4(5)-nitroimidazole effectively fragments these molecules [141; 142]. Making radiosensitizers more susceptible to DEA is thus an interesting path to follow to enhance their therapeutic efficiency.

In this context, we conducted DEA studies on pentafluorothiophenol (PFTP), 2-fluoro thiophenol (2-FTP) and pentafluorobenzoic acid (PFBA), which may serve as model compounds for rational tailoring of more efficient radiosensitizers.

As has been discussed in the introduction, DEA reactions don't exclusively proceed via single bond ruptures. Sometimes, bond ruptures are accompanied by the formation of new bonds. In such cases, the system can gain energy from the formation of new bonds and thus new reaction channels, otherwise inaccessible at low electron energies, can be promoted. An important example of this process is given by the DEA reactions that lead to neutral HF formation [25; 26; 54; 55; 145]. The formation of this chemical bond supplies 5.9 eV to the system and can fuel new reaction channels. Such HF formation was also observed in DEA to 2-fluoro adenine and it was suggested that energy gained from the HF bond enthalpy may provide the thermochemical prerequisite for this DEA channel [143].

The first systematic studies on HF formation in DEA was conducted by Ómarsson et al.

[25; 26] in 2012. In those studies, the authors investigated the HF formation through DEA to pentafluorotoluene (PFT), pentafluoroaniline (PFA), and pentafluorophenol (PFP). They suggested that in such systems the HF formation is promoted by the formation of an intermediate intramolecular hydrogen bond, $X-H\cdots F$, which is supported by the polarization of the $X-H$ bond. The HF formation was found to be exothermic in the case of PFP and endothermic in the case of PFA and PFT. The exothermicity of the HF formation from PFP was, in this study, partly attributed to the subsequent rearrangement of the charge retaining fragment into a pentagonal structure.

In the context of promoting DEA reaction channels in radiosensitizers, exothermic HF formation may be considered as a way to enhance the susceptibility of such compounds towards low-energy electrons.

This motivated us to investigate the HF formation upon DEA to PFTP and 2-FTP (Article III). While both the compounds have the prerequisites to form the intermediate $X-H\cdots F$, the perfluorination in PFTP significantly influences the thermochemistry of the process. In fact, the perfluorination increases the electron affinity of the charge-retaining fragment, $[M-HF]^-$, and this supplies additional energy into the DEA process lowering the thermochemical thresholds. Furthermore, the perfluorination of aromatic rings enhances the DEA efficiency by strongly lowering the σ^* MOs as compared to the π^* MOs. Electron capture in to the σ^* MO can lead to direct dissociation. However, the same process from the electron occupation of the π^* MOs is symmetrically forbidden in the C_{2v} point group and requires efficient vibronic coupling.

It's worth mentioning that in PFTP the HF formation will not be supported by the polarization of the $S-H$ bond because S is less electronegative than N and O atoms. However, the $S-H$ bond is much longer and weaker than the $O-H$ bond, so the H atom in PFTP is more labile than in PFP.

We also extended these investigations to pentafluorobenzoic acid (PFBA), a good candidate for HF formation upon DEA (Article IV). In a recent study, Zawadzki et al. [27] investigated DEA to the native benzoic acid (BA), the aromatic benzene ring with a carboxylic acid group. They found five main dissociation channels, $[M-H]^-$, $C_6H_5^-$, OH^- , $COOH^-$, and O^- , which are related to the fragmentation of the $COOH$ group. In that study, the authors pointed out that the fragmentation mechanism of an aromatic ring molecule, under low-energy electron interactions, can be strongly influenced by binding large molecular structures to the ring.

A comparison between BA and PFBA is very informative because also the perfluorination could affect the fragmentation mechanism of the molecule.

Furthermore, in this section, a small comparison of the DEA processes in $Pt(CO)_2X_2$ ($X=Cl, Br$) with those in $Pt(NH_3)Cl_2$, i.e., cisplatin is offered.

Cisplatin is a FDA approved chemotherapeutic agent which has been widely used in the treatment of testicular and ovarian cancer [146–149], metastatic breast cancer [150; 151] and other various types of tumors, such as metastatic melanoma [152] and carcinoma of the head and neck [153].

The mode of cytotoxic action of cisplatin lies in its ability to form cisplatin–DNA adducts with the guanine bases blocking DNA replication [154; 155]. Inside the cell, CDDP loses the two Cl atoms due to hydrolysis and forms a Pt-acqua complex. The resulting complex, then, binds to the N7 position of guanine bases. Other than directly

acting as a chemotherapeutic agent, cisplatin also acts as a radiosensitizer. It has been shown that the concomitant application of radiation and platinum-based chemotherapy enhances the cell-killing effect of radiation [156; 157]. Zheng et al. [33] showed that when cisplatin-DNA complexes are irradiated, the single and double-strand breaks induced by the LEEs significantly increase. This sensitization to LEEs has been attributed to DEA processes.

4.2.2 Comparison between $\text{Pt}(\text{CO})_2\text{Br}_2$ and $\text{Pt}(\text{NH}_3)_2\text{Cl}_2$ in DEA

In 2009, a DEA study on cisplatin was performed by Kopyra et al. [28]. The authors found that the dominant DEA channels involve the cleavage of the Pt–halogen bonds, leading to the formation of $[\text{Pt}(\text{NH}_3)_2\text{Cl}]^-$, Cl^- and $[\text{Pt}(\text{NH}_3)_2]^-$. As has been previously shown, the dominant DEA channels in $\text{Pt}(\text{CO})_2\text{Cl}_2$ and $\text{Pt}(\text{CO})_2\text{Br}_2$ involve the loss of one and two CO ligands, while the halogen loss is negligible.

The fact that DEA efficiently triggers the loss of both Cl atoms in cisplatin is interesting. The Pt–NH₃ bond, similar to the Pt–CO bond, is much weaker than the Pt–Cl bond. With DFT calculations, Kopyra et al. [28] found the respective bond energies to be 1.5 eV for the Pt–NH₃ and 3.3 eV for the Pt–Cl.

At the $\omega\text{B97X-D3/ma-def2-TZVP}$ level of theory, we derived a halogen–Pt bond of 3.3 eV for $\text{Pt}(\text{CO})_2\text{Cl}_2$ and 2.8 eV for $\text{Pt}(\text{CO})_2\text{Br}_2$, while the Pt–CO bond energy was found to be 1.5 eV.

The authors of the DEA study on cisplatin also found that the LUMO involved in the electron capture has a repulsive σ^* character along all the ligands. Therefore, electron occupation of the LUMO allows direct Pt–Cl dissociation.

As has been previously discussed, the LUMO involved in electron attachment to $\text{Pt}(\text{CO})_2\text{X}_2$, where X is the halogen ligand, has π^* character and therefore, direct dissociation from the respective anionic ground state is symmetry forbidden and requires effective vibronic coupling. However, our study on $\text{Pt}(\text{CO})_2\text{Br}_2$ also shows that weakening the Pt–halogen bond by substitution with heavier halogens, increases the efficiency of the dissociation of the halogens in the DEA process. It may be worth considering substitution with heavier halogens in further optimization of cisplatin.

4.2.3 HF formation from pentafluorothiophenol and 2-fluorothiophenol upon dissociative electron attachment

Figure 4.9 shows the optimized ground state geometry of PFTP (left) and 2-FFTP (right) at the B3LYP D3BJ/aug-cc-pVTZ level of theory.

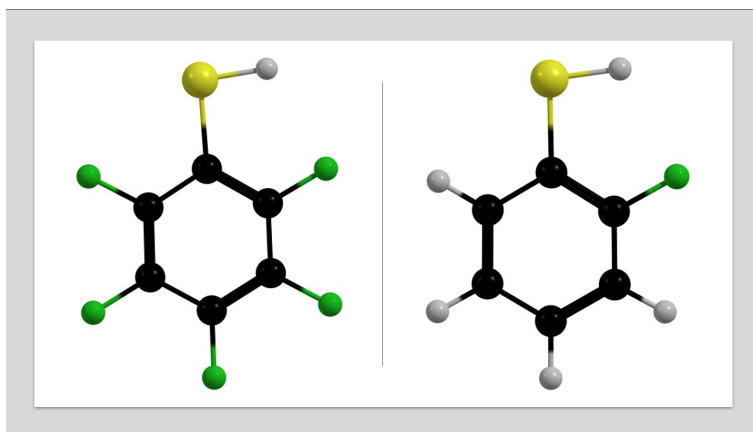


Figure 4.9. Optimized ground state geometry of PFTP (left) and 2-FFTP (right) at the B3LYP D3BJ/aug-cc-pVTZ level of theory. The colors of the atoms are assigned as follow: S: Yellow, C: Black, H: gray, F: green

Figure 4.10 shows the DEA ion yield curves for observed anionic fragments from PFTP and Figure 4.11 shows these from 2-FFTP. DEA to PFTP leads to HF formation $[M - HF]^-$, H loss $[M - H]^-$ and SH loss $[M - SH]^-$.

In PFTP, the most dominant DEA channel is the neutral HF formation ($[M - HF]^-$). The DEA ion yield curve for this process displays a significant contribution at 0 eV, indicating that this process is exothermic. A less intense contribution peaking at around 4.7 eV is also observed in the $[M - HF]^-$ yield curve.

Similar to the $[M - HF]^-$ and $[M - H]^-$ formations, the ion yield curve for the SH loss shows a low energy contribution centered at around 0.8 eV, and a less intense higher-lying contribution centered at around 4 eV.

In DEA to 2-FFTP, HF formation, i.e. $[M - HF]^-$ and H loss, i.e. $[M - H]^-$, are also observed. The respective ion yield curves for these processes show the maximum intensity at around 1.0 eV. Differently from PFTP, HF formation from 2-FFTP occurs with a relative cross-section that is three orders of magnitude lower than that for the H loss. The relative cross section for $[M - HF]^-$ formation from PFTP is five orders of magnitude higher than that for $[M - HF]^-$ formation from 2-FFTP.

The onset of the ion yield curve for the HF formation from 2-FFTP is at around 0.5 eV. Therefore this process is expected to be endothermic.

The ion yield curve for the H loss from 2-FFTP presents a low energy shoulder at around 0 eV. We attributed this contribution to "hot band" transitions or I^- ($m/z = 127$) from some contaminations containing iodine. The other observed DEA channel in 2-FFTP is the formation of S^- . The DEA ion yield curve for this process has the maximum

intensity at around 0.6 eV and is two orders of magnitude lower than that for $[M - H]^-$ formation from this compound.

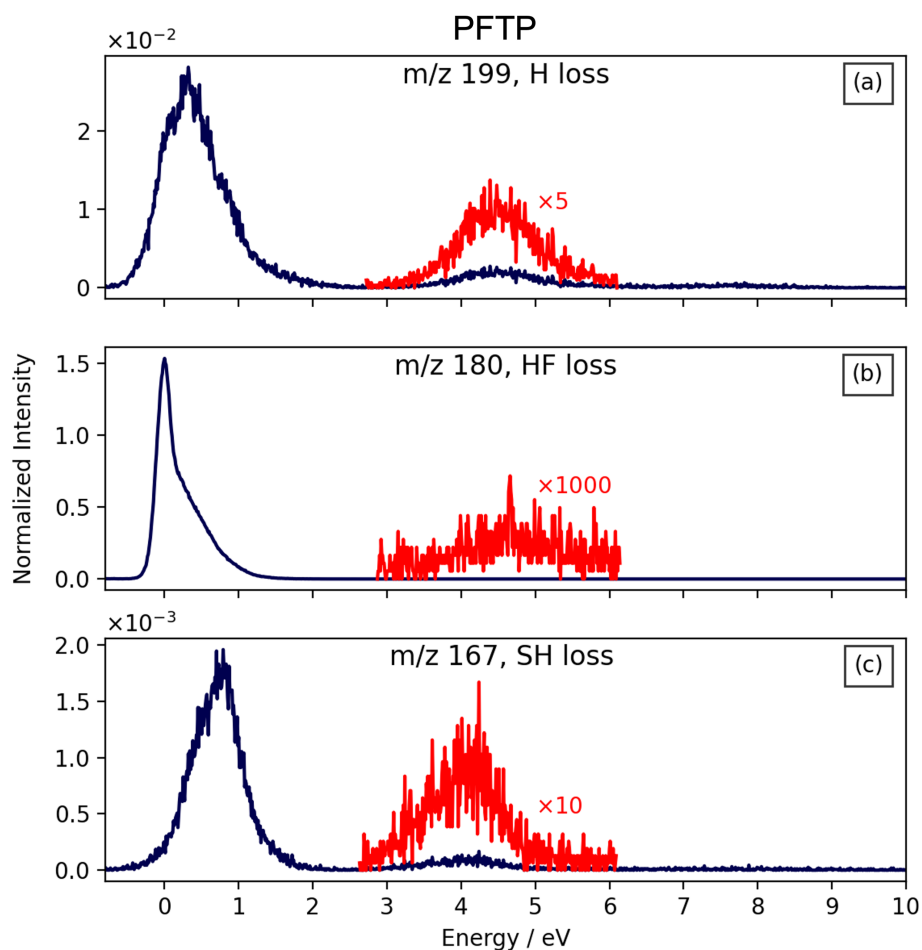


Figure 4.10. Negative ion yield curves from PFTP for the DEA channels: (a) H loss, (b) HF loss, and (c) SH loss. The ion yield curves are normalized with respect to the target gas pressure and the formation of SF_6^- from SF_6 at 0 eV as described in the method section 27. Adapted from ref [158] under open access Creative Commons CC BY 4.0 license.

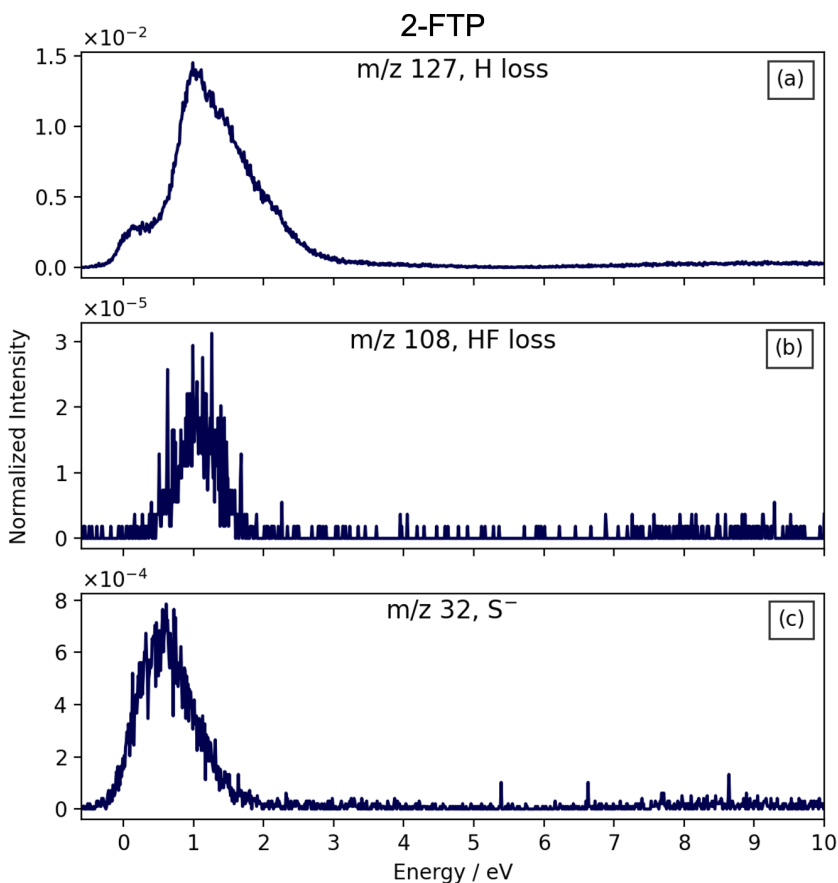


Figure 4.11. Negative ion yield curves from 2-FTP for the DEA channels: (a) H loss, (b) HF loss, and (c) S⁻ formation. The ion yield curves are normalized with respect to the target gas pressure and the formation of SF₆⁻ from SF₆ at 0 eV as described in the method section 27. Adapted from ref [158] under open access Creative Commons CC BY 4.0 license.

The calculated thermochemical thresholds for the DEA processes in PFTP and 2-FTP, calculated at the B3LYP D3BJ/aug-cc-pVTZ level of theory, are reported in Table 4.4.

Similarly, exothermic HF loss at 0 eV was observed in DEA experiments to PFP [25; 26]. In those studies, the calculated threshold for direct HF loss from PFP was found to be endothermic. However, considering a subsequent rearrangement of the anion into a pentagonal structure, the process was found to be exothermic by 0.19 eV at the B2PLYP/aug-pc-2 level of theory.

Following this finding, for the HF formation from PFTP and 2-FTP, we additionally calculated the respective thermochemical thresholds considering the rearrangement of the aromatic ring into a pentagonal structure as represented in Figure 4.12.

Table 4.4. Calculated thresholds at the B3LYP D3BJ/aug-cc-pVTZ level of theory. Geometry optimizations were performed at the same level of theory. All values are taken from ref [158] under open access Creative Commons CC BY 4.0 license.

m/z	Fragment	ΔE_{th}
PFTP		
199	$[M - H]^- / C_6F_5S^-$	0.13
180	$[M - HF]^- / C_6F_4S^-$	-0.29
180	* $[M - HF]^- / C_5F_4CS^-$	-0.35
167	$[M - SH]^- / C_6F_5^-$	0.32
2-FTP		
127	$[M - H]^- / C_6H_4FS^-$	0.84
108	$[M - H]^- / C_6H_4S^-$	0.42
108	* $[M - H]^- / C_5H_4CS^-$	0.28
32	S^-	0.14

* Calculated threshold considering the rearrangement of the ring after the HF formation

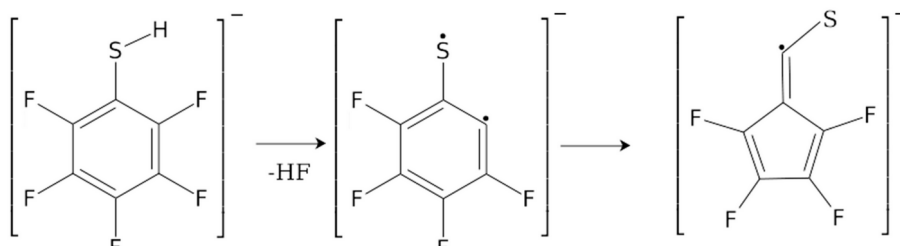


Figure 4.12. Representation of the rearrangement of the phenyl ring after the neutral HF loss upon DEA to PFTP and 2-FTP. The figure shows this for PFTP as an example. After the HF loss, the phenyl ring rearranges into a 5-membered ring with exocyclic-CS. This rearrangement was hypothesized to occur for PFP in the previous DEA studies on PFP, PFA and PFT [25; 26]. Reprinted from ref [158] under open access Creative Commons CC BY 4.0 license.

At the B3LYP D3BJ/aug-cc-pVTZ level of theory, we found that direct HF formation, i.e., without involving the rearrangement of the ring, is exothermic by 0.29 eV. Considering the ring rearrangement, we found the threshold to be lowered to -0.35 eV. At the same level of theory, we also found that direct HF formation from PFP is, in fact, exothermic by 0.33 eV. Therefore, it appears that exothermic HF formation from these compounds can occur as a direct process without involving the rearrangement of the

phenyl ring. Additionally, we calculated the thresholds for HF formation from PFTP and PFP at higher levels of theory, ω B97X-D3/aug-cc-pVTZ, ω B97X-D3/aug-cc-pVQZ, and DLPNO-CCSD(T)/aug-cc-pVQZ, obtaining qualitatively the same results. These values are reported as supplementary information with Article III.

In the case of 2-FTP, direct HF loss is endothermic by 0.42 eV and considering the ring rearrangement we found the threshold to be 0.28 eV.

In order to explore the dynamics involved in the HF formation from PFTP and 2-FTP, we calculated the minimum energy path using the Nudged Elastic Band method with transition state (TS) optimization (NEB-TS) [92].

The calculated reaction paths are reported in Article III along with a detailed discussion. They show that the ring rearrangement, after HF formation, proceeds through an energy barrier of 1.24 eV, in the case of PFTP, and 2.3 eV in the case of 2-FTP.

Similarly, the minimum energy path for the HF formation from PFP shows that the ring rearrangements must overcome an energy barrier close to 2 eV [26].

Therefore, according to our thermochemical threshold calculations and rearrangements barriers estimated from the minimum energy paths, we conclude that HF formation upon DEA at the 0 eV threshold to PFP, PFTP and 2-FTP can occur as a direct process without ring rearrangement.

Furthermore, the comparison between PFTP and 2-FTP shows that the perfluorination in PFTP plays an important role in the exothermic HF formation. This is understandable since the perfluorination increases the electron affinity of the charge-retaining fragment. In addition, as previously discussed, it is well known that the perfluorination of aromatic rings strongly lowers the σ^* MOs as compared to the π^* MOs due to the strong inductive effect of fluorine [159]. The low-lying σ^* MOs decrease in energy with increasing fluorination and this is called perfluoro effect [160; 161].

In regard to DEA to these compounds, this is important as while electron occupation of the σ^* orbital can lead to direct dissociation, the same process is symmetrically forbidden from the π^* MOs in the C_{2v} point group [162] and requires $\pi^* - \sigma^*$ coupling in order to proceed. This is similar to the comparison between cisplatin and $Pt(CO)_2Cl_2$, where, while dissociation from the σ^* LUMO of cisplatin can occur as a direct process, dissociation from the π^* LUMO of $Pt(CO)_2Cl_2$ is symmetrically forbidden and requires vibronic coupling. In polyfluorinated benzene anions, this coupling can be provided by the pseudo-Jahn-Teller (pJT) effect [163; 164].

In Article III, the nature of the low-lying LUMOs involved in DEA to PFTP and 2-FTP is extensively discussed. The ordering of the LUMOs was determined through vertical electron attachment energy (VAE) calculations using the EOM-EA-CCSD method with B3LYP orbitals and aug-cc-pVTZ basis set. We noted that the VAEs to these systems strongly depend on the level of theory that is used to perform the calculations; however, the order of the LUMOs is reliable. Figure 4.13 shows the LUMO and LUMO+1 of PFTP.

We found that the LUMO of PFTP has σ^* character. This MO is antibonding along the C–F coordinates and, therefore, can support the HF loss upon DEA. The LUMO+1 of PFTP, on the other hand, has π^* character and according to Jordan et al. practices [165] we labeled it $b_1(\pi^*)$. While this MO is antibonding along the C–F coordinates, dissociation from this state is symmetrically forbidden and requires $\pi^* - \sigma^*$ coupling, which may be provided by the pJT effect.

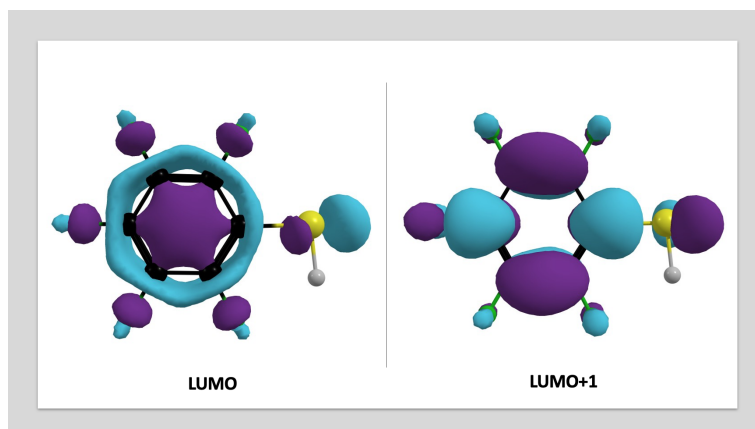


Figure 4.13. Contour plots of the LUMO and LUMO+1 of PFTP (B3LYP orbitals). The LUMO has a σ^* character, while LUMO + 1 has π^* character. Redrawn from the original source in ref. [158] under open access Creative Commons CC BY 4.0 license.

The low energy contribution in the ion yield curve of $[M - HF]^-$ from PFTP is asymmetric towards higher energies and we attributed this asymmetry to overlapping contributions from two distinct resonances. This is signified with a combined fit of a normal Gaussian curve, for the lower energy contribution peaking at 0 eV, and a skewed Gaussian for the higher energy overlapping contribution. The combined fit is shown in Figure 4.14.

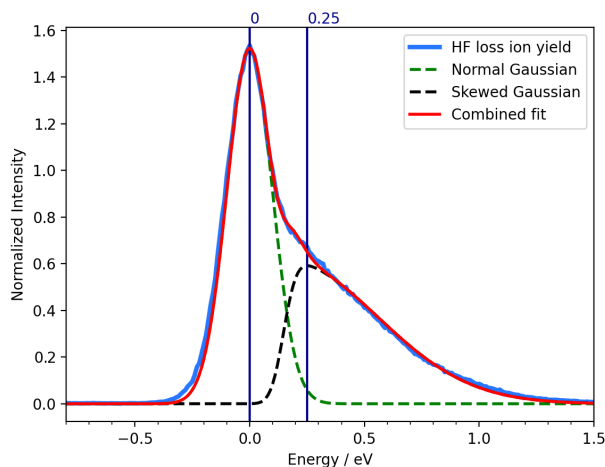


Figure 4.14. Combined fit of a Gaussian and skewed Gaussian to the ion yield curve of $[M - HF]^-$ from DEA to PFTP. Reprinted from ref [158] under open access Creative Commons CC BY 4.0 license.

The skewed Gaussian was chosen in order to reproduce the asymmetry of the higher energy component due to the energy dependency of the autodetachment lifetime. At higher energies, the autodetachment process becomes more significant, resulting in a lower survival probability with respect to dissociation. This, in turn, gives asymmetric peaks towards higher energies in the DEA ion yield curves.

We attributed the first low energy resonance, which peaks at 0 eV, to electron occupation of the σ^* LUMO and the second higher-lying resonance to electron occupation of the $b_1(\pi^*)$ LUMO+1. The lower intensity of the second resonance can be explained considering the required $\pi^* - \sigma^*$ coupling for dissociation from the $b_1(\pi^*)$ state extends the dissociation time and thus favoring autodetachment. Dissociation from the σ^* state, on the other hand, is a direct process. In addition, the energy dependence of the autodetachment process also plays a role.

For 2-FTP, we found that both the LUMO and LUMO+1, shown in Figure 4.15, have π^* character and according to the Jordan et al.[165] nomenclature, they correlate with the $a_2(\pi^*)$ and $b_1(\pi^*)$ MOs. The condition for HF formation from 2-FTP is provided by the $b_1(\pi^*)$ LUMO+1, which is anti-bonding along the C–F coordinate. However, dissociation from the $b_1(\pi^*)$ state requires $\pi^* - \sigma^*$ coupling. The low relative cross section for the HF formation from 2-FTP could be the result of the high threshold for this process and an inefficient coupling between the LUMO+1 and the C–F σ^* state.

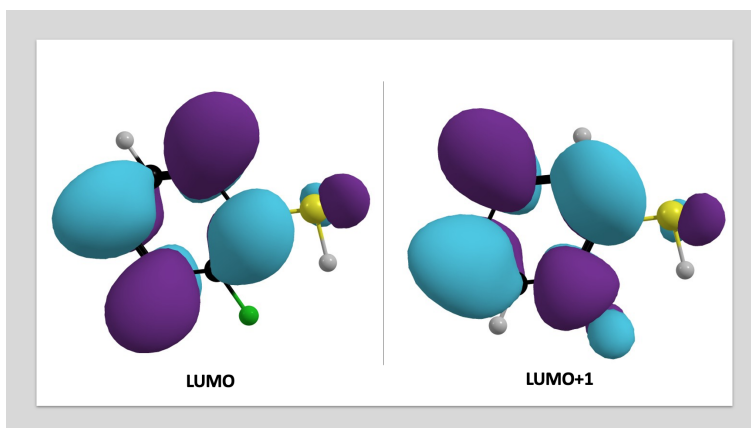


Figure 4.15. Contour plots of the LUMO and LUMO + 1 of 2-FTP (B3LYP orbitals). Both LUMOs have π^* character. Redrawn from the original source in ref. [158] under open access Creative Commons CC BY 4.0 license.

Our study shows that the perfluorination in PFTP plays an important role in exothermic HF formation and also lowers the lowest σ^* MO below the respective π^* MOs, allowing directing dissociation at electron energies close to 0 eV. Furthermore, the efficient coupling of the π^* MO with the low lying σ^* MO, provided by the pJT, is important in order to have HF formation from the π^* MO in PFTP. In the context of tailoring new radiosensitizers that are more susceptible towards DEA, both HF formation and perfluorination can be considered as potential tools for a bottom-up design.

4.2.4 Dissociative electron attachment to pentafluorobenzoic acid

Figure 4.16 shows the optimized ground state geometry of PFBA at the B3LYP D3BJ/aug-cc-pVTZ level of theory.

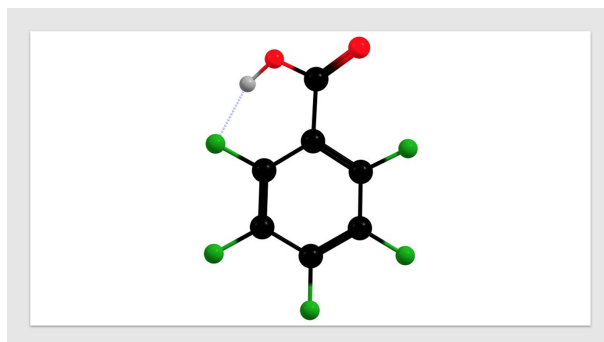


Figure 4.16. Optimized ground state geometry of PFBA at the B3LYP D3BJ/aug-cc-pVTZ level of theory. The colors of the atoms are assigned as follow: O: red, C: Black, H: gray, F: green

Figure 4.17 shows the negative ion yield curves for the most efficient DEA channels observed in dissociative electron attachment to pentafluorobenzoic acid (PFBA) in the energy range from about 0 eV to about 10 eV. These are the neutral HF formation $[M - HF]^-$ (m/z 192), the neutral CO_2 loss leading to the formation of $[M - CO_2]^-$ (m/z 184) and the loss of both HF and CO_2 leading to the formation of $[M - HF - CO_2]^-$ (m/z 164). Hydrogen loss is also observed (not shown here), but with about four orders of magnitude lower intensity, when compared to that of $[M - HF - CO_2]^-$.

All the curves show a pronounced peak at or close to 0 eV. On the contrary, in the previous study on DEA to the native benzoic acid (BA) [27], with the exception of the ion yield curve for H loss peaking at around 1.34 eV, all ion yields curves peak at energies above 5 eV. In that study, the ion yield curve for $[M - H]^-$ shows the highest intensity. The second most intense fragment is $[M - COOH]^-$. This neutral COOH loss has also a complementary DEA channel given by the loss of $COOH^-$. In our experiment, the HF formation efficiently prevails over the H loss. We attribute this to the strong intramolecular hydrogen bond $COO-H \cdots F$ which sterically hinders the H loss and promotes the HF formation. The relative, maximum cross-section for $[M - HF - CO_2]^-$ is an order of magnitude higher than those for $[M - HF]^-$ and $[M - CO_2]^-$. It appears clear that this DEA channel strongly competes with the $[M - HF]^-$ and $[M - CO_2]^-$ formation. As will be discussed below, we found all the channels to be exothermic. The $[M - HF - CO_2]^-$ ion yield curve appears broad and asymmetric towards higher energies as compared to the high energy tail observed for $[M - HF]^-$ and $[M - CO_2]^-$, suggesting the presence of an underlying resonance along the high energy tail.

The absence of the high energy tail in the $[M - HF]^-$ and $[M - CO_2]^-$ ion yield curves can be explained considering the thermochemistry involved in the DEA processes. Since

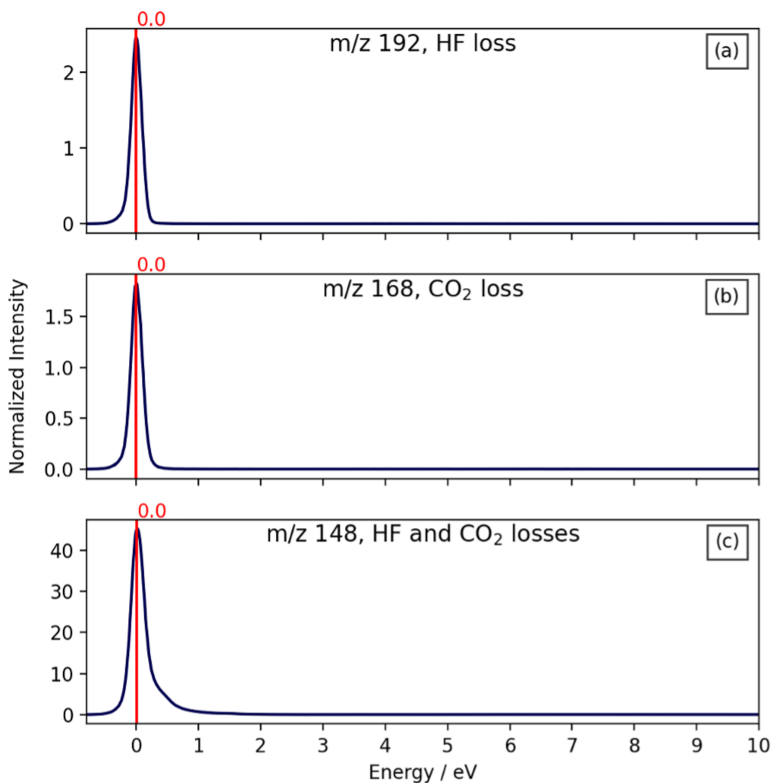


Figure 4.17. Negative ion yield curves from PFBA for the DEA channels: (a) HF loss, (b) CO₂ loss, and (c) HF and CO loss. The ion yield curves are normalized with respect to the target gas pressure and the formation of SF₆⁻ from SF₆ at 0 eV according to Equation 27 in Method section. Adapted from Article IV.

the HF loss is exothermic, the excess energy in the [M – HF]⁻ fragment makes its survival probability low above the threshold, with respect to further CO₂ loss. The same applies to the exothermic CO₂, where the excess energy in the [M – CO₂]⁻ could be channeled into further HF loss. This is specially true as in our experimental setup, the extraction times is about 10 μs and the flight time through the quadrupole is about 50 μs. Therefore, only ions that are formed within the first 10 μs and survive the flight through the quadrupole are observed.

The asymmetric nature of the [M – HF – CO₂]⁻ peak is better visualized with a combined fit of a normal gaussian and a skewed gaussian, shown in Figure 4.18. The underlying resonance along the high energy tail is expected to be asymmetric towards high energies due to the energy dependency of the autodetachment lifetime. In the lower

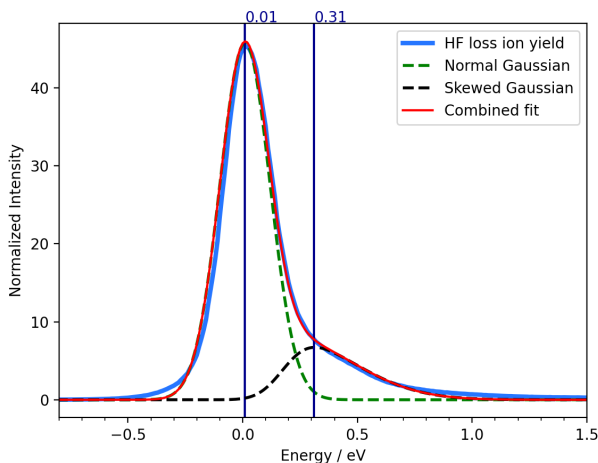


Figure 4.18. Combined fit of a Gaussian and skewed Gaussian to the ion yield curve for $[M - HF - CO_2]^-$ formed upon DEA to PFBA. Adapted from Article IV.

energy contribution, centered at 0.01 eV, the energy dependence of the autodetachment process is not expected to significantly affect the shape of the peak, therefore we used a normal gaussian for the fit of this contribution. The fit agrees well with an underlying contribution centered at around 0.31 eV in the DEA yield. We associate the low-energy contribution of the peak, at 0 eV, to electron attachment to the LUMO, and the high-energy contribution to electron attachment to LUMO+1. The respective SOMOs are shown in Figure 4.19. Contrary to PFTP, the SOMO of PFBA shows π^* character and according to the Jordan et al. [165][48] nomenclature, it can be labeled as b_1 (π^*). This MO is antibonding along the C–F and C–O bonds. The SOMO+1 shows σ^* character and C–F dissociation can directly proceed from the SOMO+1. This process from the SOMO is symmetry forbidden within the C_{2v} group and requires effective coupling within the σ^* C–F coordinates. As we previously discussed, in fluorinated mono-substituted benzenes, this is provided by the pseudo Jahn-Teller effect. At the B3LYP D3BJ/aug-cc-pVTZ level of theory, the vertical attachment energy (VAE) for the anion ground state was found to be -0.52 eV, while for the first excited anion state we derived a value of 0.4 eV using a Δ SCF approach. The SOMO doesn't show antibonding character along the C–CO₂H, however, CO₂ loss may proceed through vibrational redistribution.

Table 4.5 lists the calculated thresholds (ΔE_{th}) for the most efficient DEA processes. As we did in the previous investigation of DEA to PFTP and 2-FTP, for the HF formation from PFBA, we also calculated the threshold considering the rearrangement of the benzene ring into a pentagonal ring after the HF loss. The optimized geometry of this pentagonal structure is shown in Figure 4.20.

Surprisingly, while we found direct HF loss to be exothermic by 0.81 eV, the subsequent rearrangement of the ring makes the process endothermic by 0.54 eV.

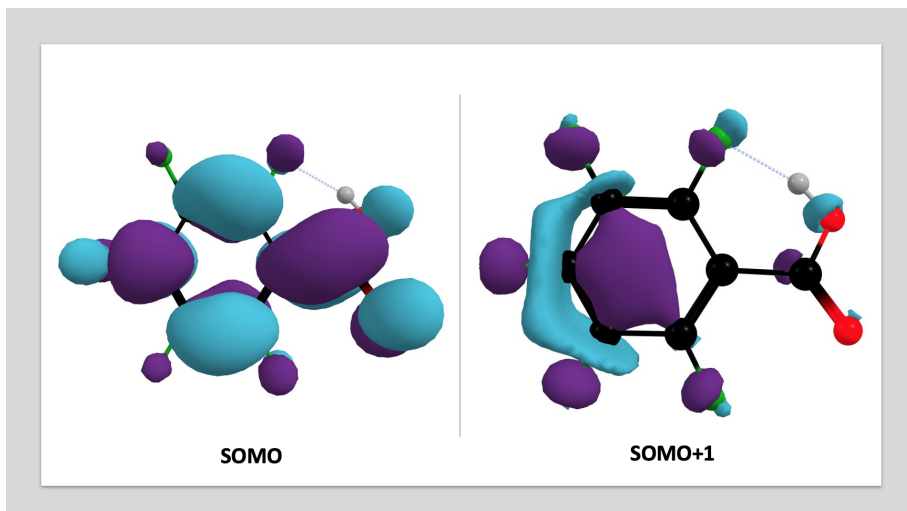


Figure 4.19. Contour plot of the SOMO and SOMO+1 of PFBA. The SOMO was calculated at the B3LYP D3BJ/aug-cc-pVTZ level of theory. The SOMO+1 was obtained with a Δ SCF approach at the same level of theory.

Table 4.5. Calculated thresholds at the B3LYP D3BJ/aug-cc-pVTZ level of theory. Geometry optimizations were performed at the same level of theory.

m/z	Fragment	ΔE_{th}
192	$[M - HF]^- / C_6F_4COO^-$	-0.81
192	* $[M - HF]^- / C_5F_4CCOO^-$	0.54
168	$[M - CO_2]^- / C_6F_5H^-$	-1.48
148	$[M - HF - CO_2]^- / C_6F_5H^-$	-0.21

* Calculated threshold considering the rearrangement of the ring after the HF formation

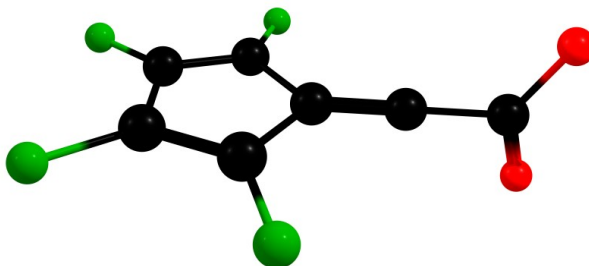


Figure 4.20. Pentagonal structure of PFBA after HF loss upon DEA. The structure was optimized at the B3LYP D3BJ/aug-cc-pVTZ. Adapted from Article IV.

In the previous BA study [27], the authors found the thresholds for the complementary DEA channels $[M - \text{COOH}]^-$ and COOH^- to be 3.25 eV and 2.78 eV, respectively. For the $[M - \text{COOH}]^-$ channel, considering a further dissociation of COOH into CO_2 and H , they derived a threshold of 3.31 eV at the B3LYP/aug-cc-pVTZ level of theory. For comparison, we calculated the threshold for the eventual complementary $[M - \text{COOH}]^-$ and COOH^- losses upon DEA to PFBA and we found both to be endothermic. For $[M - \text{COOH}]^-$ we obtained a threshold of 0.66 eV, while for the COOH^- loss we obtained a threshold of 2.49 eV. According to our calculations, CO_2 loss with hydrogen transfer to the vacated carbon is exothermic by 1.48 eV. It appears clear that the CO_2 loss is a more favorable DEA channel as compared to the COOH loss. The $[M - \text{CO}_2]^-$ channel leads to the formation of pentafluorobenzene radical anion. The complementary DEA channel leading to the formation CO_2^- is a closed channel because CO_2 has a negative electron affinity and, therefore, does not form a stable anion. In the previous study on DEA to BA, the $[M - \text{CO}_2]^-$ channel wasn't observed because the respective counter fragment, the benzene ring, has negative electron affinity and does not form a stable anion.

Supporting our approach in the comparison of PFTP and 2-FTP, the current study on PFBA shows that the DEA efficiency and the DEA path may be controlled by means of molecular design. Specifically, more extensive fragmentation may be achieved through HF loss and perfluorination.

5 Summary and outlook

In this Ph.D. thesis, the role of low-energy electron interactions in decomposition of FEBID precursors and model compounds for application in chemoradiotherapy has been discussed. In the DI study on $(\eta^3\text{-C}_3\text{H}_5)\text{Ru}(\text{CO})_3\text{Br}$, we reported the experimental AEs and the calculated thresholds. A good agreement was obtained between the experimental and theoretical values, except for the calculated values for the loss of the allyl group and the loss of this group and one CO, which are considerably lower than the respective experimental AEs. The most likely explanation for this discrepancy is the presence of a kinetic shift in the allyl loss channel due to the poor lability of this group. In an effort to improve the performance of FEBID precursors, gas-phase studies of DEA and DI are commonly conducted to understand the fragmentation mechanism of adsorbed precursor molecules upon electron beam impact. However, DEA or DI to this compound in the gas phase don't explain the observed behavior of $(\eta^3\text{-C}_3\text{H}_5)\text{Ru}(\text{CO})_3\text{Br}$ in the surface science and FEBID experiments. It is possible that ligand-surface-interactions slower the the loss of allyl ligand more than the CO loss.

In the case of $\text{Pt}(\text{CO})_2\text{Br}_2$ and $\text{Pt}(\text{CO})_2\text{Cl}_2$, the comparison of gas phase studies with surface and deposition studies suggests that DEA rather than DI is dominating in the initial decomposition step. The DEA studies on $\text{Pt}(\text{CO})_2\text{Br}_2$ and $\text{Pt}(\text{CO})_2\text{Cl}_2$ have been compared to a recent DEA study on cisplatin, which is as a chemotherapeutic agent that also acts as a radiosensitizer. Interesting, while the dominant DEA channels in $\text{Pt}(\text{CO})_2\text{Br}_2$ and $\text{Pt}(\text{CO})_2\text{Cl}_2$ are the loss of one and two CO ligands, the dominant DEA channels in cisplatin are the loss of one and two Cl atoms. In the context of chemoradiotherapy treatment, we hypothesized that it may be in principle possible to promote DEA reaction channels in radiosensitizers through perfluorination and HF formation. We conducted experimental and theoretical studies on DEA to PFTP, 2-FTP and PFBA. The comparison between PFTP and 2-FTP showed the important role of the perfluorination in making the HF formation exothermic. In PFTP, the perfluorination lowers the thermochemical threshold for the HF formation and also lowers σ^* MO below the respective π^* MOs. In PFBA we observed four main DEA channels: $[\text{M} - \text{H}]^-$, $[\text{M} - \text{HF}]^-$, $[\text{M} - \text{CO}_2]^-$ and $[\text{M} - \text{CO}_2 - \text{HF}]^-$. We reported the ion yield curves for the $[\text{M} - \text{HF}]^-$, $[\text{M} - \text{CO}_2]^-$ and $[\text{M} - \text{CO}_2 - \text{HF}]^-$. The respective thermochemical thresholds for these three channels were found to be exothermic. The comparison between BA and PFBA showed that the perfluorination affects the fragmentation mechanism of the molecule promoting new reaction channels.

Our studies have shown the important role of gas-phase experiment in characterizing the LEE interactions with FEBID precursors and model compounds for application in chemoradiotherapy. Specifically, the systematic investigation of LEE interactions with molecules with different functionalizations is of fundamental importance for a bottom-

up approach in the design of new efficient FEBID precursors and radiosensitizers. We have shown that perfluorination and HF formation in PFTP and PFBA enhance the DEA efficiency. It may be valuable to explore this path in the case of FEBID precursors.

References

- [1] O. Ingólfsson, editor. *Low-Energy Electrons*. Jenny Stanford Publishing, April 2019.
- [2] L.G. Christophorou. *Electron–Molecule Interactions and their Applications*. Academic Press, 1984.
- [3] W.F. van Dorp and C.W. Hagen. A critical literature review of focused electron beam induced deposition. *Journal of Applied Physics*, 104(8):081301, 2008.
- [4] I. Utke, P. Hoffmann, and J. Melngailis. Gas-assisted focused electron beam and ion beam processing and fabrication. *Journal of Vacuum Science & Technology B: Microelectronics and Nanometer Structures Processing, Measurement, and Phenomena*, 26(4):1197–1276, 2008.
- [5] I. Utke. *Nanofabrication using focused ion and electron beams : principles and applications*. Oxford University Press, Oxford New York, 2011.
- [6] W.F. Van Dorp, B. Van Someren, C.W. Hagen, K. Pieter, and C. Peter. Approaching the resolution limit of nanometer-scale electron beam-induced deposition. *Nano Letters*, 5(7):1303–1307, July 2005.
- [7] R.M. Thorman, R.T.P. Kumar, D. H.Fairbrother, and O. Ingólfsson. The role of low-energy electrons in focused electron beam induced deposition: four case studies of representative precursors. *Beilstein Journal of Nanotechnology*, 6:1904–1926, 2015.
- [8] S.M. Pimblott and J.A. LaVerne. Production of low-energy electrons by ionizing radiation. *Radiation Physics and Chemistry*, 76(8):1244–1247, 2007. Proceedings of the 11th Tihany Symposium on Radiation Chemistry.
- [9] B. Boudarffa, P. Cloutier, D. Hunting, M.A. Huels, and L. Sanche. Resonant formation of dna strand breaks by low-energy (3 to 20 ev) electrons. *Science*, 287(5458):1658–1660, 2000.
- [10] A. Kumar, D. Becker, A. Adhikary, and M.D. Sevilla. Reaction of electrons with dna: Radiation damage to radiosensitization. *International Journal of Molecular Sciences*, 20(16), 2019.
- [11] J. Ameixa, E. Arthur-Baidoo, R. R. Meißner, S. Makurat, W. Kozak, K. Butowska, F. Ferreira da Silva, J. Rak, and S. Denifl. Low-energy electron-induced decomposition of 5-trifluoromethanesulfonyl-uracil: A potential radiosensitizer. *The Journal of Chemical Physics*, 149(16):164307, 2018.
- [12] H.D. Flosadóttir, B. Ómarsson, I. Bald, and O. Ingólfsson. Metastable decay of dna components and their compositions - a perspective on the role of reactive electron scattering in radiation damage. *Eur. Phys. J. D*, 66(1):13, 2012.
- [13] R. Meißner, L. Feketeová, A. Bayer, P. Limão-Vieira, and S. Denifl. Formation of negative and positive ions in the radiosensitizer nimorazole upon low-energy

- electron collisions. *The Journal of Chemical Physics*, 154(7):074306, 2021.
- [14] A.M. Scheer, K. Aflatooni, G.A. Gallup, and P.D. Burrow. Bond breaking and temporary anion states in uracil and halouracils: Implications for the dna bases. *Phys. Rev. Lett.*, 92:068102, Feb 2004.
- [15] J.Kopyra, A. Keller, and I. Bald. On the role of fluoro-substituted nucleosides in dna radiosensitization for tumor radiation therapy. *RSC Adv.*, 4:6825–6829, 2014.
- [16] M.C. Boyer, N. Rivas, A.A. Tran, C.A. Verish, and C.R. Arumainayagamb. The role of low-energy (20ev) electrons in astrochemistry. *Surface Science*, 652:26–32, 2016. Insights into Surface Phenomena: In Honor of John T. Yates Jr.
- [17] L.G. Christophorou and J.K. Olthoff. *Electron Interactions with Plasma Processing Gases*. Special Publication (NIST SP), National Institute of Standards and Technology, Gaithersburg, MD, 1998-08-01 00:08:00 1998.
- [18] M. Rezaee, R.P. Hill, and D.A. Jaffray. The Exploitation of Low-Energy Electrons in Cancer Treatment. *Radiation Research*, 188(2):123 – 143, 2017.
- [19] R.M. Thorman, J.A. Brannaka, L. McElwee-White, and O. Ingólfsson. Low energy electron-induced decomposition of (3-c3h5)ru(co)3br, a potential focused electron beam induced deposition precursor with a heteroleptic ligand set. *Phys. Chem. Chem. Phys.*, 19:13264–13271, 2017.
- [20] R.M. Thorman, R. Bjornsson, and O. Ingólfsson. Computational study of dissociative electron attachment to -allyl ruthenium (II) tricarbonyl bromide. *The European Physical Journal D*, 70(8), August 2016.
- [21] J.A. Spencer, J.A. Brannaka, M. Barclay, L. McElwee-White, and D.H. Fairbrother. Electron-induced surface reactions of 3-allyl ruthenium tricarbonyl bromide [(3-c3h5)ru(CO)3br]: Contrasting the behavior of different ligands. *The Journal of Physical Chemistry C*, 119(27):15349–15359, June 2015.
- [22] J.A. Spencer, Y. Wu, L. McElwee-White, and D.H. Fairbrother. Electron induced surface reactions of cis-pt(CO)₂Cl₂: A route to focused electron beam induced deposition of pure pt nanostructures. *Journal of the American Chemical Society*, 138(29):9172–9182, July 2016.
- [23] A. Mahgoub, H. Lu, R.M. Thorman, K. Preradovic, T. Jurca, L. McElwee-White, H. Fairbrother, and C.W. Hagen. Electron beam-induced deposition of platinum from pt(CO)₂Cl₂ and cis-pt(CO)₂Br₂. *Beilstein Journal of Nanotechnology*, 11:1789–1800, November 2020.
- [24] F. Ferreira da Silva, R.M. Thorman, R. Bjornsson, H. Lu, L. McElwee-White, and O. Ingólfsson. Dissociation of the febid precursor cis-pt(CO)₂Cl₂ driven by low-energy electrons. *Phys. Chem. Chem. Phys.*, 22:6100–6108, 2020.
- [25] Ómarsson B, E.H. Bjarnason, O. Ingólfsson, S. Haughey, and T.A. Field. Chemical control through dissociative electron attachment – a study on pentafluorotoluene, pentafluoroaniline and pentafluorophenol. *Chemical Physics Letters*, 539-540:7–10, 2012.
- [26] B. Ómarsson, E.H. Bjarnason, S.A. Haughey, T.A. Field, A. Abramov, P. Klüpfel, H. Jónsson, and O. Ingólfsson. Molecular rearrangement reactions in the gas phase triggered by electron attachment. *Phys. Chem. Chem. Phys.*, 15:4754–4766, 2013.
- [27] M. Zawadzki, P. Wierzbicka, and J. Kopyra. Dissociative electron attachment

- to benzoic acid ($C_7H_6O_2$). *The Journal of Chemical Physics*, 152(17):174304, 2020.
- [28] J. Kopyra, C. Koenig-Lehmann, I. Bald, and E. Illenberger. A single slow electron triggers the loss of both chlorine atoms from the anticancer drug cisplatin: Implications for chemoradiation therapy. *Angewandte Chemie*, 121(42):8044–8047, October 2009.
- [29] Yasuhiko Takeiri. Negative ion source development for fusion application (invited). *Review of Scientific Instruments*, 81(2):02B114, 2010.
- [30] R McAdams, A J T Holmes, D B King, E Surrey, I Turner, and J Zacks. Negative ion research at the culham centre for fusion energy (CCFE). *New Journal of Physics*, 18(12):125013, dec 2016.
- [31] A.Y. Wong, D.L. Mamas, and D. Arnush. Negative ion plasmas. *The Physics of Fluids*, 18(11):1489–1493, 1975.
- [32] Petra Swiderek. Fundamental processes in radiation damage of dna. *Angewandte Chemie International Edition*, 45(25):4056–4059, 2006.
- [33] F.A. Gianturco and R.R. Lucchese. Radiation damage of biosystems mediated by secondary electrons: Resonant precursors for uracil molecules. *The Journal of Chemical Physics*, 120(16):7446–7455, 2004.
- [34] W.T. Diamond, Y. Imahori, J.W. McKay, J.S.C. Wills, and H. Schmeing. Efficient negative-ion sources for tandem injection (invited). *Review of Scientific Instruments*, 67(3):1404–1409, 1996.
- [35] George J. Schulz. Resonances in electron impact on atoms. *Rev. Mod. Phys.*, 45:378–422, Jul 1973.
- [36] George J. Schulz. Resonances in electron impact on diatomic molecules. *Rev. Mod. Phys.*, 45:423–486, Jul 1973.
- [37] E.Illenberger and J. Momigny. *Gaseous Molecular Ions*. Steinkopff, Heidelberg, 1992.
- [38] J. P. Gauyacq and A. Herzenberg. The attachment of very slow electrons to polyatomic molecules. *Journal of Physics B: Atomic and Molecular Physics*, 17(6):1155–1171, mar 1984.
- [39] O. Ingólfsson, F. Weik, and E. Illenberger. Formation and decay of negative ion resonances in gaseous and condensed molecules. *International Reviews in Physical Chemistry*, 15(1):133–151, 1996.
- [40] M. Lezius, P. Scheier, and T.D. Märk. Free electron attachment to C_{60} and C_{70} . *Chemical Physics Letters*, 203(2):232–236, 1993.
- [41] I.I. Fabrikant, H. Hotop, and M. Allan. Elastic scattering, vibrational excitation, and attachment in low-energy electron- SF_6 scattering: Experiment and effective range theory. *Phys. Rev. A*, 71:022712, Feb 2005.
- [42] E. Vogt and G.H. Wannier. Scattering of ions by polarization forces. *Phys. Rev.*, 95:1190–1198, Sep 1954.
- [43] U. Hefter, R.D. Mead, P.A. Schulz, and W.C. Lineberger. Ultrahigh-resolution study of autodetachment in C_2^- . *Phys. Rev. A*, 28:1429–1439, Sep 1983.
- [44] K.R. Lykke, K.K. Murray, D.M. Neumark, and W.C. Lineberger. High-resolution studies of autodetachment in negative ions. *Philosophical Transactions of the Royal Society of London. Series A, Mathematical and Physical Sciences*, 324(1578):179–196, January 1988.

- [45] D.T. Birtwistle and A. Herzenberg. Vibrational excitation of N_2 by resonance scattering of electrons. *Journal of Physics B: Atomic and Molecular Physics*, 4(1):53–70, Jan 1971.
- [46] M. Fenzlaff, R. Gerhard, and E. Illenberger. Associative and dissociative electron attachment by SF_6 and SF_5Cl . *The Journal of Chemical Physics*, 88(1):149–155, 1988.
- [47] O. Ingólfsson, F. Weik, and E. Illenberger. The reactivity of slow electrons with molecules at different degrees of aggregation: gas phase, clusters and condensed phase. *International Journal of Mass Spectrometry and Ion Processes*, 155(1):1–68, 1996.
- [48] L.G. Christophorou and J.A.D Stockdale. Dissociative electron attachment to molecules. *The Journal of Chemical Physics*, 48(5):1956–1960, 1968.
- [49] W. E. Wentworth, R. George, and H. Keith. Dissociative thermal electron attachment to some aliphatic chloro, bromo, iodo compounds. *The Journal of Chemical Physics*, 51(5):1791–1801, 1969.
- [50] S. Matejcik, G. Senn, P. Scheier, A. Kiendler, A. Stamatovic, and T.D. Märk. Dissociative electron attachment cross section to $CHCl_3$ using a high resolution crossed beams technique. *The Journal of Chemical Physics*, 107(21):8955–8962, 1997.
- [51] L.G. Christophorou, R.N. Compton, and H.W. Dickson. Dissociative electron attachment to hydrogen halides and their deuterated analogs. *The Journal of Chemical Physics*, 48(5):1949–1955, 1968.
- [52] K.M. Ervin, I. Anusiewicz, P. Skurski, J. Simons, and W. C. Lineberger. The only stable state of O_2^- is the $X^2\Pi_g$ ground state and it (still!) has an adiabatic electron detachment energy of 0.45 eV. *The Journal of Physical Chemistry A*, 107(41):8521–8529, September 2003.
- [53] G.J. Schulz. Cross sections and electron affinity for O^- ions from O_2 , CO , and CO_2 by electron impact. *Phys. Rev.*, 128:178–186, Oct 1962.
- [54] B. Ómarsson, R. Björnsson, and O. Ingólfsson. Proton shuttling and reaction paths in dissociative electron attachment to o- and p-tetrafluorohydroquinone, an experimental and theoretical study. *The Journal of Physical Chemistry A*, 121(30):5580–5585, 2017. PMID: 28695738.
- [55] I. Dąbkowska, H.D. Flosadóttir, M. Orzol, S. Ptasinska, I. Bald, O. Ingólfsson, and E. Illenberger. Reactions in gas phase and condensed phase $c6f_5x$ ($x = nco, ch_2cn$) triggered by low energy electrons. *Phys. Chem. Chem. Phys.*, 11:5323–5330, 2009.
- [56] J. Simons and K.D. Jordan. Ab initio electronic structure of anions. *Chemical Reviews*, 87(3):535–555, June 1987.
- [57] H.S. Taylor, G.V. Nazarov, and A. Golebiewski. Qualitative aspects of resonances in electron—atom and electron—molecule scattering, excitation, and reactions. *The Journal of Chemical Physics*, 45(8):2872–2888, 1966.
- [58] J.N. Bardsley and F. Mandl. Resonant scattering of electrons by molecules. *Reports on Progress in Physics*, 31(2):471, 1968.
- [59] M. Allan. Study of triplet states and short-lived negative ions by means of electron impact spectroscopy. *Journal of Electron Spectroscopy and Related Phenomena*, 48(2):219–351, 1989.

- [60] L.G. Christophorou. The lifetimes of metastable negative ions I research sponsored by the energy research and development administration under contract with union carbide corporation. volume 46 of *Advances in Electronics and Electron Physics*, pages 55–129. Academic Press, 1978.
- [61] H. Hotop, M.W. Ruf, M. Allan, and I.I. Fabrikant. Resonance and threshold phenomena in low-energy electron collisions with molecules and clusters. In *Advances In Atomic, Molecular, and Optical Physics*, pages 85–216. Elsevier, 2003.
- [62] M. Cizek, J. Horacek, M. Allan, I. Fabrikant, and W. Domcke. Vibrational excitation of hydrogen fluoride by low-energy electrons: Theory and experiment. *Journal of Physics B Atomic Molecular and Optical Physics*, 36, 07 2003.
- [63] J.P. Gauyacq and A. Herzenberg. Nuclear-excited feshbach resonances in e+HCl scattering. *Phys. Rev. A*, 25:2959–2967, Jun 1982.
- [64] M. Allan. Vibrational structures in electron-CO₂ scattering below the $^2\Pi_u$ shape resonance. *Journal of Physics B: Atomic, Molecular and Optical Physics*, 35(17):L387–L395, August 2002.
- [65] T.D. Märk. Electron ionization. 2010.
- [66] G.H. Wannier. The threshold law for single ionization of atoms or ions by electrons. *Phys. Rev.*, 90:817–825, Jun 1953.
- [67] T. Fiegele, G. Hanel, I. Torres, M. Lezius, and T.D. Märk. Threshold electron impact ionization of carbon tetrafluoride, trifluoromethane, methane and propane. *Journal of Physics B Atomic Molecular Physics*, 33(20):4263–4283, October 2000.
- [68] D.W. Marquardt. An algorithm for least-squares estimation of nonlinear parameters. *Journal of the Society for Industrial and Applied Mathematics*, 11(2):431–441, 1963.
- [69] E.H. Bjarnason, B. Ómarsson and S. Engmann, F. H. Ómarsson, and O. Ingólfsson. Dissociative electron attachment to titanium tetrachloride and titanium tetraisopropoxide. *European Physical Journal D*, 68(5):121, May 2014.
- [70] P.W. Harland and J.C.J. Thynne. Autodetachment lifetimes, attachment cross sections, and negative ions formed by sulfur hexafluoride and sulfur tetrafluoride. *The Journal of Physical Chemistry*, 75(23):3517–3523, 1971.
- [71] D. Klar, M.W. Ruf, and H. Hotop. Attachment of electrons to molecules at mev resolution. *Australian journal of physics*, 45(3):263–292, 1992.
- [72] R.C. Wetzell, F.A. Baiocchi, T.R. Hayes, and R.S. Freund. Absolute cross sections for electron-impact ionization of the rare-gas atoms by the fast-neutral-beam method. *Phys. Rev. A*, 35:559–577, Jan 1987.
- [73] F. Neese. The orca program system. *WIREs Computational Molecular Science*, 2(1):73–78, 2012.
- [74] J.P. Perdew, K. Burke, and M. Ernzerhof. Generalized gradient approximation made simple. *Phys. Rev. Lett.*, 77:3865–3868, Oct 1996.
- [75] C. Adamo and V. Barone. Toward reliable density functional methods without adjustable parameters: The pbe0 model. *The Journal of Chemical Physics*, 110(13):6158–6170, 1999.
- [76] A.D. Becke. Density-functional thermochemistry. iii. the role of exact exchange. *The Journal of Chemical Physics*, 98(7):5648–5652, 1993.

- [77] C. Lee, W. Yang, and R.G. Parr. Development of the colle-salvetti correlation-energy formula into a functional of the electron density. *Phys. Rev. B*, 37:785–789, Jan 1988.
- [78] P.J. Stephens, F.J. Devlin, C.F. Chabalowski, and M.J. Frisch. Ab initio calculation of vibrational absorption and circular dichroism spectra using density functional force fields. *The Journal of Physical Chemistry*, 98(45):11623–11627, November 1994.
- [79] J.D. Chai and M. Head-Gordon. Long-range corrected hybrid density functionals with damped atom–atom dispersion corrections. *Phys. Chem. Chem. Phys.*, 10:6615–6620, 2008.
- [80] S. Grimme, J. Antony, S. Ehrlich, and H. Krieg. A consistent and accurate ab initio parametrization of density functional dispersion correction (dft-d) for the 94 elements h-pu. *The Journal of Chemical Physics*, 132(15):154104, 2010.
- [81] F. Weigend and R. Ahlrichs. Balanced basis sets of split valence, triple zeta valence and quadruple zeta valence quality for h to rn: Design and assessment of accuracy. *Phys. Chem. Chem. Phys.*, 7:3297–3305, 2005.
- [82] J. Zheng, X. Xu, and D.G. Truhlar. Minimally augmented karlsruhe basis sets. *Theoretical Chemistry Accounts*, 128(3):295–305, February 2011. Funding Information: This work was supported in part by the U. S. Department of Energy, Office of Basic Energy Sciences, under grant no. DE-FG02-86ER13579 and by the Air Force Office of Scientific Research under grant no. FA9550-08-1-0183.
- [83] R.A. Kendall, T.H. Dunning, and R.J. Harrison. Electron affinities of the first-row atoms revisited. systematic basis sets and wave functions. *The Journal of Chemical Physics*, 96(9):6796–6806, 1992.
- [84] D.E. Woon and T.H. Dunning. Gaussian basis sets for use in correlated molecular calculations. iii. the atoms aluminum through argon. *The Journal of Chemical Physics*, 98(2):1358–1371, 1993.
- [85] C. Riplinger and F. Neese. An efficient and near linear scaling pair natural orbital based local coupled cluster method. *The Journal of Chemical Physics*, 138(3):034106, 2013.
- [86] C. Riplinger, P. Pinski, U. Becker, E.F. Valeev, and F. Neese. Sparse maps—a systematic infrastructure for reduced-scaling electronic structure methods. ii. linear scaling domain based pair natural orbital coupled cluster theory. *The Journal of Chemical Physics*, 144(2):024109, 2016.
- [87] C. Riplinger, B. Sandhoefer, A. Hansen, and F. Neese. Natural triple excitations in local coupled cluster calculations with pair natural orbitals. *The Journal of Chemical Physics*, 139(13):134101, 2013.
- [88] M. Saitow, U. Becker, C. Riplinger, E.F. Valeev, and F. Neese. A new near-linear scaling, efficient and accurate, open-shell domain-based local pair natural orbital coupled cluster singles and doubles theory. *The Journal of Chemical Physics*, 146(16):164105, 2017.
- [89] A. Hellweg, C. Hättig, S. Höfener, and W. Klopper. Optimized accurate auxiliary basis sets for ri-mp2 and ri-cc2 calculations for the atoms rb to rn. *Theoretical Chemistry Accounts*, 117(4):587–597, 2007.
- [90] T.H. Dunning Jr. Gaussian basis sets for use in correlated molecular calculations. i. the atoms boron through neon and hydrogen. *The Journal of chemical physics*,

- 90(2):1007–1023, 1989.
- [91] D. Figgen, K.A. Peterson, M. Dolg, and H. Stoll. Energy-consistent pseudopotentials and correlation consistent basis sets for the 5 d elements hf-pt. *The Journal of chemical physics*, 130(16):164108, 2009.
- [92] V. Ásgeirsson, B.O. Birgisson, R. Bjornsson, U. Becker, F. Neese, C. Riplinger, and H. Jónsson. Nudged elastic band method for molecular reactions using energy-weighted springs combined with eigenvector following. *Journal of Chemical Theory and Computation*, 17(8):4929–4945, 2021.
- [93] P. Hohenberg and W. Kohn. Inhomogeneous electron gas. *Phys. Rev.*, 136:B864–B871, Nov 1964.
- [94] W. Kohn and L.J. Sham. Self-consistent equations including exchange and correlation effects. *Phys. Rev.*, 140:A1133–A1138, Nov 1965.
- [95] M.M. Quintal, A. Karton, M.A. Iron, A.D. Boese, and J.M.L. Martin. Benchmark study of DFT functionals for late-transition-metal reactions. *The Journal of Physical Chemistry A*, 110(2):709–716, October 2005.
- [96] T. Weymuth, E.P.A. Couzijn, P. Chen, and M. Reiher. New benchmark set of transition-metal coordination reactions for the assessment of density functionals. *Journal of Chemical Theory and Computation*, 10(8):3092–3103, July 2014.
- [97] M.P. Waller, H. Braun, N. Hojdis, and M. Bühl. Geometries of second-row transition-metal complexes from density-functional theory. *Journal of Chemical Theory and Computation*, 3(6):2234–2242, October 2007.
- [98] M. Weimer, F. Della Sala, and A. Görling. The kohn–sham treatment of anions via the localized hartree–fock method. *Chemical Physics Letters*, 372(3):538–547, 2003.
- [99] T. Bally and G.N. Sastry. Incorrect dissociation behavior of radical ions in density functional calculations. *The Journal of Physical Chemistry A*, 101(43):7923–7925, October 1997.
- [100] E. Runge and E.K.U. Gross. Density-functional theory for time-dependent systems. *Phys. Rev. Lett.*, 52:997–1000, Mar 1984.
- [101] M.E. Casida. Time-dependent density functional response theory for molecules. In *Recent Advances In Density Functional Methods: (Part I)*, pages 155–192. World Scientific, 1995.
- [102] M.E. Casida. Time-dependent density-functional theory for molecules and molecular solids. *Journal of Molecular Structure: THEOCHEM*, 914(1):3–18, 2009. Time-dependent density-functional theory for molecules and molecular solids.
- [103] S. Hirata and M. Head-Gordon. Time-dependent density functional theory within the tamm–dancoff approximation. *Chemical Physics Letters*, 314(3):291–299, 1999.
- [104] J.F. Stanton and R.J. Bartlett. The equation of motion coupled-cluster method. a systematic biorthogonal approach to molecular excitation energies, transition probabilities, and excited state properties. *The Journal of chemical physics*, 98(9):7029–7039, 1993.
- [105] M. Huth, F. Porrati, C. Schwalb, M. Winhold, R. Sachser, M. Dukic, J. Adams, and G. Fantner. Focused electron beam induced deposition: A perspective. *Beilstein Journal of Nanotechnology*, 3:597–619, August 2012.

- [106] J. Schaefer and J. Hoelzl. A contribution to the dependence of secondary electron emission from the work function and fermi energy. *Thin Solid Films*, 13(1):81–86, 1972.
- [107] A.P. Knights and P.G. Coleman. Secondary electron emission from ag(100) stimulated by positron and electron impact. *Applied Surface Science*, 85:43–48, 1995. Proceedings of the Sixth International Workshop on Slow-Positron Beam Techniques for Solids and Surfaces.
- [108] N. Silvis-Cividjian, C.W. Hagen, L.H.A. Leunissen, and P. Kruit. The role of secondary electrons in electron-beam-induced-deposition spatial resolution. *Microelectronic engineering*, 61:693–699, 2002.
- [109] A.P.J.M. Botman, D.A.M. De Winter, and J.J.L. Mulders. Electron-beam-induced deposition of platinum at low landing energies. *Journal of Vacuum Science & Technology B: Microelectronics and Nanometer Structures Processing, Measurement, and Phenomena*, 26(6):2460–2463, 2008.
- [110] J.H. Noh, M.G. Stanford, B.B. Lewis, J.D. Fowlkes, H. Plank, and P.D. Rack. Nanoscale electron beam-induced deposition and purification of ruthenium for extreme ultraviolet lithography mask repair. *Applied Physics A*, 117(4):1705–1713, August 2014.
- [111] J.M. Slaughter, D.W. Schulze, C.R. Hills, A. Mirone, R. Stalio, R.N. Watts, C. Tarrío, T.B. Lucatorro, M. Krumrey, P. Mueller, and C.M. Falco. Structure and performance of si/mo multilayer mirrors for the extreme ultraviolet. *Journal of Applied Physics*, 76(4):2144–2156, 1994.
- [112] J. Jurczyk, C.R. Brewer, O.M. Hawkins, M.N. Polyakov, C. Kapusta, L. McElwee-White, and I. Utke. Focused electron beam-induced deposition and post-growth purification using the heteroleptic ru complex (3-c3h5)ru(CO)3br. *ACS Applied Materials & Interfaces*, 11(31):28164–28171, July 2019.
- [113] G.D. Wilson, S. M. Bentzen, and P.M. Harari. Biologic basis for combining drugs with radiation. *Seminars in Radiation Oncology*, 16(1):2–9, 2006. Concurrent Radiation/Drug Regimens Current Future Horizons.
- [114] L. Kelland. The resurgence of platinum-based cancer chemotherapy. *Nature Reviews Cancer*, 7(8):573–584, July 2007.
- [115] D. Lebwohl and R. Canetta. Clinical development of platinum complexes in cancer therapy: an historical perspective and an update. *European Journal of Cancer*, 34(10):1522–1534, September 1998.
- [116] K. Landheer, S.G. Rosenberg, L. Bernau, P. Swiderek, I. Utke, C.W. Hagen, and D.H. Fairbrother. Low-energy electron-induced decomposition and reactions of adsorbed tetrakis(trifluorophosphine)platinum [pt(PF₃)₄]. *The Journal of Physical Chemistry C*, 115(35):17452–17463, August 2011.
- [117] M.N. Hedhili, J.H. Bredehoft, and P. Swiderek. Electron-induced reactions of mecptme₃ investigated by hreels. *The Journal of Physical Chemistry C*, 113(30):13282–13286, 2009.
- [118] J.D. Wnuk, J.M. Gorham, S.G. Rosenberg, W.F. van Dorp, Theodore E. Madey, C.W. Hagen, and D.H. Fairbrother. Electron induced surface reactions of the organometallic precursor trimethyl(methylcyclopentadienyl)platinum(IV). *The Journal of Physical Chemistry C*, 113(6):2487–2496, January 2009.
- [119] S. Engmann, M. Stano, S. Matejčík, and O. Ingólfsson. Gas phase low energy

- electron induced decomposition of the focused electron beam induced deposition (febid) precursor trimethyl (methylcyclopentadienyl) platinum(IV) (mecpPtMe₃). *Phys. Chem. Chem. Phys.*, 14:14611–14618, 2012.
- [120] O. May, D. Kubala, and M. Allan. Dissociative electron attachment to Pt(PF₃)₄—a precursor for focused electron beam induced processing (febip). *Phys. Chem. Chem. Phys.*, 14:2979–2982, 2012.
- [121] M. Zlatar, M. Allan, and J. Fedor. Excited states of Pt(PF₃)₄ and their role in focused electron beam nanofabrication. *The Journal of Physical Chemistry C*, 120(19):10667–10674, May 2016.
- [122] M. Rohdenburg, H. Boeckers, C.R. Brewer, L. McElwee-White, and P. Swiderek. Efficient NH₃-based process to remove chlorine from electron beam deposited ruthenium produced from (3-C₃H₅)Ru(CO)₃Cl. *Scientific Reports*, 10(1), July 2020.
- [123] M. Rohdenburg, P. Martinović, K. Ahlenhoff, S. Koch, D. Emmrich, A. Götzhäuser, and P. Swiderek. Cisplatin as a potential platinum focused electron beam induced deposition precursor: NH₃ ligands enhance the electron-induced removal of chlorine. *The Journal of Physical Chemistry C*, 123(35):21774–21787, August 2019.
- [124] Maicol Cipriani, Rachel M. Thorman, Christopher R. Brewer, Lisa McElwee-White, and Oddur Ingólfsson. Dissociative ionization of the potential focused electron beam induced deposition precursor -allyl ruthenium(II) tricarbonyl bromide, a combined theoretical and experimental study. *The European Physical Journal D*, 73(10), October 2019.
- [125] S.G. Rosenberg, M. Barclay, and D.H. Fairbrother. Electron beam induced reactions of adsorbed cobalt tricarbonyl nitrosyl (Co(CO)₃NO) molecules. *The Journal of Physical Chemistry C*, 117(31):16053–16064, July 2013.
- [126] S.G. Rosenberg, M. Barclay, and D.H. Fairbrother. Electron induced reactions of surface adsorbed tungsten hexacarbonyl (W(CO)₆). *Phys. Chem. Chem. Phys.*, 15:4002–4015, 2013.
- [127] M. Cipriani, S. Svavarsson, F.d.S. Ferreira, H. Lu, L. McElwee-White, and O. Ingólfsson. The role of low-energy electron interactions in cis-Pt(CO)₂Br₂ fragmentation. *International Journal of Molecular Sciences*, 22(16), 2021.
- [128] C. Desfrancois, H. Abdoul-Carime, and J.P. Schermann. Ground-state dipole-bound anions. *International Journal of Modern Physics B - IJMPB*, 10:1339–1395, 05 1996.
- [129] T. Sommerfeld. Dipole-bound states as doorways in (dissociative) electron attachment. *Journal of Physics: Conference Series*, 4:245–250, January 2005.
- [130] M. Stepanović, Y. Pariat, and M. Allan. Dissociative electron attachment in cyclopentanone, -butyrolactone, ethylene carbonate, and ethylene carbonate-d₄: Role of dipole-bound resonances. *The Journal of Chemical Physics*, 110(23):11376–11382, 1999.
- [131] K. Graham and E. Unger. Overcoming tumor hypoxia as a barrier to radiotherapy, chemotherapy and immunotherapy in cancer treatment. *International Journal of Nanomedicine*, Volume 13:6049–6058, October 2018.
- [132] S. Rockwell, I Dobrucki, E. Kim, S. Marrison, and V. Vu. Hypoxia and radiation therapy: Past history, ongoing research, and future promise. *Current Molecular*

- Medicine*, 9(4):442–458, May 2009.
- [133] A.L. Harris. Hypoxia — a key regulatory factor in tumour growth. *Nature Reviews Cancer*, 2(1):38–47, January 2002.
- [134] Y. Park, K. Polska, J. Rak, J.R. Wagner, and Léon Sanche. Fundamental mechanisms of DNA radiosensitization: Damage induced by low-energy electrons in brominated oligonucleotide trimers. *The Journal of Physical Chemistry B*, 116(32):9676–9682, August 2012.
- [135] T.F. M. Luxford, S.A. Pshenichnyuk, N.L. Asfandiarov, T. Perečko, M. Falk, and J. Kočišek. 5-nitro-2, 4-dichloropyrimidine as an universal model for low-energy electron processes relevant for radiosensitization. *International Journal of Molecular Sciences*, 21(21):8173, October 2020.
- [136] Herbert Morawetz. Radiation chemistry-principles and applications, farhataziz and michael a. j. rogers, eds. VCH, new york and germany, 1987, 641 pp. price.: *Journal of Polymer Science Part C: Polymer Letters*, 25(12):510–510, December 1987.
- [137] Jorge Kohanoff, Maeve McAllister, Gareth A Tribello, and Bin Gu. Interactions between low energy electrons and DNA: a perspective from first-principles simulations. *Journal of Physics: Condensed Matter*, 29(38):383001, August 2017.
- [138] E. Alizadeh, T.M. Orlando, and L. Sanche. Biomolecular damage induced by ionizing radiation: The direct and indirect effects of low-energy electrons on dna. *Annual Review of Physical Chemistry*, 66(1):379–398, 2015. PMID: 25580626.
- [139] I. Baccarelli, I. Bald, F.A. Gianturco, E. Illenberger, and J. Kopyra. Electron-induced damage of DNA and its components: Experiments and theoretical models. *Physics Reports*, 508(1-2):1–44, November 2011.
- [140] I. Bald and S. Denifl. The role of low-energy electrons in dna radiation damage. In *Low-Energy Electrons*, pages 285–340. Jenny Stanford Publishing, 2019.
- [141] K. Tanzer, L. Feketeová, Benjamin Puschnigg, Paul Scheier, Eugen Illenberger, and Stephan Denifl. Reactions in nitroimidazole triggered by low-energy (0b-/b2 eV) electrons: Methylation at n1-h completely blocks reactivity. *Angewandte Chemie International Edition*, 53(45):12240–12243, September 2014.
- [142] A.Ribar, K. Fink, M. Probst, S.E. Huber, L. Feketeová, and Stephan Denifl. Isomer selectivity in low-energy electron attachment to nitroimidazoles. *Chemistry - A European Journal*, 23(52):12892–12899, August 2017.
- [143] J. Rackwitz, J. Kopyra, I. Dąbkowska, K. Ebel, M.L. Ranković, A.R. Milosavljević, and I. Bald. Sensitizing DNA towards low-energy electrons with 2-fluoroadenine. *Angewandte Chemie International Edition*, 55(35):10248–10252, August 2016.
- [144] Vincent Grégoire, K Kian Ang, Jean-François Rosier, Marc Beauvain, Adam S Garden, Marc Hamoir, Walter N Hittelman, Yves Humblet, Fadlo R Khuri, Luka Milas, et al. A phase i study of fludarabine combined with radiotherapy in patients with intermediate to locally advanced head and neck squamous cell carcinoma. *Radiotherapy and oncology*, 63(2):187–193, 2002.
- [145] J. Langer, M. Stano, S. Gohlke, V. Foltin, S. Matejcik, and E. Illenberger. Reactions in trifluoroacetic acid (CF₃cooh) induced by low energy electron attachment. *Chemical Physics Letters*, 419(1-3):228–232, February 2006.

- [146] N. Hanna and L.H. Einhorn. Testicular cancer: A reflection on 50 years of discovery. *Journal of Clinical Oncology*, 32(28):3085–3092, October 2014.
- [147] E.H. Einhorn. Testicular cancer: an oncological success story. *Clinical Cancer Research*, 3(12):2630–2632, 1997.
- [148] G.V. Kondagunta, J. Bacik, A. Donadio, D. Bajorin, S. Marion, J. Sheinfeld, G.J. Bosl, and R.J. Motzer. Combination of paclitaxel, ifosfamide, and cisplatin is an effective second-line therapy for patients with relapsed testicular germ cell tumors. *Journal of Clinical Oncology*, 23(27):6549–6555, September 2005.
- [149] R.F. Ozols, B.N. Bundy, B.E. Greer, J.M. Fowler, D. Clarke-Pearson, R.A. Burger, R.S. Mannel, K.DeGeest, E.M. Hartenbach, and R. Baergen. Phase III trial of carboplatin and paclitaxel compared with cisplatin and paclitaxel in patients with optimally resected stage III ovarian cancer: A gynecologic oncology group study. *Journal of Clinical Oncology*, 21(17):3194–3200, September 2003.
- [150] G.W. Sledge, P.J. Loehrer, B.J. Roth, and L.H. Einhorn. Cisplatin as first-line therapy for metastatic breast cancer. *Journal of Clinical Oncology*, 6(12):1811–1814, December 1988.
- [151] N. Koshy, D. Quispe, R. Shi, R. Mansour, and G.V. Burton. Cisplatin–gemcitabine therapy in metastatic breast cancer: Improved outcome in triple negative breast cancer patients compared to non-triple negative patients. *The Breast*, 19(3):246–248, June 2010.
- [152] S.S. Legha, S. Ring, A. Bedikian, C. Plager, O. Eton, A.C. Buzaid, and N. Papadopoulos. Treatment of metastatic melanoma with combined chemotherapy containing cisplatin, vinblastine and dacarbazine (CVD) and biotherapy using interleukin-2 and interferon-. *Annals of Oncology*, 7(8):827–835, October 1996.
- [153] K.J. Cullen, Z. Yang, L. Schumaker, and Z. Guo. Mitochondria as a critical target of the chemotherapeutic agent cisplatin in head and neck cancer. *Journal of Bioenergetics and Biomembranes*, 39(1):43–50, February 2007.
- [154] E.R. Jamieson and S.J. Lippard. Structure, recognition, and processing of cisplatin-DNA adducts. *Chemical Reviews*, 99(9):2467–2498, August 1999.
- [155] M.H. Baik, R.A. Friesner, and S.J. Lippard. Theoretical study of cisplatin binding to purine bases: why does cisplatin prefer guanine over adenine? *Journal of the American Chemical Society*, 125(46):14082–14092, October 2003.
- [156] Lloyd R Kelland and Nicholas P Farrell. Platinum-based drugs in cancer therapy. 2000.
- [157] Y. Zheng, D.J. Hunting, P. Ayotte, and L. Sanche. Role of secondary low-energy electrons in the concomitant chemoradiation therapy of cancer. *Phys. Rev. Lett.*, 100:198101, May 2008.
- [158] M. Cipriani and O. Ingólfsson. Hf formation through dissociative electron attachment—a combined experimental and theoretical study on pentafluorothiophenol and 2-fluorothiophenol. *International Journal of Molecular Sciences*, 23(5), 2022.
- [159] C.R. Brundle, M.B. Robin, and N.A. Kuebler. Perfluoro effect in photoelectron spectroscopy. II. aromatic molecules. *Journal of the American Chemical Society*, 94(5):1466–1475, March 1972.
- [160] A.L. Hinde, D. Poppinger, and L. Radom. Ab initio study of the benzene radical anion. *Journal of the American Chemical Society*, 100(15):4681–4685, July

- 1978.
- [161] Arthur J. Birch, Alan L. Hinde, and Leo Radom. A theoretical approach to the birch reduction. structures and stabilities of the radical anions of substituted benzenes. *Journal of the American Chemical Society*, 102(10):3370–3376, May 1980.
- [162] T. Skalický, C. Chollet, N. Pasquier, and M. Allan. Properties of the π^* and σ^* states of the chlorobenzene anion determined by electron impact spectroscopy. *Physical Chemistry Chemical Physics*, 4(15):3583–3590, June 2002.
- [163] L.N. Shchegoleva, I.I. Bilkis, and P.V. Schastnev. Geometrical and electronic structure of fluoro-substituted benzene radical anions based on quantum chemical analysis of hyperfine interactions. *Chemical Physics*, 82(3):343–353, December 1983.
- [164] L.N. Shchegoleva, I.V. Beregovaya, and P.V. Schastnev. Potential energy surface of $C_6F_6^-$ radical anion. *Chemical Physics Letters*, 312(2-4):325–332, October 1999.
- [165] K.D. Jordan, J.A. Michejda, and P.D. Burrow. Electron transmission studies of the negative ion states of substituted benzenes in the gas phase. *Journal of the American Chemical Society*, 98(23):7189–7191, October 1976.

Article I

Dissociative ionization of the potential focused electron beam induced deposition precursor -allyl ruthenium(II) tricarbonyl bromide, a combined theoretical and experimental study

Maicol Cipriani, Rachel M. Thorman, Christopher R. Brewer, Lisa McElwee-White and Oddur Ingolfsson

The European Physical Journal D, 2019, 73, 227

Copyright © 2019, EDP Sciences / Società Italiana di Fisica / Springer-Verlag GmbH Germany, part of Springer Nature. Permission for reproduction in this thesis granted by the copyright owner.

Maicol Cipriani conducted all the computational work and major part of the data analysis. He wrote the first draft of the manuscript and contributed to editing until publication.

Dissociative ionization of the potential focused electron beam induced deposition precursor π -allyl ruthenium(II) tricarbonyl bromide, a combined theoretical and experimental study*†

Maicol Cipriani¹, Rachel M. Thorman², Christopher R. Brewer³, Lisa McElwee-White³, and Oddur Ingólfsson^{1,‡}¹ Science Institute and Department of Chemistry, University of Iceland, Dunhagi 3, 107 Reykjavík, Iceland² Department of Chemistry, Johns Hopkins University, Baltimore, USA³ Department of Chemistry, University of Florida, Gainesville, FL 32611-7200, USA

Received 18 March 2019 / Received in final form 26 July 2019

Published online 29 October 2019

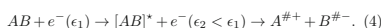
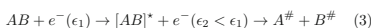
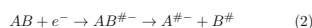
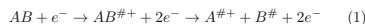
© EDP Sciences / Società Italiana di Fisica / Springer-Verlag GmbH Germany, part of Springer Nature, 2019

Abstract. Here we present a combined theoretical and experimental study on dissociative ionization of $(\eta^3\text{-allyl})\text{Ru}(\text{CO})_3\text{Br}$, a potential precursor for focused electron beam induced deposition. Experimental appearance energies are determined by electron impact ionization and relative cross sections for selected fragmentation channels are presented from their respective thresholds to about 70 eV incident electron energy. Threshold energies for individual fragmentation channels are computed at the hybrid density functional and coupled cluster level of theory and compared to the respective experimental appearance energies.

1 Introduction

Focused electron beam induced deposition (FEBID) is a nanofabrication technique with the capability of directly writing three-dimensional nanostructures by metal deposition on uneven surfaces with a tightly focused, high-energy electron beam [1–3]. Deposition is the result of electron induced reactions causing fragmentation of the precursor molecules, which are continuously supplied to the substrate surface. Ideally, FEBID precursors should dissociate completely upon interaction with the high-energy electron beam, creating pure deposits of well-defined composition confined to the area exposed to the electron beam. However, the interaction of a high-energy primary electron beam with a substrate produces backscattered and secondary electrons with a broad energy distribution. The energy distribution of the secondary electrons produced in this process generally ranges from close to 0 eV to about 100 eV, peaks below 10 eV and has a substantial value at energies close to 0 eV [4,5]. These low-energy secondary electrons may be significantly more plentiful at the point of interaction on the substrate surface than the high-energy primary electrons [1,6] and may cause fragmentation of the

precursor molecules [7–11]. Further, the low-energy electron induced fragmentation processes may have considerable cross sections (see e.g. Refs. [11,12] and references therein). Such low-energy electron induced fragmentation typically results in incomplete decomposition and ligand co-deposition, and is thus relevant to deposit purity. In fact, currently used FEBID precursors commonly lead to low purity deposits and deposits broadening beyond the dimension of the primary beam [1,2]. This is mainly due to the spatial distribution of the backscattered and thus low-energy secondary electrons. Generally, low-energy electrons can induce fragmentation through four distinct processes, as shown in equations (1)–(4): Dissociative Ionization (DI, (1)), Dissociative Electron Attachment (DEA, (2)), Neutral Dissociation (ND, (3)) and Dipolar Dissociation (DD, (4)).



Here the hash, #, indicates that the transient negative ion (TNI) and/or the fragments produced may be in an electronically and/or vibrationally excited state, while the asterisk, *, indicates an electronic excitation. In support of the efforts to develop high performance FEBID precursors, it is important to understand the energy dependence and the extent of these electron-induced processes

* Contribution to the Topical Issue “Dynamics of Systems on the Nanoscale (2018)”, edited by Ilko Bald, Ilia A. Solov'yov, Nigel J. Mason and Andrey V. Solov'yov.

† Supplementary material in the form of one pdf file available from the Journal web page at <https://doi.org/10.1140/epjd/e2019-100151-9>.

‡ e-mail: odduring@hi.is

with current and potential FEBID precursors, and to compare such data with their decomposition on surfaces and their actual performance under real FEBID conditions. In this context several studies on electron-induced decomposition of FEBID precursors in the gas phase under single collision conditions (see e.g. Refs. [11,13–16] and Refs. therein) and at surfaces under controlled UHV conditions have been conducted (see e.g. Refs. [17–19] and Refs. therein). The comparison of such gas phase and surface data has also been reported in collaborative studies (see e.g. Refs. [11,20]) and most recently this approach has been extended by comparing the gas phase decomposition of the bimetallic precursor $\text{HfFeCo}_3(\text{CO})_{12}$ with its decomposition under electron exposure at surfaces under controlled UHV conditions and its deposition performance under actual high-vacuum FEBID conditions [21].

In this context we have studied dissociative electron attachment (DEA) to $(\eta^3\text{-allyl})\text{Ru}(\text{CO})_3\text{Br}$ in detail [22,23], using this potential precursor as a model compound with three different types of ligands with distinctly different properties. The same compound has also been studied with regards to its fragmentation and deposition properties when adsorbed on a substrate surface and exposed to 500 eV electrons under controlled UHV conditions [24]. Most recently FEBID and reductive post purification of π -allyl ruthenium(II) tricarbonyl has also been reported [25], showing 23 at. % content in the initial deposition and 83 at. % after treatment with 2% hydrogen in a nitrogen gas. However, in these experiments significant volume reduction was observed after the purification step. These studies are particularly interesting as FEBID has been developed on a commercial scale for photo mask repair, and due to its fairly high transparency in the extreme ultraviolet regime, ruthenium is commonly used as a capping layer in the currently emerging EUVL masks [26]. Current Ru precursors are limited, and the only ones we are aware of are $\text{Ru}_3(\text{CO})_{12}$ [27] and bis(ethylcyclopentadienyl) ruthenium(II) [26,28] thus providing an additional motivation for our current study of $(\eta^3\text{-allyl})\text{Ru}(\text{CO})_3\text{Br}$. In the current contribution, we extend our previous studies on $(\eta^3\text{-allyl})\text{Ru}(\text{CO})_3\text{Br}$ by presenting the energy dependence of the relative cross sections for electron impact ionization and dissociative ionization of this potential FEBID precursor. Furthermore, we use the onset of the positive ion yield curves to estimate the ionization energy and appearance energies (AEs) for the principal dissociative ionization fragmentation channels. Further, threshold energies for the principal fragmentation channels, at the PBE0 [29,30] and DLPNO-CCSD(T) [31–33] level of theory are reported and compared to the respective experimental AEs.

2 Method

2.1 Quantum chemical calculations

All calculations were performed using ORCA [34]. All structures were optimized at the PBE0 (hybrid GGA functional) [29,30]/def2-TZVP [35] (using the def2 effective core potential [35] for the ruthenium core electrons), including the D3(BJ) dispersion correction by Grimme

et al. [36,37]. PBE0 and BP86 [38,39] (GGA functional) have both been found to give very reliable structures of transition metal complexes [40–42]. However, in thermochemical studies on transition metal compounds, PBE0 is often among the best performers [43–45]. Thus, for comparison PBE0 threshold values are reported along with the threshold values calculated at the coupled cluster level of theory. Also a comparison with threshold values calculated at the BP86 level of theory is given as Supplementary Material (Tab. S11). Harmonic vibrational frequencies were calculated at the PBE0/def2-TZVP level of theory. They were confirmed to be positive and were used to derive zero point vibrational energy and thermal energy corrections. Potential alternate isomers and spin states were investigated in order to make sure that the lowest energy state was indeed determined for each fragment. Coupled cluster calculations were performed on optimized geometries at the DLPNO-CCSD(T) [31–33] level of theory, using DZ/TZ extrapolation (def2-SVP [35] and def2-TZVP), auxiliary def2-QZVPP/C [46] basis set and ECPs: def2-ECP (for Ru). Quasi-restricted orbitals [47] were used as a reference in the coupled cluster calculations, which reduces spin contamination from the UHF step.

2.2 Experimental

Positive ion yield curves and mass spectra were recorded with an electron-molecule crossed beam setup that has been previously described in detail [48]. Only a brief description is given here. The crossed beam setup consists of a trochoidal electron monochromator (TEM), an effusive gas inlet and a commercial quadrupole mass spectrometer (QMS) (Hiden EPIC1000, Hiden Analytical, Warrington UK). The quasi mono-energetic electron beam is crossed with the effusive target gas, generated by sublimation of solid $(\eta^3\text{-allyl})\text{Ru}(\text{CO})_3\text{Br}$ at room temperature, entering the reaction region through a capillary tube. The typical background pressure was around 4×10^{-8} mbar and experiments were carried out with a target gas pressure in the range from 3 to 6×10^{-7} mbar in order to assure single collision conditions. The gas temperature is assumed to be that of the inlet system (room temperature), but the monochromator was heated to 120°C with two halogen lamps in order to avoid deposition of the target compound on the electrical lens components. The electron energy was calibrated using the SF_6^- formation from SF_6 at 0 eV electron energy and the energy resolution was estimated from the full width at half maximum of that signal and was found to be in the range from 120–140 meV in the current study. Mass spectra were recorded at fixed electron impact energy, typically 70–75 eV, by scanning through the relevant m/z range and ion yield curves were recorded at fixed m/z ratios by scanning through the relevant electron energy range. The ions formed in the crossed beam region were extracted by a small electric field (typically <1 V/cm) and focused onto the entrance aperture of the quadrupole mass spectrometer. The extraction time from the point of origin to the entrance of the QMS was in the range of 20–30 μs , depending on the voltage setting and the mass of the respective ions. To allow better

Table 1. Experimentally determined ionization and AEs for the principal fragments observed in electron impact ionization and fragmentation of (η^3 -allyl)Ru(CO)₃Br compared to the respective threshold values calculated at the PBE0/ def2-TZVP and at the DLPNO-CCSD(T) Extrapolate(2/3,def2) def2-TZVP/C level of theory (including ZPE and thermal energy of the neutral molecules).

Fragment	m/z	AE	PBE0 / def2-TZVP	DLPNO-CCSD(T) Extrapolate(2/3, def2) def2-QZVPP/C
$(\pi\text{-C}_3\text{H}_5)\text{Ru}(\text{CO})_3\text{Br}^+$	306	$8.6 \pm 0.6(\pm 0.6)$	7.99	8.20
$(\pi\text{-C}_3\text{H}_5)\text{Ru}(\text{CO})_2\text{Br}^+$	278	$9.9 \pm 0.5(\pm 0.1)$	9.43	9.57
$(\pi\text{-C}_3\text{H}_5)\text{Ru}(\text{CO})\text{Br}^+$	250	$10.8 \pm 0.5(\pm 0.2)$	10.76	10.58
$(\pi\text{-C}_3\text{H}_5)\text{RuBr}^+$	222	$13.3 \pm 0.5(\pm 0.5)$	12.77	12.34
$\text{Ru}(\text{CO})_3\text{Br}^+$	265	$12.9 \pm 0.6(\pm 0.6)$	10.13	10.40
$\text{Ru}(\text{CO})_2\text{Br}^+$	237	$13.4 \pm 0.5(\pm 0.5)$	12.24	12.29
$\text{Ru}(\text{CO})\text{Br}^+$	209	$15.7 \pm 0.5(\pm 0.5)$	15.31	15.59
RuBr^+	181	$16.6 \pm 0.6(\pm 0.6)$	17.65	17.02
$(\pi\text{-C}_3\text{H}_5)\text{Ru}^+$	143	$15.9 \pm 0.5(\pm 0.1)$	15.15	14.33
RuC^+	114	$17.4 \pm 0.5(\pm 0.4)$	21.96*(18.6**)	20.44*(17.11**)
Ru^+	102	$18.8 \pm 0.5(\pm 0.5)$	18.74	17.81

* Assuming that the carbon originates from the allyl group and that H₂ is formed in the fragmentation process (see Eq. (7))

** Assuming Br⁻ formation through dipolar dissociation, but otherwise as shown in equation (7).

comparison between the relative cross sections for individual fragmentation channels, the respective ion yields were normalized to the pressure, and the Ar⁺ ion yield from Ar at 70 eV incident electron energy recorded for each specific experiment:

$$I_{\text{Norm.}} = \left(\frac{I_{m/z}}{I_{\text{Ar}^+_{70\text{eV}}}} \right) \left(\frac{p_{\text{Ar}}}{p_{\text{Ru}}} \right). \quad (5)$$

Here $I_{m/z}$ is the spectral intensity of a particular m/z fragment from the (η^3 -allyl)Ru(CO)₃Br and p_{Ru} is the partial pressure of (η^3 -allyl)Ru(CO)₃Br during a particular measurement. $I_{\text{Ar}^+_{70\text{eV}}}$ and p_{Ar} are the measured Ar⁺ ion yields at 70 eV and the Ar pressure during the same measurement, respectively.

For determination of the appearance energies, the energy scale was recalibrated using the AE of Ar⁺ with Ar as the target gas [49]. The onset of the ion yields were fitted with a Wannier type function [50] of the form:

$$\begin{aligned} E \leq AE, f(x) &= b \\ E > AE, f(x) &= b + a(E - AE)^d. \end{aligned} \quad (6)$$

Here, E represents the energy of the incident electron, AE represents the appearance energy, b is a constant that considers the background signal, a is a scaling coefficient, and d is an exponential factor. Examples of these fits can be found in the ESI. The resulting ion yield curves for each fragment were obtained with the average of multiple scans recorded after each other. The fitting error from fitting equation (6) to these data sets ranges from <0.1 eV to about 0.6 eV. We, however, estimate the confidence limit to rather be in the range of 0.5 eV, as only one data set is behind each fit. These are the confidence limits reported, but in Table 1 and Table S11 the fitting errors are also reported in parenthesis. The (η^3 -allyl)Ru(CO)₃Br was synthesized as previously reported [51], purified by sublimation at 30°C and 90 mTorr and characterized by comparison with literature values [51,52].

3 Results and discussion

Figure 1 shows a positive ion mass spectrum resulting from electron impact ionization and dissociation of (η^3 -allyl)Ru(CO)₃Br at 75 eV incident electron energy. The mass spectrum is characterized by three progressions: i) loss of 1-3 CO ligands, ii) loss of the allyl group and 0-3 CO ligands, and iii) the loss of bromine and 0-3 CO ligands. The most prominent of these progressions is that of the loss of 1-3 CO ligands and interestingly, most of the intensity in the other two progressions is in the m/z ratios reflecting the loss of all three CO units along with the loss of the allyl group and bromine, respectively. In addition to these three regressions, RuCO⁺, RuC⁺ and Ru⁺ are observed with fair intensities. Figure 2 shows the respective positive ion yield curves for (a) the loss of 1-3 CO units and (b) the loss of the allyl group and 0-3 CO units. Such progressions of CO loss are commonly observed in dissociative ionization of carbonyl containing FEBID precursors. The formation of the bare metal ion with appreciable intensity is common in dissociative ionization of pure metal carbonyls, but is generally less efficient for other organometallic species (see for example Refs [53-55] and Refs therein). The ion yield in the energy range from 0-70 eV electron incident energy and an expansion of the threshold region is shown in the lower panels (c and d). For better comparison, the ion yield curve for the formation of the parent ion is shown in all panels and all ion yields are normalised with respect to pressure and the Ar⁺ ion yield measured at 70 eV, see equation (5). The experimental AEs for these fragments, determined by fitting equation (6) to the threshold region, are shown in Table 1 along with the respective threshold values calculated at the PBE0/ def2-TZVP and at the DLPNO-CCSD(T) Extrapolate(2/3,def2) def2-QZVPP/C level of theory. Also shown are the calculated threshold values for the loss of bromine (or bromide), three CO units and for the formation of Ru⁺, RuC⁺ and RuCO⁺. The experimental AEs and the calculated threshold values are

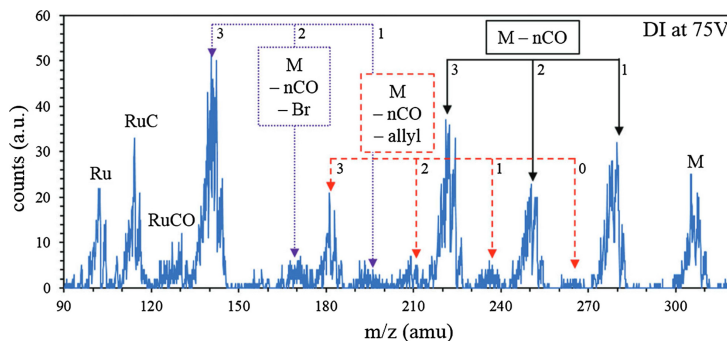


Fig. 1. Electron impact ionization mass spectrum of $(\eta^3\text{-allyl})\text{Ru}(\text{CO})_3\text{Br}$ recorded at 75 eV incident electron energy. The main channels observed are sequential carbonyl loss (1-3 CO), allyl loss accompanied by sequential carbonyl loss (0-3 CO), and bromine loss accompanied by sequential carbonyl loss (1-3 CO). Reproduced with permission from the CCPP Owner Societies.

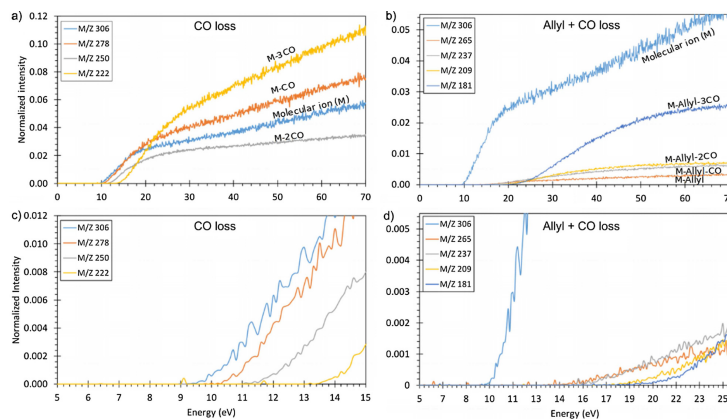


Fig. 2. Positive ion yield curves for (a) the loss of 1-3 CO units and (b) the loss of the allyl group and 0-3 CO units. The ion yield curves are shown in the incident electron energy range from below threshold to about 70 eV and an expansion of the threshold region is shown in the lower panels (c and d). All ion yields are normalised with respect to the pressure and the Ar^+ ion yield from Ar at 70 eV incident electron energy recorded for each specific experiment, see equation (5). For better comparison the ion yield curve for the formation of the parent ion is shown in all panels.

further compared in Figure 3, which also shows the optimized structures of the respective cationic fragments (the x,y,z files are provided with SI). Here, the AE for m/z 306 corresponds to the IE of $(\eta^3\text{-allyl})\text{Ru}(\text{CO})_3$ and is

experimentally determined to be 8.6 eV. The adiabatic IE calculated at the DLPNO-CCSD(T) Extrapolate(2/3, def2) def2-QZVPP/C level of theory is 8.20 eV. Considering the confidence limits of the experimental values, the

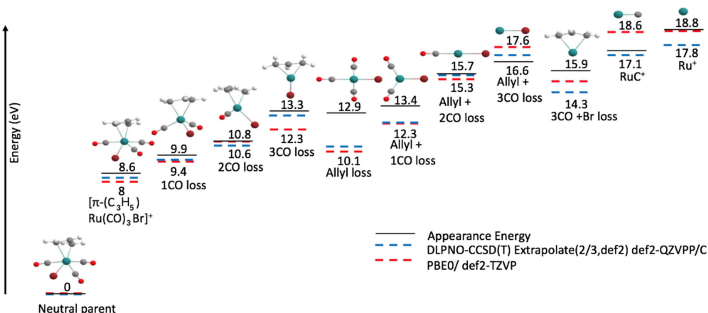
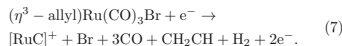


Fig. 3. Optimized structures and threshold energies for charged fragments observed in dissociative ionization of $(\eta^3\text{-allyl})\text{Ru}(\text{CO})_3\text{Br}$. Also shown are the experimentally determined AEs for the respective fragments. The structural optimization was carried out at the PBE0/def2-TZVP level of theory and the threshold energies were calculated at the PBE0/def2-TZVP and at the DLPNO-CCSD(T) Extrapolate(2/3,def2) def2-TZVP/C levels of theory. The optimized structure of the neutral molecule is shown as the origin (0 eV) of the energy axis. All numbers are in eV.

agreement is fairly good. The same is true for the threshold values for sequential CO loss, except for the coupled cluster value for the loss of 3 CO units, which is about 1 eV below the experimentally determined AE. The calculated values for the allyl loss and the allyl loss and one CO loss, on the other hand, are considerably lower than the experimental AEs for the loss of the allyl and the allyl and one CO unit. The calculated threshold value for the allyl loss and the loss of two CO units, on the other hand agrees comparably well with the experimentally determined AE. Turning back to the mass spectra shown in Figure 1 and the ion yield curves shown in Figure 2 it is clear that most of the intensity in this regression is from the loss of the allyl group and all three CO units. This may be due to a considerable kinetic shift in the allyl loss channel, making the allyl loss too slow to be observed at threshold in the current experimental setup. We note that this must be a substantial effect, as the observation window in the current setup is about 20–30 μsec and the calculated threshold values are about 2.5 eV below the experimental AE for the allyl loss. However, presuming that all observed dissociation channels are from the cationic ground state, the allyl loss would compete with the energetically much more favourable, and presumably faster CO loss. This is further supported by the fact that the $(\eta^3\text{-allyl})$ group is a polyhapto ligand with a π -facial interaction of all three allyl carbons with the central Ru atom. Another possible explanation is that the initial allyl loss proceeds from an electronically excited cationic state that is considerably higher in energy than the ground state. In both of these cases, the excess energy is readily available for further CO loss after the initial allyl loss, which provides a rationale for the bulk of the intensity for this regression representing loss of the allyl group and all three CO units. Hence, reflecting the resilience of the allyl group and the lability of the CO units toward dissociation from the complex.

The remaining fragments, m/z 130, 114 and 102, are assigned to RuCO^+ , ruthenium carbide RuC^+ and Ru^+ , respectively. For RuC^+ we find the AE to be 17.4 ± 0.4 eV and the calculated threshold value, assuming that the carbon originates from the allyl group and that H_2 is formed in the process, is 20.44 eV:



However, presuming that this fragment results from dipolar dissociation leading to bromide formation, the threshold calculated at the coupled cluster level is found to be 17.11 eV, which is in good agreement with the experimental value. Previously we have reported gas phase DEA studies to $(\eta^3\text{-allyl})\text{Ru}(\text{CO})_3\text{Br}$ [22,23], and recently Spencer et al. [24] reported a study on the electron-induced decomposition of this compound when adsorbed on surfaces at low temperature under controlled UHV conditions. In the surface study by Spencer et al. [24], attention was given to comparison of the different ligands in the context of their suitability as leaving groups in FEBID precursors. The authors found that the electron-induced fragmentation of $(\eta^3\text{-allyl})\text{Ru}(\text{CO})_3\text{Br}$ adsorbed on surfaces, is characterized by an initial CO loss. Judging from the intensity in the O (1s) signal in their XPS spectra, about 80% of the CO is lost already after an irradiation of about $4 \times 10^{16} \text{ e}^- \text{ cm}^{-2}$. Further electron irradiation of about $5 \times 10^{18} \text{ e}^- \text{ cm}^{-2}$ effectuated removal of the bulk of the bromine, but the carbon from the allyl group remained on the surface. Under gas phase single collision conditions, we find the most significant electron induced dissociation channel to be the loss of a single CO. In fact, the loss of CO ligands per incident electron in DI is about 2, while the CO loss per DEA incident is about 1 [22]. Further, other channels than

CO loss are insignificant in DEA, while both allyl and bromine loss is observed in DI of $(\eta^3\text{-allyl})\text{Ru}(\text{CO})_3\text{Br}$ in the gas phase. Thus neither the ligand loss as observed in DI in the gas phase under single collision conditions, nor that observed in DEA reflects the observations when $(\eta^3\text{-allyl})\text{Ru}(\text{CO})_3\text{Br}$ is adsorbed on surfaces and is exposed to 500 eV electrons [24]. Interestingly, in a very recent FEBID study [25] on π -allyl ruthenium(II) tricarbonyl bromide at room temperature, a reduction of the C:Ru ratio from the initial 6:1 found in the precursor to 2:1 in the deposit is observed; i.e., an average of 4 carbon atoms are lost during the deposition process. The O:Ru ratio in the deposit is similarly reduced to 0.3:1 from the initial 3:1. The authors interpret these observations as due to essentially complete CO loss, but also a partial allyl loss. They point out that the reason for the lack of allyl loss in the surface experiments may be due to the low temperature these are conducted at (-168°C). No bromine loss is observed in the FEBID experiments, which is readily understandable as the FEBID experiments are conducted under quasi steady state conditions and bromine loss is only observed in the surface experiment after prolonged irradiation of the static monolayers initially deposited. In principle both DEA and DI may be active and one would expect their efficiency to reflect the energy dependence of their relative cross sections, convoluted with the energy distribution of the secondary electrons (see e.g. Ref. [11]). However, no desorption of bromine or the allyl group is observed from the initial fragmentation of $(\eta^3\text{-allyl})\text{Ru}(\text{CO})_3\text{Br}$, when adsorbed on surfaces, and no bromine loss is observed in the FEBID experiments. This may in part be due to alteration of the dissociation efficiency when $(\eta^3\text{-allyl})\text{Ru}(\text{CO})_3\text{Br}$ is adsorbed on surfaces and/or be the result of hindered desorption of ligands through ligand-surface interaction or the compounds orientation on the surface. Furthermore, the surface may offer an efficient heat bath for vibrational cooling, quenching the presumably slower allyl loss more efficiently than the CO loss. Such ligand stabilization has been observed for clusters in general [56], but more relevant for the current study, this effect has also been observed in clusters of the FEBID precursor $\text{Fe}(\text{CO})_5$ [57]. We also note that no information on ND is provided here and this may also be a very effective channel, as has been shown in the case of $\text{Pt}(\text{PF}_3)_4$ [58].

4 Conclusion

In the current contribution we have determined threshold energies for positive ion formation from $(\eta^3\text{-allyl})\text{Ru}(\text{CO})_3\text{Br}$, computed at the PBE0/def2-TZVP and DLPNO-CCSD(T) Extrapolate(2/3,def2) def2-QZVPP/C level of theory. These were compared to the respective experimental IE and AEs estimated from the onsets of the respective electron impact ion yield curves. The computed structure of the molecular cation and the respective fragments, optimized at the PBE0/def2-TZVP level of theory, were also presented as well as the experimentally acquired ion yields for sequential CO loss and the loss of the allyl group and 1-3 CO ligands. The presented data

were discussed in the context of previous DEA studies on $(\eta^3\text{-allyl})\text{Ru}(\text{CO})_3\text{Br}$ [22,23], and in the context of a study on electron-induced decomposition of this precursor adsorbed on surfaces at low temperature under controlled UHV conditions [24], and in context to a very recent FEBID study on this compound [25]. Dissociative ionization of $(\eta^3\text{-allyl})\text{Ru}(\text{CO})_3\text{Br}$ is characterized by three progressions: sequential loss of the CO ligands, loss of the allyl group and 0-3 CO ligands and loss of the bromine and 0-3 CO ligands. Among these, the sequential CO loss has the highest integral intensity, but the loss of the allyl group and the bromine along with 3 CO units is also significant. Further fragments observed in DI of $(\eta^3\text{-allyl})\text{Ru}(\text{CO})_3\text{Br}$ are the bare ruthenium cation Ru^+ , the ruthenium carbide cation RuC^+ , and RuCO^+ . In general, the coupled cluster calculations agree better with the experimental results than the calculations using the PBE0 functional. The agreement with the experimental AEs for sequential CO loss is fairly good, considering the confidence limits on the experimental data. However, the AE for the allyl loss alone is more than 2.5 eV above the calculated values. The difference is smaller (1.0 eV) for the loss of the allyl group along with three additional CO ligands and is only 0.4 eV for the loss of the allyl group and two CO ligands (calculated at the coupled cluster level of theory). We tentatively attribute this effect to delayed dissociation of the allyl group due to the trihapto nature of the $\eta^3\text{-allyl}$ -ruthenium bond. This effect is strengthened through competition with the singly coordinated, presumably faster, direct CO loss channels. As has been discussed previously, DI of $(\eta^3\text{-allyl})\text{Ru}(\text{CO})_3\text{Br}$ leads to considerably more extensive fragmentation than DEA [22], and in contrast to DEA, DI leads to both significant allyl and bromide loss. In the previous surface study [24] the initial electron induced decomposition of $(\eta^3\text{-allyl})\text{Ru}(\text{CO})_3\text{Br}$ was found to be characterized by CO loss. Bromine loss was only observed in a second step after prolonged irradiation while loss of the allyl group was not observed. In the recent FEBID study [25] loss of all three CO ligands was observed as well as partial allyl loss, but no bromine loss was observed. The extent of the ligand loss in these experiments does not match directly with DEA or DI of this compound in the gas phase under single collision conditions, demonstrating the additional complexity introduced through surface interaction and eventual desorption barriers. Nonetheless similar to the observations in the surface experiments, CO loss is the dominating channel in both DI and DEA in the gas phase and much more efficient than the allyl loss. This further supports the assertion that polyhapto ligands are not suitable in FEBID precursors.

This work has been supported by the Icelandic Center of Research (RANNIS), Grant No. 13049305(1-3) and the University of Iceland Research Fund. M.C. acknowledges a doctoral grant from The Doctoral Grants of The University of Iceland Research Fund. It was conducted within the framework of the COST Action CM1301: Chemistry for Electron-Induced Nano-fabrication (CELINA). RMT acknowledges financial support from the COST Action CM1301: CELINA for a short term scientific mission (STSM). L.M.-W. and C.R.B. thank the US National Science Foundation (Grant CHE- 1607547) for partial support of this work.

References

1. I. Utke, P. Hoffmann, J. Melngailis, *J. Vac. Sci. Technol. B* **26**, 1197 (2008)
2. W.F. van Dorp, C.W. Hagen, *J. Appl. Phys.* **104**, 081301 (2008)
3. M. Huth, F. Porrati, C. Schwalb, M. Winhold, R. Sachser, M. Dukic, J. A. Adams, G. Fantner, *Beilstein J. Nanotechnol.* **3**, 597 (2012)
4. J. Schaefer, J. Hoelzl, *Thin Solid Films* **13**, 81 (1972)
5. A.P. Knights, P.G. Coleman, *Appl. Surf. Sci.* **85**, 43 (1995)
6. N. Silvis-Cividjian, C.W. Hagen, H.A. Leunissen, P. Kruit, *Microelectron. Eng.* **61-62**, 693 (2002)
7. S. Engmann, M. Stano, Š. Matejič, O. Ingólfsson, *Phys. Chem. Chem. Phys.* **14**, 14611 (2012)
8. S. Engmann, M. Stano, P. Papp, M.J. Brunger, Š. Matejič, O. Ingólfsson, *J. Chem. Phys.* **138**, 044305 (2013)
9. O. May, D. Kubala, M. Allan, *Phys. Chem. Chem. Phys.* **14**, 2979 (2012)
10. K. Wnorowski, M. Stano, C. Matias, S. Denif, W. Barszczewska, Š. Matejič, *Rapid Commun. Mass Spectrom.* **26**, 2093 (2012)
11. R.M. Thorman, R.K. T.P., D.H. Fairbrother, O. Ingólfsson, *Beilstein J. Nanotechnol.* **6**, 1904 (2015)
12. P.C. Hoyle, J.R.A. Cleaver, H. Ahmed, *Appl. Phys. Lett.* **64**, 1448 (1994)
13. R.K. T.P., S. Barth, R. Björnsson, O. Ingólfsson, *Eur. Phys. J. D* **70**, 163 (2016)
14. R.M. Thorman, I. Unlu, K.R. Johnson, R. Björnsson, L. McElwee-White, D.H. Fairbrother, O. Ingólfsson, *Phys. Chem. Chem. Phys.* **20**, 8 (2018)
15. J. Kopyra, P. Maciejewska, J. Maljković, *Beilstein J. Nanotechnol.* **8**, 2257 (2017)
16. M. Allan, M. Lacko, P. Papp, Š. Matejič, M. Zlatar, I.I. Fabrikant, J. Kočíšek, J. Fedor, *Phys. Chem. Chem. Phys.* **20**, 11692 (2018)
17. J.A. Spencer, Y.C. Wu, L. McElwee-White, D.H. Fairbrother, *J. Am. Chem. Soc.* **138**, 9172 (2016)
18. R.K. T.P., I. Unlu, S. Barth, O. Ingólfsson, D.H. Fairbrother, *J. Phys. Chem. C* **122** (2017)
19. W.G. Garden, H. Lu, J.A. Spencer, D.H. Fairbrother, L. McElwee-White, *MRS Commun.* **8**, 343 (2018)
20. I. Unlu, J.A. Spencer, K.R. Johnson, R.M. Thorman, O. Ingólfsson, L. McElwee-White, D.H. Fairbrother, *Phys. Chem. Chem. Phys.* **20**, 7862 (2018)
21. R.K. T.P., P. Weorlich, L. Hanefeld, R. Björnsson, H.R. Hrodmarsson, S. Barth, D.H. Fairbrother, M. Huth, O. Ingólfsson, *Beilstein J. Nanotechnol.* **9**, 555 (2018)
22. R.M. Thorman, J.A. Brannaka, L. McElwee-White, O. Ingólfsson, *Phys. Chem. Chem. Phys.* **19**, 13264 (2017)
23. R.M. Thorman, R. Björnsson, O. Ingólfsson, *Eur. Phys. J. D* **70**, 164 (2016)
24. J.A. Spencer, J. Brannaka, M. Barclay, L. McElwee-White, D.H. Fairbrother, *J. Phys. Chem. C* **119**, 15349 (2015)
25. J. Jurczyk, C.R. Brewer, O.M. Hawkins, M.N. Polyakov, C. Kapusta, L. McElwee-White, I. Utke, *ACS Appl. Mater. Interfaces* **11**, 28164 (2019)
26. J.H. Noh, M.G. Stanford, B.B. Lewis, J.D. Fowlkes, H. Plank, P.D. Rack, *Appl. Phys. A* **117**, 1705 (2014)
27. V. Scheuer, H. Koops, T. Tschudi, *Microelectron. Eng.* **5**, 423 (1986)
28. C.M. Gonzalez, W. Slingenberg, R. Timilsina, J.-H. Noh, M.G. Stanford, B.B. Lewis, K.L. Klein, T. Liang, J.D. Fowlkes, P.D. Rack, *Proc. SPIE* **9048**, 90480M (2014)
29. J.P. Perdew, K. Burke, M. Ernzerhof, *Phys. Rev. Lett.* **77**, 3865 (1996)
30. C. Adamo, V. Barone, *J. Chem. Phys.* **110**, 6158 (1999)
31. C. Riplinger, F. Neese, *J. Chem. Phys.* **138**, 034106 (2013)
32. C. Riplinger, B. Sandhoefer, A. Hansen, F. Neese, *J. Chem. Phys.* **139**, 134101 (2013)
33. C. Riplinger, P. Pinski, U. Becker, E. Valeev, F. Neese, *J. Chem. Phys.* **144**, 024109 (2016)
34. F. Neese, *WIREs Comput. Mol. Sci.* **2**, 73 (2012)
35. F. Weigend, R. Ahlrichs, *Phys. Chem. Chem. Phys.* **7**, 3297 (2005)
36. S. Grimme, J. Antony, S. Ehrlich, H. Krieg, *J. Chem. Phys.* **132**, 154104 (2010)
37. S. Grimme, S. Ehrlich, L. Goerigk, *J. Comput. Chem.* **32**, 1456 (2011)
38. A.D. Becke, *Phys. Rev. A* **38**, 3098 (1988)
39. J.P. Perdew, *Phys. Rev. B* **33**, 8822 (1986)
40. M. Bühl, H. Kabrede, *J. Chem. Theory Comput.* **2**, 1282 (2006)
41. M.P. Waller, H. Braun, N. Hojdis, M. Bühl, *J. Chem. Theory Comput.* **3**, 2234 (2007)
42. M. Bühl, C. Reimann, D.A. Pantazis, T. Bredow, F. Neese, *J. Chem. Theory Comput.* **4**, 1449 (2008)
43. M.M. Quintal, A. Karton, M.A. Iron, A.D. Boese, J.M. Martin, *J. Phys. Chem. A* **110**, 709 (2006)
44. C.A. Jiménez-Hoyos, B.G. Janesko, G.E. Scuseria, *J. Phys. Chem. A* **113**, 11742 (2009)
45. T. Weymuth, E.P.A. Cozijn, P. Chen, M. Reiher, *J. Chem. Theory Comput.* **10**, 3092 (2014)
46. A. Hellweg, C. Hattig, S. Hofener, W. Klopper, *Theor. Chem. Acc.* **117**, 587 (2007)
47. F. Neese, *J. Am. Chem. Soc.* **128**, 10213 (2006)
48. E.H. Bjarnason, B. Ómarsson, S. Engmann, F.H. Ómarsson, O. Ingólfsson, *Eur. Phys. J. D* **68**, 121 (2014)
49. R.C. Wetzel, F.A. Baiocchi, T.R. Hayes, R.S. Freund, *Phys. Rev. A* **35**, 559 (1987)
50. G.H. Wannier, *Phys. Rev.* **90**, 817 (1953)
51. K.R. Johnson, A.P. Rodriguez, C.R. Brewer, J.A. Brannaka, Z. Shi, J. Yang, B. Salazar, L. McElwee-White, A.V. Walker, *J. Chem. Phys.* **146**, 052816 (2017)
52. G. Sbrana, G. Braca, F. Piacenti, P. Pino, *J. Organomet. Chem.* **13**, 240 (1968)
53. G.A. Junk, H.J. Svec, *Z. Naturforsch. B* **23**, 1 (1968)
54. M.I. Bruce, *Adv. Organomet. Chem.* **6**, 273 (1968)
55. R.B. King, *J. Am. Chem. Soc.* **90**, 1417 (1968)
56. O. Ingólfsson, F. Weik, E. Illenberger, *Int. J. Mass Spectrom. Ion Processes* **155**, 1 (1996)
57. J. Lengyel, J. Fedor, M. Fárnik, *J. Phys. Chem. C* **120**, 17810 (2016)
58. M. Zlatar, M. Allan, J. Fedor, *J. Phys. Chem. C* **120**, 10667 (2016)

Article II

The Role of Low-Energy Electron Interactions in cis-Pt(CO)₂Br₂ Fragmentation

Maicol Cipriani, Styrmir Svavarsson, Filipe Ferreira da Silva, Hang Lu, Lisa McElwee-White and Oddur Ingólfsson

International Journal of Molecular Sciences, 2021,22(16), 89984

This is an open access article distributed under the Creative Commons Attribution License CC BY 4.0

Maicol Cipriani conducted all the computational work and a major part of the data analysis. He wrote the first of the manuscript and contributed to editing until publication.



Article

The Role of Low-Energy Electron Interactions in cis-Pt(CO)₂Br₂ Fragmentation

Maicol Cipriani ¹, Styrmir Svavarsson ¹, Filipe Ferreira da Silva ², Hang Lu ³, Lisa McElwee-White ³ 
and Oddur Ingólfsson ^{1,*}¹ Department of Chemistry and Science Institute, University of Iceland, Dunhagi 3, 107 Reykjavik, Iceland; mac31@hi.is (M.C.); styrmir94@gmail.com (S.S.)² CEFITEC, Departamento de Física, Faculdade de Ciências e Tecnologia, Universidade NOVA de Lisboa, 2829-516 Caparica, Portugal; fr.silva@fct.unl.pt³ Department of Chemistry, University of Florida, Gainesville, FL 32611-7200, USA; hlu90@ufl.edu (H.L.); lmwhite@chem.ufl.edu (L.M.-W.)

* Correspondence: odduring@hi.is



Citation: Cipriani, M.; Svavarsson, S.; Ferreira da Silva, F.; Lu, H.; McElwee-White, L.; Ingólfsson, O. The Role of Low-Energy Electron Interactions in cis-Pt(CO)₂Br₂ Fragmentation. *Int. J. Mol. Sci.* **2021**, *22*, 8984. <https://doi.org/10.3390/ijms22168984>

Academic Editor: Mauro Coluccia

Received: 26 July 2021

Accepted: 16 August 2021

Published: 20 August 2021

Publisher's Note: MDPI stays neutral with regard to jurisdictional claims in published maps and institutional affiliations.



Copyright: © 2021 by the authors. Licensee MDPI, Basel, Switzerland. This article is an open access article distributed under the terms and conditions of the Creative Commons Attribution (CC BY) license (<https://creativecommons.org/licenses/by/4.0/>).

Abstract: Platinum coordination complexes have found wide applications as chemotherapeutic anticancer drugs in synchronous combination with radiation (chemoradiation) as well as precursors in focused electron beam induced deposition (FEBID) for nano-scale fabrication. In both applications, low-energy electrons (LEE) play an important role with regard to the fragmentation pathways. In the former case, the high-energy radiation applied creates an abundance of reactive photo- and secondary electrons that determine the reaction paths of the respective radiation sensitizers. In the latter case, low-energy secondary electrons determine the deposition chemistry. In this contribution, we present a combined experimental and theoretical study on the role of LEE interactions in the fragmentation of the Pt(II) coordination compound cis-PtBr₂(CO)₂. We discuss our results in conjunction with the widely used cancer therapeutic Pt(II) coordination compound cis-Pt(NH₃)₂Cl₂ (cisplatin) and the carbonyl analog Pt(CO)₂Cl₂, and we show that efficient CO loss through dissociative electron attachment dominates the reactivity of these carbonyl complexes with low-energy electrons, while halogen loss through DEA dominates the reactivity of cis-Pt(NH₃)₂Cl₂.

Keywords: anticancer drugs; cisplatin; platinum (II) halo-carbonyl complexes; low-energy electrons; dissociative electron attachment; dissociative ionization; focused electron beam induced deposition

1. Introduction

Platinum coordination complexes, such as cisplatin [Pt(NH₃)₂Cl₂], have been widely used as chemotherapeutic anticancer drugs since the 1970s [1,2]. Cisplatin-based chemotherapy has proven to be highly effective against testicular cancer [3,4] and other various types of malignancies, such as metastatic melanoma, carcinoma of the head and neck and metastatic breast cancer [5]. The cytotoxicity of this platinum complex lies in its ability to form CDDP–DNA adducts inhibiting replication [1,2]. In fact, after entering the cell, the cisplatin undergoes hydrolysis, and as a result, the two chlorine atoms are lost. The remaining fragment forms the CDDP–DNA adducts by binding to guanine or purine nucleobases that inhibit transcriptions of the cancer cell, blocking its replication. The synchronous combination of platinum complexes and radiation (chemoradiation) has increased the survival probability of cancer patients due to the enhancement of the cell-killing effect of radiation [6–8]. It has been hypothesized that cisplatin, in addition to acting directly as a chemotherapeutic agent, also acts as a radiosensitizer. Apart from the medical/biological applications, platinum-based complexes are also used as precursors for focused electron beam-induced deposition (FEBID) [9–13], an electron-induced materials deposition technique for the fabrication of functional nanostructures [14]. In both applications, low-energy electrons (LEEs) play an important role in dictating the fragmentation pathways through

electron capture as well as by electron ionization. In chemoradiation, these low-energy electrons are produced in the interaction of the ionizing radiation with the tissue material and in FEBID by interaction of the high energy electron beam with the substrate surface and the depositing material [15,16]. In both cases, the energy distribution of these secondary electrons peaks at or below 10 eV, and has a contribution close to 0 eV and a long tail extending to higher energies [17]. These LEEs can inflict considerable damage on the DNA [18], causing single and double strand breaks (SSB and DSB) [19]. In a 2008 study by Zheng et al. [7], the authors showed that when cisplatin is covalently bonded to DNA, SSB and DSB induced by LEEs are substantially enhanced. This enhancement has been attributed to bond cleavage triggered by the formation of transient negative ions (TNI) through electron capture, i.e., dissociative electron attachment (DEA). Dissociative electron attachment studies on cisplatin have been performed by Kopyra et al. [20], determining the fragmentation pathways under interaction with low-energy electrons. In this study, it was shown that electrons close to 0 eV can easily fragment this molecule by cleavage of the Pt–Cl bonds, leading to the loss of one or even both Cl atoms with considerable intensity. Hence, one single low-energy electron efficiently triggers the cleavage of both the Pt–Cl bonds. In the FEBID process, gas phase precursors, usually organometallics, are introduced into a high vacuum (HV) chamber in close proximity to a substrate surface where they are subjected to a tightly focused high-energy electron-beam. The high energy electron beam generates a considerable number of low-energy SEs [21,22] that interact with the precursor molecules, initiating chemical reactions through DEA, dissociative ionization (DI), neutral dissociation (ND) and dipolar dissociation (DD). These processes determine the decomposition of the precursor molecule at the substrate surface leading to deposition of the nonvolatile fragments formed, while volatile fragments are pumped away. A description of these processes is given, e.g., in References [23,24]. Ideally, for the creation of metallic deposits, the organometallic precursors should fully dissociate, leaving the metallic atom on the surface while the ligands are pumped away. In recent years, several studies on LEE interactions with organometallic platinum compounds have been carried out in the context of FEBID [25–28], studies that are also relevant to the action of radiation sensitizers where low-energy electrons are expected to play a significant role.

In low-energy electron interactions with $\text{Pt}(\text{CO})_2\text{Cl}_2$ in the gas phase under single collision conditions, Ferreira da Silva et al. [28] found that, in contrast to cisplatin [20], DEA close to 0 eV electron incident energies leads exclusively to CO loss. This channel is very efficient for both single and double CO loss, while Cl loss is inefficient and only observed at higher energies. Similarly, CO loss is also the main channel in dissociative ionization of this compound, though significant Cl loss is also observed and the bare Pt^+ ion is formed with appreciable intensity. In a UHV surface study where adsorbed monolayers of $\text{Pt}(\text{CO})_2\text{Cl}_2$ (and $\text{Pt}(\text{CO})_2\text{Br}_2$) were exposed to 500 eV electrons from a flood gun (and correspondingly the generated low-energy SEs), J. A. Spencer et al. [12] found that these compounds decomposed by rapid CO loss leading to a PtCl_2 deposit with the 1:2 stoichiometric ratio of the initial compound. Prolonged electron irradiation then led to nearly quantitative removal of the chlorine. The authors attributed this to an initial DEA step leading to the CO loss. In this context, a comparative electron beam deposition study of $\text{Pt}(\text{CO})_2\text{Cl}_2$ and $\text{Pt}(\text{CO})_2\text{Br}_2$ was recently conducted by A. Mahgoub et al. [29]. Interestingly, it was found that while both these compounds behave similarly, the UHV deposits contained a significant portion of the halogen species but little or no carbon, while the deposits created under HV contained only small amounts of halogen species but high carbon content. It is possible that the presence of trace water in the HV experiments leads to the formation of volatile HCl in the irradiation process, decreasing the chlorine content in the deposits. This has been observed by M. Rohdenburg et al. [13,30] for cisplatin in electron-induced intermolecular reactions of the chlorine with hydrogen from the amine ligand and in electron-induced reactions of $(\eta^3\text{-C}_3\text{H}_5)$ $\text{Ru}(\text{CO})_3\text{Cl}$ in the presence of NH_3 as processing gas. It is thus clear that the environment plays a critical role in electron-induced

decomposition of these compounds, and this is especially true for biological media where water is plentiful.

In the current study, we have performed DEA and DI experiments on $\text{Pt}(\text{CO})_2\text{Br}_2$ in the gas phase under single collision conditions as well as thermochemical calculations at the DFT and coupled-cluster level of theory for the respective processes. Relaxed potential energy surface scans were computed, and vertical electron attachment energies and the respective MOs were calculated along with the respective electronic excitation energies. For comparison, the vertical transition energies from the anionic ground state to the first excited anionic state are also presented for all the Pt(II) halogen carbonyls; $\text{Pt}(\text{CO})_2\text{X}$ (X = F, Cl, Br and I). We compare our findings with previous work on electron-induced decomposition of $\text{Pt}(\text{CO})_2\text{Cl}_2$ and of $\text{Pt}(\text{CO})_2\text{Br}_2$ as well as cisplatin; $\text{Pt}(\text{NH}_3)_2\text{Cl}_2$.

2. Results and Discussion

Figure 1 shows the DEA ion yield curves for $\text{Pt}(\text{CO})\text{Br}_2^-$ and PtBr_2^- , from $\text{Pt}(\text{CO})_2\text{Br}_2$, i.e., the energy dependence of the loss of one and two CO ligands, respectively. To better allow comparison, the intensities are normalized with respect to the pressure and the intensity of SF_6^- formation from SF_6 at 0 eV recorded before each measurement. These are the two most efficient DEA processes and both fragments are formed with appreciable intensity close to 0 eV. However, while $[\text{Pt}(\text{CO})\text{Br}_2]^-$ peaks at 0 eV, the maximum of the low-energy PtBr_2^- contribution is at about 0.07 eV, and both contributions are broad and asymmetric towards higher energies. The loss of both CO ligands, and the formation of PtBr_2^- , is also observed through a higher-lying resonance (or resonances), contributing to the ion yield close to 3 eV. This contribution is not observed in the single CO loss ion yield curve. This is similar to the previous observations for $\text{Pt}(\text{CO})_2\text{Cl}_2$ [28], where DEA contributions through higher lying resonances were observed in the $[\text{PtCl}_2]^-$ but not in the $[\text{Pt}(\text{CO})\text{Cl}_2]^-$ ion yield curves. The single CO loss from $\text{Pt}(\text{CO})_2\text{Cl}_2$ was found to be exothermic, and it was suggested that the excess energy in the $[\text{Pt}(\text{CO})\text{Cl}_2]^-$ fragment (i.e., after the first CO loss) makes its survival probability low at the onset of the high energy resonance (or resonances), and further decomposition to $[\text{PtCl}_2]^-$ is the predominant process. The losses of one and two CO ligands from $\text{Pt}(\text{CO})_2\text{Br}_2$ through DEA are also found to be exothermic, and at the DLPNO-CCSD(T) level of theory, we find the threshold for the loss of one and two CO ligands to be -1.57 and -0.48 eV, respectively.

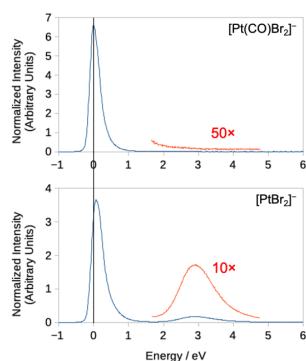


Figure 1. Negative ion yields for the loss of one and two CO ligands. **Top:** loss of one CO ligand; **bottom:** loss of two CO ligands.

This is also clear from the cut through the relative potential energy surfaces (PESs) shown in Figure 2. These are calculated through relaxed energy scans at the wB97X-D3/ma-def2-TZVP level of theory along the OC–Pt(CO)Br₂ and OC–PtBr₂ dissociation coordinates, respectively. For [Pt(CO)Br₂][−], the energy contribution of the CO ligand (ϵ_{CO}) is included in the calculations. The single-point energies obtained from the relaxed energy scans were fitted with Morse potential energy function. From the fitting, we obtained the Pt–CO dissociation energies for the neutral molecule (Pt(CO)₂Br₂), the molecular anion ([Pt(CO)₂Br₂][−]), and the [Pt(CO)Br₂][−] fragment. It is noted that these PESs do not include the zero-point vibrational energy (ZPVE). For the neutral molecule, we derived a dissociation energy of 1.5 eV and an equilibrium Pt–CO bond length of 1.9 Å. For the molecular anion, these values were found to be 0.2 eV and 1.9 Å, respectively. The Pt–CO bond length in [Pt(CO)Br₂][−] was found to be 1.8 Å and the dissociation energy was found to be 1.4 eV. The corresponding Pt–CO bond lengths from our geometry optimization at the wB97X-D3/ma-def2-TZVP level of theory are 1.9 Å for Pt(CO)₂Br₂, [Pt(CO)₂Br₂][−] and [Pt(CO)Br₂][−], which agrees with these derived from the PES fits.

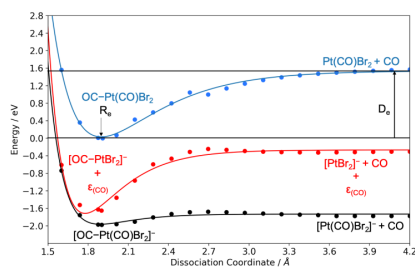


Figure 2. Relaxed potential energy surface scans for OC–Pt(CO)Br₂ dissociation from the neutral parent and OC–Pt(CO)Br₂ and OC–PtBr₂ dissociations from the respective anion. The calculations were performed at wB97X-D3/ma-def2-TZVP level of theory.

As is clear from Figure 2, the PESs for the formation of the anionic fragment [Pt(CO)Br₂][−] and [PtBr₂][−] lie entirely below the ground state of the neutral molecule in the range of the dissociative coordinate 1.4 to 4.2 Å. Thus, the survival probability of [Pt(CO)Br₂][−], with respect to further CO loss, drops rapidly above the threshold. This, in turn, is reflected in the shift and broadening of the low-energy contribution for [Pt(CO)Br₂][−] as compared to PtBr₂[−] and the lack of any [Pt(CO)Br₂][−] contribution through the higher lying resonance at around 3 eV.

Similar to Pt(CO)₂Cl₂ [28], we attribute the low-energy contributions in the Pt(CO)₂Br₂ ion yields to the initial formation of the ground state negative ion and the first excited negative ion state, i.e., electron occupation of the LUMO and the slightly higher lying LUMO+1. Figure 3 shows the electrostatic potential isosurfaces for the corresponding SOMO and SOMO+1. The former of these is a mixture of contributions from the π^* CO orbitals and the Pt 5 d_{xz} p and has antibonding character. The latter is predominantly composed of the Pt $d_{x^2-y^2}$ orbital with σ^* P–L antibonding character (L = CO or Br) and direct CO loss from this excited anion state is given by its repulsive σ^* nature. The same process from the ground anion state, however, is in principle symmetry forbidden and requires effective coupling of the CO π^* orbital with the respective σ^* Pt–L. For Pt(CO)₂Cl₂ [28], it has been hypothesized that such effective coupling is provided by the out-of-plane bending of the CO group.

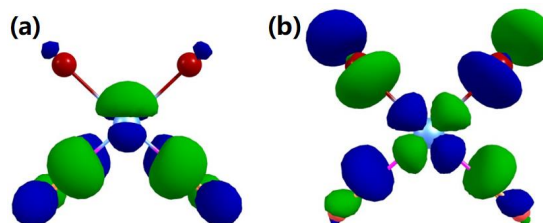


Figure 3. Isosurfaces of the frontier orbitals of the $\text{Pt}(\text{CO})_2\text{Br}_2$ anion obtained with a contour value of 0.05. (a): SOMO. (b): SOMO+1.

From our calculation, we derive a dipole moment for $\text{Pt}(\text{CO})_2\text{Br}_2$ of 5.0 D, which should be well above the limit for a capture into a dipole bound state [31]. For the lower lying (0 eV) resonance, we anticipate that this provides a gateway for the DEA process as has been discussed by, e.g., Sommerfeld for nitromethane, uracil and cyanoacetylene [32]. In this mechanism, the initially formed diffuse dipole-bound state couples with the nuclear motion, channeling the excess energy into the vibrational degrees of freedom. The so formed vibrational Feshbach resonance couples with the respective valence state, in this case the LUMO, leading to a transient negative ion characterized by the excess electron defining the SOMO. At higher energies, where the angular momentum of the electron has l components higher than zero, the initial capture may rather be through the formation of the respective shape resonance. A detailed discussion on the actual capture mechanism at these low incident energies exceeds the scope of this paper, but we refer the interested reader to Reference [24] and references therein.

The calculated adiabatic electron affinity of $\text{Pt}(\text{CO})_2\text{Br}_2$ was found to be 2.31 eV at the $\omega\text{B97X-D3}$ level of theory and 2.11 eV at the $\text{DLPNO-CCSD(T)/aug-cc-pVQZ}$ level of theory. The vertical attachment energy (VAE) for the anion ground state was found to be -1.14 eV at the $\omega\text{B97X-D3}$ level of theory and -0.99 eV for the first excited anion state using a delta-SCF approach at the same level of theory. Similar to $\text{PtCl}_2(\text{CO})_2$, the VAEs associated with formation of the ground state and first excited state anions are both negative at the equilibrium geometry of the neutral molecule. The resulting vertical excitation energy for $\text{PtBr}_2(\text{CO})_2$ from the anion ground state to the first anionic excited state was found to be 0.15 eV, while for $\text{PtCl}_2(\text{CO})_2$, the value was found to be 0.38 eV with delta-SCF at the same level of theory [28]. This reflects the increased destabilization of the σ^* SOMO+1 with increasing electronegativity of the halogen ligand and suggests that substitution of the Br ligands with I atoms would further decrease the excitation energy while substitution with F atoms would largely increase the excitation energy. This is confirmed by the vertical transition energies between these anion states, obtained at TDDFT wB97X-D3/ma-def2-TZVP level of theory, shown in Table 1. As can be seen in Table 1, the vertical excitation energy from the anionic ground state to the first anionic excited state decreases following the trend $[\text{Pt}(\text{CO})_2\text{F}_2]^- > [\text{Pt}(\text{CO})_2\text{Cl}_2]^- > [\text{Pt}(\text{CO})_2\text{Br}_2]^- > [\text{Pt}(\text{CO})_2\text{I}_2]^-$.

Table 1. Calculated vertical excitation energy from the anionic ground state to the first anionic excited at the TDDFT wB97X-D3/ma-def2-TZVP level of theory.

Anions	Vertical Excitation SOMO+1 \leftarrow SOMO (eV)
$[\text{Pt}(\text{CO})_2\text{F}_2]^-$	0.58
$[\text{Pt}(\text{CO})_2\text{Cl}_2]^-$	0.44
$[\text{Pt}(\text{CO})_2\text{Br}_2]^-$	0.27
$[\text{Pt}(\text{CO})_2\text{I}_2]^-$	0.13

This is also reflected in the more structured low-energy contributions from $\text{Pt}(\text{CO})_2\text{Cl}_2$ as compared to the high energy tail observed in $\text{Pt}(\text{CO})_2\text{Br}_2$. To visualize this, Figure 4 shows a fit of two Gaussian functions to the low-energy contributions in the ion yield curves for $[\text{Pt}(\text{CO})\text{Br}_2]^-$ and PtBr_2^- . An excellent fit with an R^2 value of 0.99 is achieved with a fairly narrow lower energy contribution peaking at about 0 eV electron energy and a broader higher energy component peaking at 0.18 and 0.33 eV, respectively. These values for the higher energy contributions are in both cases slightly below the corresponding VAE as is to be expected due to the intrinsic competition between autodetachment and dissociation. The lower value for $[\text{Pt}(\text{CO})\text{Br}_2]^-$ as compared to $[\text{PtBr}_2]^-$ is also in line with the expected energy dependence of the survival probability of that fragment with respect to further CO loss to form $[\text{PtBr}_2]^-$.

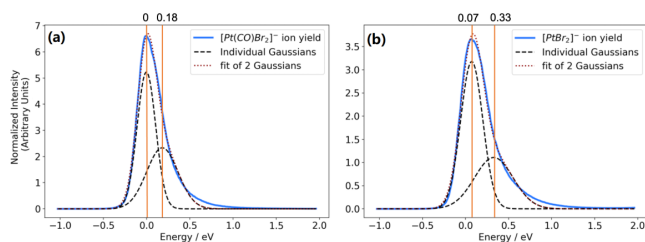


Figure 4. Fit of two Gaussian functions to the $[\text{Pt}(\text{CO})\text{Br}_2]^-$ ion yield (a) and the $[\text{PtBr}_2]^-$ ion yield (b). The first represents contributions from dissociation from the anionic ground state, while the latter represents these from the first excited anionic state.

In addition to the CO loss fragments, DEA to $\text{Pt}(\text{CO})_2\text{Br}_2$ also leads to the formation of $[\text{Pt}(\text{CO})\text{Br}]^-$, $[\text{PtBr}]^-$ and Br^- , though with considerably lower intensity. The ion yield traces for these are shown in Figure 5, and Table 2 lists the threshold values for all fragments observed from $\text{Pt}(\text{CO})_2\text{Br}_2$, calculated at the wB97X-D3/ma-def2-TZVP and DLPNO-CCSD(T)/aug-cc-pVQZ level of theory. For comparison, the onsets of individual contributions estimated from the ion yield curves, i.e., the appearance energies (AEs), are also shown in Table 2. With the exception of the formation of $[\text{PtBr}]^-$, all DEA channels observed from $\text{Pt}(\text{CO})_2\text{Br}_2$ are found to be exothermic. Similar to $[\text{PtBr}_2]^-$, the ion yield curve for $[\text{Pt}(\text{CO})\text{Br}]^-$ shows two contributions, one that peaks close to 0.5 eV and one with considerably higher intensity peaking close to 3 eV. We attribute the former of these to dissociation from the first excited anionic state, though contributions from the high energy tail from the ground state transient negative ion (TNI) cannot be excluded. The 3 eV contribution is shifted to slightly higher energies as compared to the double CO loss, which is likely rooted in the competition between these channels falling in favor of the more exothermic double CO loss at lower energies. The situation is very similar for the Br^- formation, which also appears through two contributions peaking at around 0.15 and 3.4 eV, respectively, and here we also attribute the low-energy contribution to the σ^* , first anionic excited state. Interestingly we do not observe any $[\text{Pt}(\text{CO})_2\text{Br}]^-$ contributions in DEA to $\text{Pt}(\text{CO})_2\text{Br}_2$, suggesting that $[\text{Pt}(\text{CO})\text{Br}]^-$ is formed through initial CO loss, i.e., through Br loss from $[\text{Pt}(\text{CO})\text{Br}_2]^-$. This may be rooted in the synergistic back-bonding Br–Pt–CO interaction through the contribution of Br lone pair electron density through the metal d orbitals into the $\pi^*(\text{CO})$. If the CO is lost first, then the partial extra bond from Br–Pt is gone, and the Br that was trans to the now missing CO may be more disposed to dissociation.

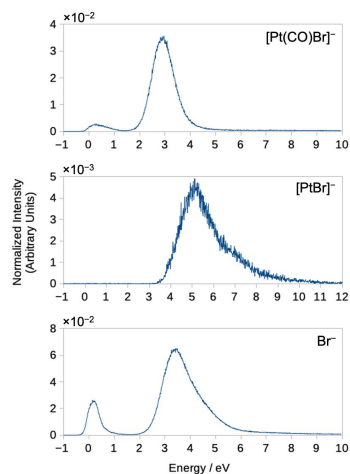


Figure 5. Negative ion yields for $[\text{Pt}(\text{CO})\text{Br}]^-$, $[\text{PtBr}]^-$ and Br^- .

Table 2. Appearance energies and calculated thermochemical thresholds for all observed DEA fragments calculated at the wB97X-D3/ma-def2-TZVP and DLPNO-CCSD(T)/aug-cc-pVQZ level of theory. Threshold energies include the thermal energy of the neutral at 50 °C.

Fragments	AEs (eV)	Threshold Energy	
		wB97X-D3/ma-def2-TZVP (eV)	DLPNO-CCSD(T)/aug-cc-pVQZ (eV)
$[\text{Pt}(\text{CO})\text{Br}_2]^-$	0.0	−2.06	−1.57
$[\text{Pt}(\text{CO})\text{Br}]^-$	0.0–2.0	−0.20	−0.017
$[\text{PtBr}_2]^-$	0.0	−0.70	−0.48
$[\text{PtBr}]^-$	3.8	3.56	3.80
$[\text{Br}]^-$	0.0–2.3	−0.93	−0.59

Finally, $[\text{PtBr}]^-$ is formed with an onset close to its threshold at 3.8 eV and a maximum at about 5 eV. This fragment, which is formed through the loss of three ligands, appears with low intensity, and we anticipate that it is formed through the high energy tail of the resonance (or resonances), contributing to the $[\text{PtBr}_2]^-$, $[\text{Pt}(\text{CO})\text{Br}]^-$ and Br^- formation at around 3 eV.

At the wB97X-D3/ma-def2-TZVP level of theory, taking into account the ZPVE and the thermal energy corrections at room temperature, we find the halogen–Pt bond energies for $\text{Pt}(\text{CO})_2\text{Cl}_2$ and $\text{Pt}(\text{CO})_2\text{Br}_2$ to be 3.3 and 2.8 eV, respectively. The calculated threshold for the formation of $[\text{Pt}(\text{CO})\text{Br}]^-$ was found to be −0.017 eV at the DLPNO-CCSD(T) level of theory, while the threshold for $[\text{Pt}(\text{CO})\text{Cl}]^-$ was found to be 0.19 eV at the same level of theory. Similarly, the calculated threshold for the formation of Br^- was found to be −0.59 eV at the DLPNO-CCSD(T) level of theory, while the calculated threshold for Cl^- formation from $\text{Pt}(\text{CO})_2\text{Cl}_2$ was found to be −0.51 eV at the same level of theory. It is noted

that the $[\text{Pt}(\text{CO})\text{Br}]^-$ calculations include the thermal energy of the neutral at 50 °C, while those for $\text{Pt}(\text{CO})_2\text{Cl}_2$ include the thermal energy of the neutral at 85 °C.

As compared to $\text{Pt}(\text{CO})_2\text{Cl}_2$ and $\text{Pt}(\text{CO})_2\text{Br}_2$, DEA to cisplatin $[\text{Pt}(\text{NH}_3)_2\text{Cl}_2]$ shows a very different behavior. Here, the dominant DEA channels are the formation of $[\text{Pt}(\text{NH}_3)_2\text{Cl}]^-$, Cl^- and $[\text{Pt}(\text{NH}_3)_2]^-$ [20], i.e., the cleavage of the Pt–halogen bonds. This is interesting, as similar to the Pt–CO bond, the Pt– NH_3 bond is much weaker than the Pt–Cl bond, and in their study, Kopyra et al. [20] calculated the respective bond energies to be 1.5 eV for the Pt– NH_3 bond and 3.3 eV for the Pt–Cl bond using DFT. The LUMO, involved in LEE attachment to cisplatin, however, has a repulsive σ^* character in all the ligands [20], which is more similar to the LUMO+1 of the current compound, through which effective Pt–Br bond cleavage is observed. Thus, at very low energies, where the electron attachment cross sections are the highest, direct relaxation of $[\text{Pt}(\text{NH}_3)_2\text{Cl}_2]^-$ by lengthening of the Pt–Cl bond beyond its bonding distance is allowed while this process is in principle symmetry forbidden from the π^*_{CO} character LUMO of $[\text{Pt}(\text{CO})_2\text{Cl}]^-$ and $[\text{Pt}(\text{CO})_2\text{Br}]^-$.

Dissociative ionization of $\text{Pt}(\text{CO})_2\text{Br}_2$ leads to much more extensive fragmentation than DEA. Figure 6 shows the positive ion DI spectrum of $\text{Pt}(\text{CO})_2\text{Br}_2$ recorded at 70 eV electron energy, and Table 3 lists the relative contributions of individual fragments normalized to the contribution of the parent ion as well as the efficiency of CO and Br removal per incident electron. The DI spectrum shows all the fragments associated with the breakdown of the $\text{Pt}(\text{CO})_2\text{Br}_2$. As for $\text{Pt}(\text{CO})_2\text{Cl}_2$, the dominant contribution is from the parent ion $[\text{Pt}(\text{CO})_2\text{Br}_2]^+$, and the bare Pt^+ ion is observed with significant intensity. The loss of one and two CO, i.e., the formation of $[\text{Pt}(\text{CO})\text{Br}_2]^+$ and $[\text{PtBr}_2]^+$, is also appreciable, while the loss of one Br and two Br, i.e., $[\text{Pt}(\text{CO})_2\text{Br}]^+$ and $[\text{Pt}(\text{CO})_2]^+$, is much less significant. The formation of $[\text{PtBr}]^+$ is appreciable, while other fragments appear with marginal intensity.

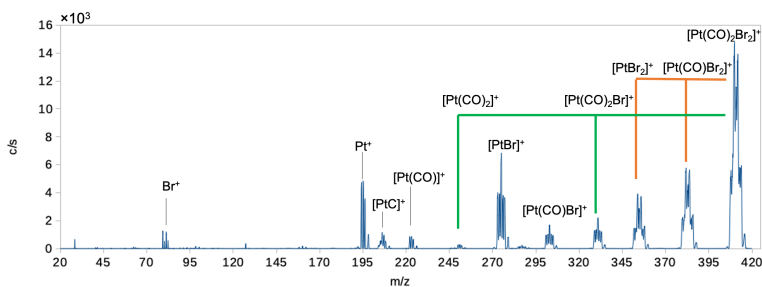


Figure 6. Positive ion mass spectrum of $\text{Pt}(\text{CO})_2\text{Br}_2$ recorded at 70 eV incident electron energy. Green lines show the sequential loss of the two Br ligands, while orange lines show the sequential loss of the two CO ligands.

Finally, for comparison with the electron-induced decomposition of $\text{Pt}(\text{CO})_2\text{Br}_2$ in FEBID and at surfaces, we have calculated the average bromine and carbonyl loss per incident in DEA and DI (see Table 3). The average CO loss per incident in DEA was calculated by taking the integral intensities of all ion yield curves of CO-loss fragments from about 0 to 10 eV (see Figure 1) and weighing these by the number of carbonyls lost. In a similar way, the average Br loss through DEA was obtained by weighing the integral intensities of the $[\text{Pt}(\text{CO})\text{Br}]^-$, $[\text{PtBr}]^-$ and Br^- ion yield curves by the number of bromines lost. For DI, the average CO and Br losses per incident were obtained in a similar way by integrating over the isotope distribution of the respective fragment peaks in the positive ion mass spectrum and weighing these by the number of CO and Br lost in the respective processes. In DEA we found an average CO loss of 1.4 per incident through DEA, and

an average Br loss per incident of only 0.04. For DI, we found an average CO loss of 0.7 per incident and an average Br loss of 0.3. This is comparable to the observations made for Pt(CO)₂Cl₂ [28], where the average CO loss in DEA is also found to be 1.4 and the Br loss negligible, while DI leads to an average of 0.6 CO and 0.5 Br lost per incident, respectively. In electron-induced decomposition of Pt(CO)₂Cl₂ at surfaces [12], CO loss was found to be the dominating process at low electron doses, leading to an average CO loss of around 1–2. Similarly, in UHV electron-induced deposition experiments, the deposits made with Pt(CO)₂Br₂ and Pt(CO)₂Cl₂ were found to retain the nearly 1:2 platinum:halogen ratio of the precursor compounds [29]. These surface and deposition studies suggest that DEA rather than DI is dominating in the initial decomposition step. However, as mentioned in the introduction, depositions made with Pt(CO)₂Cl₂ and Pt(CO)₂Br₂ under HV conditions were found to contain very little of the respective halogen species with carbon being the main contaminant [29].

Table 3. Relative yields of the fragments formed by DI and DEA to Pt(CO)₂Br₂, average weighted CO loss per DEA and DI incident and average weighted Br loss per DI incident.

Fragments	Relative DI Contributions	Relative DEA Contributions
[Pt(CO) ₂ Br ₂] ⁺	1	-
[Pt(CO)Br ₂] ^{+/-}	0.38	1
[PtBr ₂] ^{+/-}	0.23	0.76
[Pt(CO) ₂ Br] ⁺	0.10	-
[Pt(CO)Br] ^{+/-}	0.07	0.02
[PtBr] ^{+/-}	0.25	0.004
[Pt(CO) ₂] ⁺	0.01	-
[Pt(CO)] ⁺	0.02	-
[PtC] ⁺	0.04	-
Pt ⁺	0.11	-
Br ^{+/-}	0.01	0.05
Average CO loss	0.7	1.4
Average Br loss	0.3	0.04

For electron irradiation of cisplatin at surfaces [13], it has been shown that intermolecular reactions of the chlorine with hydrogen from the amino ligands readily produce HCl that desorbs and effectively reduces the Cl content in the adsorbate. Similarly, the use of NH₃ as a processing gas in electron-induced decomposition of (η³-C₃H₅)Ru(CO)₃Cl at surfaces has proven effective in Cl removal through HCl formation [30]. We speculate that residual water may have the same effect in FEBID of Pt(CO)₂Cl₂ and Pt(CO)₂Br₂ under HV conditions and thus explain the very different observations under HV and UHV conditions. This is important when considering electron-induced decomposition in a biological environment, where water is omnipresent.

3. Materials and Methods

3.1. Experimental Setup

Low-energy electron interactions with Pt(CO)₂Br₂ were studied in a crossed electron-molecule beam apparatus. The experimental setup has been covered previously [33], and only a short description will be given here. The instrument consists of a quadrupole mass spectrometer (HIDEN EPIC1000), a trochoidal electron monochromator (TEM) and an effusive gas inlet system. The TEM and the ion extraction elements are maintained at 120 °C during measurements to avoid target gas condensation on the electrical lens components. A quasi mono-energetic electron beam, generated with the TEM, crosses an effused molecular beam of the target gas. The ions formed in the crossed beam region are then extracted from the reaction region by a weak electric field (<1 V/cm) and analyzed by the mass spectrometer. Both positive and negative ions can be studied, and ion yield

curves are recorded by scanning through the electron energy at a fixed mass (m/z), while mass spectra are recorded by scanning through the relevant m/z range at fixed energies.

The background pressure inside the chamber is on the order of 10^{-6} Pa and the pressure during measurements typically about 10^{-5} Pa to ensure single collision conditions. The energy scale was calibrated by the well documented SF_6^- formation from SF_6 at 0 eV [34] recorded before and after each measurement. The energy resolution was estimated from the FWHM of that signal and was found to be 100–150 meV for the current measurements. $\text{PtBr}_2(\text{CO})_2$ is solid at room temperature and was sublimed at $\sim 50^\circ\text{C}$ in the gas inlet system.

3.2. $\text{PtBr}_2(\text{CO})_2$ Synthesis

$\text{PtBr}_2(\text{CO})_2$ was synthesized at the University of Florida as previously reported [29] and characterized by comparison to literature data [35].

3.3. Computational Method

Ab initio calculations were performed with the quantum chemistry package ORCA 4.2.1 [36]. All geometries were first optimized using a range-separated hybrid functional $\omega\text{B97X-D3}$ [37,38] with minimal augmented triple zeta basis set, ma-def2-TZVP [39,40] and the def2 effective core potential (ECP) [41] for platinum core electrons. Harmonic vibrational frequencies of the molecule and fragments were calculated at the same level of theory. They were confirmed to be positive, i.e., all structures were stationary points on the potential energy surface, and were used to yield zero-point energy contributions for the molecule and all the fragments as well as thermal energy correction for the neutral parent at 50 °C. Final threshold energies were calculated using the coupled cluster approach at the DLPNO-CCSD(T) [42–45] level of theory on the $\omega\text{B97X-D3}$ optimized geometries. A large and diffuse aug-cc-pVQZ basis set [46–48] (aug-cc-pVQZ-PP basis set and associated pseudopotential for Pt) [49] was used. All thresholds include zero-point vibrational energies for all fragments and the thermal energy of the neutral molecule at 50 °C ($\omega\text{B97X-D3}/\text{ma-def2-TZVP}$ level of theory). Vertical excitation energies for the first excited anion states were calculated using time-dependent DFT (TDDFT) at the $\omega\text{B97X-D3}/\text{ma-def2-TZVP}$ level of theory.

4. Conclusions

Dissociative electron attachment to $\text{Pt}(\text{CO})_2\text{Br}_2$ in the energy range from about 0 to 12 eV and dissociative ionization at 70 eV were studied in a crossed electron-molecule beam experiment. The thermochemical thresholds for all DEA channels were calculated, and relaxed potential energy surface scans were computed for the main channels. The vertical electron attachment energies and the respective MOs were calculated for the lowest lying anionic states as well as the vertical transition energy from the anionic ground state to the first excited anionic state for the Pt(II) halogen carbonyls $\text{Pt}(\text{CO})_2\text{X}$ ($\text{X} = \text{F}, \text{Cl}, \text{Br}$ and I). In DI at 70 eV, the main contributions are from the parent ion $[\text{Pt}(\text{CO})_2\text{Br}_2]^+$, but the loss of one and two CO, $[\text{Pt}(\text{CO})\text{Br}_2]^+$ and $[\text{PtBr}_2]^+$, and the formation of PtBr^+ and the bare Pt^+ ion are also significant. The loss of one and two Br, $[\text{Pt}(\text{CO})_2\text{Br}]^+$ and $[\text{Pt}(\text{CO})_2]^+$, the formation of $[\text{Pt}(\text{CO})\text{Br}]^+$, and the platinum carbide PtC^+ and Br^+ are also apparent, though with lesser intensities. All DEA channels, except the formation of PtBr^- were found to be exothermic, and the dominating DEA channels are the loss of one and two CO leading to the formation of $[\text{Pt}(\text{CO})\text{Br}_2]^-$ and $[\text{PtBr}_2]^-$, while Br loss is insignificant. The CO loss appears predominantly through fairly broad contributions in the respective ion yields, peaking close to 0 eV and markedly asymmetric towards higher energies. We attribute these to overlapping contributions from the anionic ground state of a mixed $\pi^* \text{CO}, \text{Pt } 5d_{xz}$ and the first electronically excited anionic state, which is of a σ^* , $\text{Pt } d_{x^2-y^2}$ character. The overall behavior of $[\text{Pt}(\text{CO})_2\text{Br}_2]$ with respect to electron-induced dissociation is similar to what has been observed for $[\text{Pt}(\text{CO})_2\text{Cl}_2]$ [28], and the differences observed can at large be attributed to the weaker Pt–Br bond as compared to Pt–Cl and the resulting

lower dissociation thresholds. Compared to the widely used cancer therapeutic cisplatin, the behavior of the Pt(II) carbonyl halides with respect to low-energy electron-induced dissociation is very different. While the dominating DEA channels in the Pt(II) carbonyl halides are the loss of one and two CO and halogen loss is negligible, the main fragments observed in DEA to $[\text{Pt}(\text{NH}_3)_2\text{Cl}_2]$ are $[\text{Pt}(\text{NH}_3)_2\text{Cl}]^-$, Cl^- and $[\text{Pt}(\text{NH}_3)_2]^-$ [20]. Hence, cleavage of the Pt–halogen bonds dominates. From the thermochemical point of view, this is not expected as the Pt–NH₃ bond is significantly weaker than the Pt–Cl bond (1.5 eV vs. 3.3 eV in cisplatin) [20]. However, the anionic ground state of cisplatin has a repulsive σ^* character unlike the π^*_{CO} character of the anionic ground state of the Pt(II) carbonyl halides. Relaxation of $[\text{Pt}(\text{NH}_3)_2\text{Cl}_2]^-$ from its anionic ground state, through Pt–Cl bond rupture along the σ^* coordinates is thus a direct process. This is not the case for the π^* , CO character anionic ground state of $[\text{Pt}(\text{CO})_2\text{Cl}_2]^-$ and $[\text{Pt}(\text{CO})_2\text{Br}_2]^-$ where this process is symmetry forbidden and effective coupling of the π^*_{CO} component with the respective σ^* states is necessary to effectuate dissociation.

Author Contributions: Conceptualization, F.F.d.S., O.I. and L.M.-W.; compound synthesis, L.M.-W. and H.L.; experimental data acquisition, S.S., F.F.d.S. and O.I.; theoretical calculations, M.C.; data curation, M.C.; writing—original draft preparation, M.C.; writing—review and editing, O.I., M.C., F.F.d.S., L.M.-W. and H.L.; visualization, M.C. All authors have read and agreed to the published version of the manuscript.

Funding: This project was conducted within the framework of ELENA, a Horizon 2020 research and innovation program under Marie Skłodowska-Curie Innovative Training Network, under the grant agreement No. 722149. M.C. and O.I. acknowledge support from the Icelandic Center of Research (RANNIS), grant no. 13049305(1–3). M.C. acknowledges a doctoral grant from the University of Iceland Research Fund. H.L. and L.M.-W. thank the National Science Foundation for support under grants CHE-1607547 and CHE-1904802. F.F.d.S. acknowledges the Portuguese National Funding Agency for Science Research and Technology (FCT-MCTES), through the research grants PTDC/FIS-AQM/31215/2017 and UIDB/00068/2020 (CEFITEC).

Institutional Review Board Statement: Not applicable.

Informed Consent Statement: Not applicable.

Data Availability Statement: The data underlying this article will be shared on reasonable request from the corresponding author.

Conflicts of Interest: The authors declare no conflict of interest. The funders had no role in the design of the study; in the collection, analyses, or interpretation of data; in the writing of the manuscript, or in the decision to publish the results.

References

1. Wilson, G.D.; Bentzen, S.M.; Harari, P.M. Biologic Basis for Combining Drugs With Radiation. *Semin. Radiat. Oncol.* **2006**, *16*, 2–9. [[CrossRef](#)] [[PubMed](#)]
2. Kelland, L. The resurgence of platinum-based cancer chemotherapy. *Nat. Rev. Cancer* **2007**, *7*, 573–584. [[CrossRef](#)] [[PubMed](#)]
3. Hanna, N.; Einhorn, L.H. Testicular Cancer: A Reflection on 50 Years of Discovery. *J. Clin. Oncol.* **2014**, *32*, 3085–3092. [[CrossRef](#)] [[PubMed](#)]
4. Einhorn, E.H. Testicular cancer: An oncological success story. *Clin. Cancer Res.* **1997**, *3*, 2630–2632. [[PubMed](#)]
5. Glover, D.; Grabelsky, S.; Fox, K.; Weiler, C.; Cannon, L.; Glick, J. Clinical trials of WR-2721 and cis-platinum. *Int. J. Radiat. Oncol.* **1989**, *16*, 1201–1204. [[CrossRef](#)]
6. Brabec, V. Chemistry and Structural Biology of 1,2-Interstrand Adducts of Cisplatin. In *Platinum-Based Drugs in Cancer Therapy*; Kelland, L.R., Farrell, N.P., Eds.; Humana Press: Totowa, NJ, USA, 2000; Volume 1, pp. 37–63. [[CrossRef](#)]
7. Zheng, Y.; Hunting, D.J.; Ayotte, P.; Sanche, L. Role of Secondary Low-Energy Electrons in the Concomitant Chemoradiation Therapy of Cancer. *Phys. Rev. Lett.* **2008**, *100*, 198101. [[CrossRef](#)]
8. Dąbkowska, I.; Rak, J.; Gutowski, M. DNA strand breaks induced by concerted interaction of H radicals and low-energy electrons. *Eur. Phys. J. D* **2005**, *35*, 429–435. [[CrossRef](#)]
9. Landheer, K.; Rosenberg, S.G.; Bernau, L.; Swiderek, P.; Utke, I.; Hagen, C.W.; Fairbrother, D.H. Low-Energy Electron-Induced Decomposition and Reactions of Adsorbed Tetrakis(trifluorophosphine)platinum $[\text{Pt}(\text{PF}_3)_4]$. *J. Phys. Chem. C* **2011**, *115*, 17452–17463. [[CrossRef](#)]

10. Hedhili, M.N.; Bredehöft, J.H.; Swiderek, P. Electron-Induced Reactions of MeCpPtMe₃ Investigated by HREELS. *J. Phys. Chem. C* **2009**, *113*, 13282–13286. [[CrossRef](#)]
11. Wnuk, J.D.; Gorham, J.M.; Rosenberg, S.G.; van Dorp, W.F.; Madey, T.E.; Hagen, C.W.; Fairbrother, D.H. Electron Induced Surface Reactions of the Organometallic Precursor Trimethyl(methylcyclopentadienyl)platinum(IV). *J. Phys. Chem. C* **2009**, *113*, 2487–2496. [[CrossRef](#)]
12. Spencer, J.A.; Wu, Y.-C.; McElwee-White, L.; Fairbrother, D.H. Electron Induced Surface Reactions of cis -Pt(CO)₂Cl₂: A Route to Focused Electron Beam Induced Deposition of Pure Pt Nanostructures. *J. Am. Chem. Soc.* **2016**, *138*, 9172–9182. [[CrossRef](#)] [[PubMed](#)]
13. Rohdenburg, M.; Martinović, P.; Ahlenhoff, K.; Koch, S.; Emmrich, D.; Götzhäuser, A.; Swiderek, P. Cisplatin as a Potential Platinum Focused Electron Beam Induced Deposition Precursor: NH₃ Ligands Enhance the Electron-Induced Removal of Chlorine. *J. Phys. Chem. C* **2019**, *123*, 21774–21787. [[CrossRef](#)]
14. Utke, I.; Hoffmann, P.; Melngailis, J. Gas-assisted focused electron beam and ion beam processing and fabrication. *J. Vac. Sci. Technol. B Microelectron. Nanom. Struct.* **2008**, *26*, 1197. [[CrossRef](#)]
15. LaVerne, J.A.; Pimblott, S.M. Electron Energy-Loss Distributions in Solid, Dry DNA. *Radiat. Res.* **1995**, *141*, 208. [[CrossRef](#)] [[PubMed](#)]
16. Cobut, V. Monte Carlo simulation of fast electron and proton tracks in liquid water—I. physical and physicochemical aspects. *Radiat. Phys. Chem.* **1998**, *51*, 229–243. [[CrossRef](#)]
17. Pimblott, S.M.; LaVerne, J.A. Production of low-energy electrons by ionizing radiation. *Radiat. Phys. Chem.* **2007**, *76*, 1244–1247. [[CrossRef](#)]
18. Sanche, L. Low energy electron-driven damage in biomolecules. *Eur. Phys. J. D* **2005**, *35*, 367–390. [[CrossRef](#)]
19. Boudaïffa, B.; Cloutier, P.; Hunting, D.; Huels, M.A.; Sanche, L. Resonant formation of DNA strand breaks by low-energy (3 to 20 eV) electrons. *Science* **2000**, *287*, 1658–1660. [[CrossRef](#)]
20. Kopyra, J.; Koenig-Lehmann, C.; Bald, I.; Illenberger, E. A Single Slow Electron Triggers the Loss of Both Chlorine Atoms from the Anticancer Drug Cisplatin: Implications for Chemoradiation Therapy. *Angew. Chem. Int. Ed.* **2009**, *48*, 7904–7907. [[CrossRef](#)]
21. Schaefer, J.; Hoelzl, J. A contribution to the dependence of secondary electron emission from the work function and fermi energy. *Thin Solid Films* **1972**, *13*, 81–86. [[CrossRef](#)]
22. Ohya, K.; Harada, A.; Kawata, J.; Nishimura, K. Monte Carlo Simulation of Yield and Energy Distribution of Secondary Electrons Emitted from Metal Surfaces. *Jpn. J. Appl. Phys.* **1996**, *35*, 6226–6232. [[CrossRef](#)]
23. Utke, I.; Moshkalev, S.; Russell, P. *Nanofabrication Using Focused Ion and Electron Beams: Principles and Applications (Oxford Series in Nanomanufacturing Book 1)*; Oxford University Press Inc.: New York, NY, USA, 2012.
24. Ingólfsson, O. *Low-Energy Electrons: Fundamentals and Applications*; Pan Stanford Publishing Pte. Ltd.: Singapore, 2019.
25. Engmann, S.; Stano, M.; Matejčík, Š.; Ingólfsson, O. Gas phase low energy electron induced decomposition of the focused electron beam induced deposition (FEBID) precursor trimethyl (methylcyclopentadienyl) platinum(IV) (MeCpPtMe₃). *Phys. Chem. Chem. Phys.* **2012**, *14*, 14611. [[CrossRef](#)] [[PubMed](#)]
26. May, O.; Kubala, D.; Allan, M. Dissociative electron attachment to Pt(PF₃)₄—A precursor for Focused Electron Beam Induced Processing (FEBIP). *Phys. Chem. Chem. Phys.* **2012**, *14*, 2979–2982. [[CrossRef](#)] [[PubMed](#)]
27. Zlatar, M.; Allan, M.; Fedor, J. Excited States of Pt(PF₃)₄ and Their Role in Focused Electron Beam Nanofabrication. *J. Phys. Chem. C* **2016**, *120*, 10667–10674. [[CrossRef](#)]
28. Ferreira da Silva, F.; Thorman, R.M.; Björnsson, R.; Lu, H.; McElwee-White, L.; Ingólfsson, O. Dissociation of the FEBID precursor cis-Pt(CO)₂Cl₂ driven by low-energy electrons. *Phys. Chem. Chem. Phys.* **2020**, *22*, 6100–6108. [[CrossRef](#)]
29. Mahgoub, A.; Lu, H.; Thorman, R.M.; Preradovic, K.; Jurca, T.; McElwee-White, L.; Fairbrother, H.; Hagen, C.W. Electron beam-induced deposition of platinum from Pt(CO)₂Cl₂ and Pt(CO)₂Br₂. *Beilstein J. Nanotechnol.* **2020**, *11*, 1789–1800. [[CrossRef](#)]
30. Rohdenburg, M.; Boeckers, H.; Brewer, C.R.; McElwee-White, L.; Swiderek, P. Efficient NH₃-based process to remove chlorine from electron beam deposited ruthenium produced from (η³-C₃H₅)Ru(CO)₂Cl. *Sci. Rep.* **2020**, *10*, 10901. [[CrossRef](#)]
31. Desfrancois, C.; Abdoul-Carime, H.; Schermann, J.-P. Ground-state dipole-bound anions. *Int. J. Mod. Phys. B* **1996**, *10*, 1339–1395. [[CrossRef](#)]
32. Sommerfeld, T. Dipole-bound states as doorways in (dissociative) electron attachment. *J. Phys. Conf. Ser.* **2005**, *4*, 245–250. [[CrossRef](#)]
33. Bjarnason, E.H.; Ómarsson, B.; Engmann, S.; Ómarsson, F.H.; Ingólfsson, O. Dissociative electron attachment to titanium tetrachloride and titanium tetraisopropoxide. *Eur. Phys. J. D* **2014**, *68*, 121. [[CrossRef](#)]
34. Braun, M.; Marienfeld, S.; Ruf, M.-W.; Hotop, H. High-resolution electron attachment to the molecules CCl₄ and SF₆ over extended energy ranges with the (EX)LPA method. *J. Phys. B At. Mol. Opt. Phys.* **2009**, *42*, 125202. [[CrossRef](#)]
35. Bagnoli, F.; Belli Dell'Amico, D.; Calderazzo, F.; Englert, U.; Marchetti, F.; Merigo, A.; Ramello, S. Halo-carbonyl complexes of platinum(II) and palladium(II). *J. Organomet. Chem.* **2001**, *622*, 180–189. [[CrossRef](#)]
36. Neese, F. Software update: The ORCA program system, version 4.0. *WIREs Comput. Mol. Sci.* **2018**, *8*. [[CrossRef](#)]
37. Chai, J.-D.; Head-Gordon, M. Long-range corrected hybrid density functionals with damped atom-atom dispersion corrections. *Phys. Chem. Chem. Phys.* **2008**, *10*, 6615. [[CrossRef](#)] [[PubMed](#)]
38. Grimme, S.; Antony, J.; Ehrlich, S.; Krieg, H. A consistent and accurate ab initio parametrization of density functional dispersion correction (DFT-D) for the 94 elements H-Pu. *J. Chem. Phys.* **2010**, *132*, 154104. [[CrossRef](#)] [[PubMed](#)]

39. Weigend, F.; Ahlrichs, R. Balanced basis sets of split valence, triple zeta valence and quadruple zeta valence quality for H to Rn: Design and assessment of accuracy. *Phys. Chem. Chem. Phys.* **2005**, *7*, 3297. [[CrossRef](#)] [[PubMed](#)]
40. Zheng, J.; Xu, X.; Truhlar, D.G. Minimally augmented Karlsruhe basis sets. *Theor. Chem. Acc.* **2011**, *128*, 295–305. [[CrossRef](#)]
41. Andrae, D.; Häußermann, U.; Dolg, M.; Stoll, H.; Preuß, H. Energy-adjusted ab initio pseudopotentials for the second and third row transition elements. *Theor. Chim. Acta* **1990**, *77*, 123–141. [[CrossRef](#)]
42. Riplinger, C.; Neese, F. An efficient and near linear scaling pair natural orbital based local coupled cluster method. *J. Chem. Phys.* **2013**, *138*, 034106. [[CrossRef](#)]
43. Riplinger, C.; Pinski, P.; Becker, U.; Valeev, E.F.; Neese, F. Sparse maps—A systematic infrastructure for reduced-scaling electronic structure methods. II. Linear scaling domain based pair natural orbital coupled cluster theory. *J. Chem. Phys.* **2016**, *144*, 024109. [[CrossRef](#)]
44. Riplinger, C.; Sandhoefer, B.; Hansen, A.; Neese, F. Natural triple excitations in local coupled cluster calculations with pair natural orbitals. *J. Chem. Phys.* **2013**, *139*, 134101. [[CrossRef](#)]
45. Saitow, M.; Becker, U.; Riplinger, C.; Valeev, E.F.; Neese, F. A new near-linear scaling, efficient and accurate, open-shell domain-based local pair natural orbital coupled cluster singles and doubles theory. *J. Chem. Phys.* **2017**, *146*, 164105. [[CrossRef](#)] [[PubMed](#)]
46. Dunning, T.H. Gaussian basis sets for use in correlated molecular calculations. I. The atoms boron through neon and hydrogen. *J. Chem. Phys.* **1989**, *90*, 1007–1023. [[CrossRef](#)]
47. Woon, D.E.; Dunning, T.H. Gaussian basis sets for use in correlated molecular calculations. III. The atoms aluminum through argon. *J. Chem. Phys.* **1993**, *98*, 1358–1371. [[CrossRef](#)]
48. Kendall, R.A.; Dunning, T.H.; Harrison, R.J. Electron affinities of the first-row atoms revisited. Systematic basis sets and wave functions. *J. Chem. Phys.* **1992**, *96*, 6796–6806. [[CrossRef](#)]
49. Figgen, D.; Peterson, K.A.; Dolg, M.; Stoll, H. Energy-consistent pseudopotentials and correlation consistent basis sets for the 5d elements Hf–Pt. *J. Chem. Phys.* **2009**, *130*, 164108. [[CrossRef](#)]

Article III

HF Formation through Dissociative Electron Attachment—A Combined Experimental and Theoretical Study on Pentafluorothiophenol and 2-Fluorothiophenol

Maicol Cipriani and Oddur Ingólfsson

International Journal of Molecular Sciences, 2022, 23(5), 2430

This is an open access article distributed under the Creative Commons Attribution License CC BY 4.0

Maicol Cipriani actively participated in developing the research concept and carried out measurements. He conducted all computational work and a major part of data analysis. He wrote the first draft of the manuscript and contributed to editing until publication



Article

HF Formation through Dissociative Electron Attachment—A Combined Experimental and Theoretical Study on Pentafluorothiophenol and 2-Fluorothiophenol

Maicol Cipriani and Oddur Ingólfsson *

Department of Chemistry and Science Institute, University of Iceland, Dunhagi 3, 107 Reykjavik, Iceland; mac31@hi.is

* Correspondence: odduring@hi.is

Abstract: In chemoradiation therapy, dissociative electron attachment (DEA) may play an important role with respect to the efficiency of the radiosensitizers used. The rational tailoring of such radiosensitizers to be more susceptible to DEA may thus offer a path to increase their efficiency. Potentially, this may be achieved by tailoring rearrangement reactions into the DEA process such that these may proceed at low incident electron energies, where DEA is most effective. Favorably altering the orbital structure of the respective molecules through substitution is another path that may be taken to promote dissociation up on electron capture. Here we present a combined experimental and theoretical study on DEA in relation to pentafluorothiophenol (PFTP) and 2-fluorothiophenol (2-FTP). We investigate the thermochemistry and dynamics of neutral HF formation through DEA as means to lower the threshold for dissociation up on electron capture to these compounds, and we explore the influence of perfluorination on their orbital structure. Fragment ion yield curves are presented, and the thermochemical thresholds for the respective DEA processes are computed as well as the minimum energy paths for HF formation up on electron capture and the underlying orbital structure of the respective molecular anions. We show that perfluorination of the aromatic ring in these compounds plays an important role in enabling HF formation by further lowering the threshold for this process and through favorable influence on the orbital structure, such that DEA is promoted. We argue that this approach may offer a path for tailoring new and efficient radiosensitizers.

Keywords: chemoradiation; radiosensitizers; low-energy electron interaction; perfluorination; HF formation; pentafluorothiophenol; 2-fluorothiophenol; dissociative electron attachment



Citation: Cipriani, M.; Ingólfsson, O. HF Formation through Dissociative Electron Attachment—A Combined Experimental and Theoretical Study on Pentafluorothiophenol and 2-Fluorothiophenol. *Int. J. Mol. Sci.* **2022**, *23*, 2430. <https://doi.org/10.3390/ijms23052430>

Academic Editor: Henry Chermette

Received: 20 January 2022

Accepted: 22 February 2022

Published: 23 February 2022

Publisher's Note: MDPI stays neutral with regard to jurisdictional claims in published maps and institutional affiliations.



Copyright: © 2022 by the authors. Licensee MDPI, Basel, Switzerland. This article is an open access article distributed under the terms and conditions of the Creative Commons Attribution (CC BY) license (<https://creativecommons.org/licenses/by/4.0/>).

1. Introduction

In recent years, appreciable attention has been paid to the interaction of low-energy electrons (LEEs) with DNA and radiosensitizers applied in cancer therapy [1–6]. Although much progress has been made in the fight against cancer, tumor hypoxia still represents an obstacle to traditional cancer therapy. Hypoxia is generally present in solid tumors due to their limited vascularization. The decrease in O₂ availability in tumor masses may make chemotherapy and radiotherapy ineffective [7–10]. A more efficient therapy is the concomitant application of radiation with oxygen-mimetic radiosensitizers, most commonly nitro-imidazoles [11,12]. In these electron-affinic radiosensitizers, the nitro group binds with the DNA free radicals generated by ionizing radiation and consequently induces DNA strand breaks [12]. However, at the microscopic level, low-energy electron (LEE) interaction plays an important role in sensitizing cancer cells to radiation [3,13]. The interaction of the ionizing radiation with a biological tissue generates LEEs (<20 eV) with energy distribution that peaks at or below 10 eV, with appreciable contribution close to 0 eV and a tail extending to higher energies [14]. At electron energies below 10 eV, electron-affinic radiosensitizers can be subjected to LEE induced reactions, which yield radical species that can damage DNA. In an aqueous medium, LEEs solvate on a picosecond scale [15].

However, before solvation, an LEE can occupy a vacant virtual orbital of a radiosensitizer, giving rise to a transient negative ion (TNI). If reaction channels are available at these electron energies, a TNI can undergo fragmentation via dissociative electron attachment (DEA), generating a negatively charged ion and neutral counter-fragment(s) [16,17]. This process is in competition with the relaxation of the TNI through autodetachment, i.e., the re-emission of the electron without fragmentation. The electron attachment process, which is the formation of the TNI, is most efficient at low energies, and the autodetachment lifetime decreases rapidly with increasing electron energies. Thus, DEA is most efficient at very low incident electron energies, given that the respective dissociation channel is thermochemically accessible. Hence, exothermic DEA processes, which may proceed close to 0 eV electron energy, are most efficient. The important role of LEEs and DEA in DNA radiolysis was shown by Boudaiffa et al. [1] already in the year 2000, in a study where the authors demonstrated that DEA processes can trigger single and double-strand breaks. This work triggered manifold studies on LEE interaction with DNA components and the fragmentation of negative ions of DNA components, with the bulk of this work being reviewed, for example, in references [18–22]. Furthermore, LEE interaction with radiosensitizers has also been investigated in a number of studies [3–6,23–25]. In these studies, it has, e.g., been shown for 5-halouracils that halogenation increases the DEA cross-sections and such halogenated uracils present sharp peaks with high cross sections in the 0–4 eV electron energy range [23]. In this context, it has also been shown that substitution of thymine with the higher electron affinity 5-halouraci significantly sensitizes DNA to radiation [26]. Similarly, Rackwitz et al. [24] have shown enhanced strand-break efficiency through DEA to DNA oligonucleotides when replacing adenine with 2-fluoro adenine, the active component in the chemotherapeutic fludarabine that has also been considered for use in chemoradiation therapy [27–29]. Rackwitz et al. [24] associate the observed strand breaks to resonances they observe in gas phase DEA to 2-fluoro adenine at around 5.5 eV and note that these are shifted towards lower energies when compared to DEA to the native adenine. In addition, DEA to the oxygen-mimetic radiosensitizers 2-nitroimidazole and 4(5)-nitroimidazole has been shown to effectively fragment these molecules [5,6].

Dissociative electron attachment is not limited to single bond ruptures but may also involve the rupture of multiple bonds and the formation of new bonds. The generation of new chemical bonds provides additional energy to the system and can thus promote DEA and open new reaction channels otherwise inaccessible at low electron energies. In recent years, dissociative electron attachment (DEA) reactions leading to neutral HF formation from perfluorinated benzene derivatives have been the object of several studies [30–33]. The formation of HF feeds 5.9 eV into the system, i.e., the bond energy of HF, and can promote reaction channels that involve the rupture of multiple bonds. Omarsson et al. [30,31] conducted detailed experimental and theoretical investigation of HF formation through DEA to pentafluorotoluene (PFT), pentafluoroaniline (PFA), and pentafluorophenol (PFP). There it was shown that the polarization of the X–H bond plays a determining role in neutral HF formation through the promotion of the formation of an intermediate intramolecular hydrogen bond, X–H...F. In these studies, the authors correlated the different magnitude of the polarization of the X–H bond for X = C, N, and O, with the stabilization of the intermediate X–H...F leading to the HF loss in the respective DEA processes. With respect to the thermochemistry, the HF formation upon DEA to PFP was found to be exothermic, partly attributed the subsequent rearrangement of the charge retaining fragment, while in the case of PFA and PFT, the HF formation was found to be endothermic. In fact, it was also pointed out by Rackwitz et al. [24] that the neutral HF formation may provide the thermochemical prerequisite for the fragmentation effectuated in DEA to 2-fluoro adenine and that such neutral halogen acid formation is frequently observed in DEA to halo-nucleobases.

Motivated by the possibility to promote reaction channels in radiosensitizers through HF formation upon DEA, we extend the previous investigations and compare the two compounds, pentafluorothiophenol (PFTP) and 2-fluorothiophenol (2-FTP). A comparison

between PFTP and 2-FTP is informative as both these compounds may form the intermediate $X-H\cdots F$ to a fluorine in the ortho position of the aromatic ring and thus dissociate by neutral HF loss up on electron attachment. However, the perfluorination of PFTP changes the order of the involved molecular orbitals and also favorably influences the thermochemistry of the process. Furthermore, the comparison of PFTP to PFP is interesting because S and O atoms have similar electron configurations, being neighbors in the same group within the periodic table. Because S is less electronegative than N and O, the process involving the HF formation will not be as well supported by the polarization of the S–H bond. However, the orbital structure of S is more extended than that of O (principal quantum number (n) = 3 as compared to 2 for oxygen), so the S–H bond is longer and weaker than the O–H bond. Thus, R–SH is a stronger acid than R–OH. For the HF formation through DEA to take place close to 0 eV incident electron energy, where the attachment cross section is highest, the electron affinity of the biradical [M–HF] must compensate the energy difference between the cleavage of the two bonds (M–F and M–H) and the formation of the new H–F bond. In addition, 2-FTP has also been the object of a near ultraviolet photodissociation study in regard to the S–H bond cleavage [34], which in turn is a prerequisite for HF formation.

Here we present a combined theoretical and experimental study where we use PFTP and 2-FTP as model compounds to explore the potential of substitution to enhance the susceptibility of such compounds towards low energy electrons. We present ion yield curves for all DEA fragments observed from these compounds and we explore the influence of fluorination on the relative energies of the respective low-lying anionic states in conjunction with the thermochemistry and reaction paths leading to fragmentation up on electron capture. Specifically, we focus on HF formation as a potential means to supply additional energy into the DEA channels in order to move the fragmentation threshold close to 0 eV, where the attachment cross sections are highest. In this study, we show that the perfluorination of the molecule is not only important with respect to the attachment cross-section but also plays an important role with respect to the orbital structure and the thermochemistry behind the HF formation. We discuss the nature of the SOMOs involved in the electron attachment processes, calculate the thermochemical thresholds of these processes, and compute the minimum energy paths for HF loss for both compounds. We argue that such molecular functionalization may serve as a basis for the design of more efficient radiosensitizers.

2. Results and Discussion

Figure 1 shows negative ion yield curves for observed fragments formed through DEA to PFTP (left) and 2-FBT (right), respectively. The ion yield curves are shown for the incident electron energy range from approximately 0 to 10 eV and are normalized to the respective target gas pressure and the relative cross-section of SF_6^- formation from SF_6 at 0 eV incident electron energy.

The most pronounced DEA channel for PFTP leads to neutral HF loss from the transient negative ion (TNI) formed in the initial attachment process, that is the formation of $[M-HF]^-$. This channel is most significant at threshold, i.e., at 0 eV, but has a higher-lying contribution centered at around 4.7 eV, which is approximately three orders of magnitude lower in intensity. The contribution peaking at approximately 0 eV is distinctly asymmetric towards higher energies, and we anticipate that this is due to overlapping contributions from two distinct resonances. Hydrogen loss is also observed from PFTP at low energies (at approximately 0.3 eV) and through a higher-lying resonance appearing in the ion yield curves at approximately 4.5 eV. The relative, maximum cross-section for the hydrogen loss from this molecule, that is the $[M-H]^-$ formation at 0.3 eV, is two orders of magnitude lower than that for the HF formation. However, the relative cross-section for the $[M-H]^-$ contribution from PFTP at approximately 4.5 eV is three orders of magnitude higher than that for the $[M-HF]^-$ formation at approximately 4.7 eV. This is understandable, as the attachment cross-section is significantly higher close to 0 eV as compared to 0.3 eV; however, at energies significantly above threshold, at approximately 4.5 eV in this case, direct

dissociation such as the hydrogen loss is expected to be more efficient as compared to rearrangement processes such as the HF formation. Finally, DEA to PFTP also leads to the loss of SH, i.e., the observation of the anionic fragment $[M-SH]^-$. Similar to the HF formation and the H loss ion yield curves, the $[M-SH]^-$ ion yield curve has a low energy contribution with an onset at approximately 0 eV and peak intensity at approximately 0.8 eV and a less intense second contribution at higher energy that is centered at approximately 4 eV. The maximum relative cross section for the $[M-SH]^-$ is three orders of magnitude lower than that for the $[M-HF]^-$ formation, i.e., an order of magnitude lower than that for $[M-H]^-$. This channel leads to the formation of the stable pentafluorbenzenide anion.

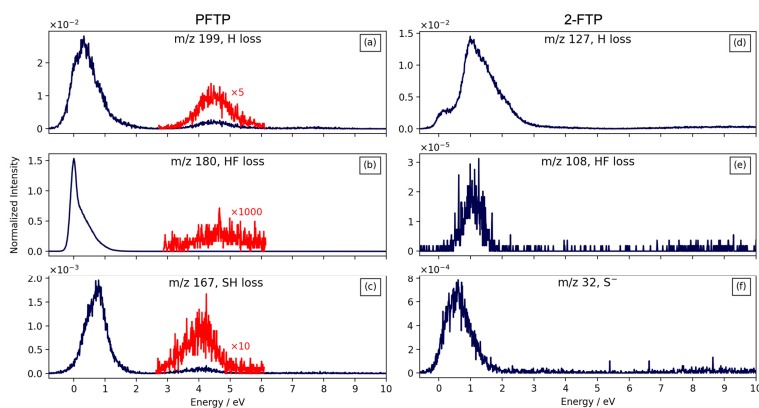


Figure 1. Left: DEA ion yield curves from PFTP for the channels: (a) H loss, (b) HF loss, and (c) SH loss. Right: DEA ion yield curves from 2-FTP for the channels: (d) H loss, (e) HF loss, (f) S^- formation. The intensities are normalized with respect to the target gas pressure and the formation of SF_6^- from SF_6 at 0 eV incident electron energy.

Dissociative electron attachment to 2-FBT also leads to the formation of $[M-H]^-$ and $[M-HF]^-$ through resonances at low incident electron energies. These contributions both have their maxima at approximately 1.0 eV. However, unlike PFTP, the relative cross-section for the HF loss from 2-FTP, i.e., the formation of $[M-HF]^-$, is three orders of magnitude lower than that for the direct hydrogen loss, $[M-H]^-$. The low energy contribution to the $[M-H]^-$ formation from 2-FTP is composed of a contribution at approximately 0 eV, appearing as a low energy shoulder on the main contribution that peaks at approximately 1 eV and is asymmetric towards high energies. We attribute this 0 eV shoulder to ‘hot-band transitions’ or I^- ($m/z = 127$) from some iodine containing compound residual in the 2-FTP sample or possibly in our inlet system. The assignments of the resonance reflected in the low energy $[M-H]^-$ contribution is discussed in more details below. In addition to the $[M-H]^-$ and $[M-HF]^-$ channels, the formation of S^- is also observed in DEA to 2-FTP. This channel is, similarly to the others, most efficient at low energies, with an onset at approximately 0 eV and a maximum cross-section at approximately 0.6 eV. The maximum relative cross-section for the S^- formation from 2-FTP is approximately two orders of magnitude lower than that for the hydrogen loss from this compound.

Hence, while the most pronounced DEA channel for 2-FTP is direct hydrogen loss, HF loss is the dominating DEA channel from PFTP. In fact, the relative cross section for neutral

HF formation from 2-FTP is five orders of magnitude lower than that for HF formation from 2-FTP. Furthermore, the onset of the HF loss from 2-FTP is at approximately 0.5 eV, indicating that this channel is endothermic, while the cross section for HF loss from PFTP peaks at approximately 0 eV, as would be expected for an exothermic process.

In order to elucidate the thermochemistry and the dynamics of the DEA processes for PFTP and 2-FTP, we have calculated the 0K reaction enthalpies (ΔH_{0K}) at the B3LYP D3BJ/ aug-cc-pVTZ level of theory for all the observed fragments. These are given in Table 1 along with the thermally corrected values (ΔE_{th}) derived by adding the thermal energy correction at room temperature to the parent molecule. This approach is taken as we expect thermal equilibrium for the parent molecules within the inlet system, but not for the DEA fragments formed under single collision conditions. For the HF formation, we additionally considered a rearrangement of the aromatic ring whereby the 6-membered benzene ring is rearranged to a 5-membered ring with an exocyclic-CS moiety: $C_5F_4CS^-$ and $C_5H_4CS^-$, respectively, see Figure 2.

Table 1. Calculated 0K reaction enthalpies (ΔH_{0K}) and thermally corrected thresholds (ΔE_{th}) for the fragments observed in DEA to PFTP and 2-FTP. For the HF loss, the values are shown for both the direct process, $[M-HF]^- / C_6F_5S^-$ or $C_6H_4S^-$ and for the rearrangement process shown in Figure 2, $[M-HF]^- / C_5F_4CS^-$ or $C_5H_4CS^-$. At the bottom of the table, the same values are calculated for the HF formation upon DEA to PFP. The calculations are performed at the B3LYP D3BJ/ aug-cc-pVTZ level of theory.

<i>m/z</i>	Fragment	ΔH_{0K}	ΔE_{th}
PFTP			
199	$[M-H]^- / C_6F_5S^-$	0.42	0.13
180	$[M-HF]^- / C_6F_4S^-$	-0.0084	-0.29
180	* $[M-HF]^- / C_5F_4CS^-$	-0.066	-0.35
167	$[M-SH]^- / C_6F_5^-$	0.61	0.32
2-FTP			
127	$[M-H]^- / C_6H_4FS^-$	1.03	0.84
108	$[M-HF]^- / C_6H_4S^-$	0.62	0.42
108	* $[M-HF]^- / C_5H_4CS^-$	0.47	0.28
32	S^-	0.33	0.14
PFP			
164	$[M-HF]^- / C_6F_4O^-$	-0.066	-0.33
164	* $[M-HF]^- / C_5F_4CO^-$	-0.27	-0.54

* Calculated threshold considering the rearrangement of the ring after the HF formation.

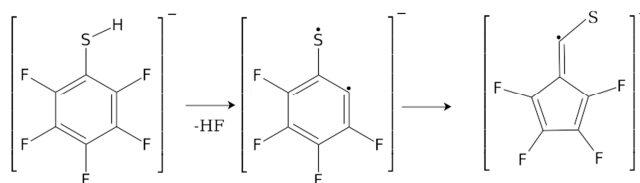


Figure 2. Considered rearrangement of the phenyl ring subsequent to the HF loss upon DEA to PFTP and 2-FTP. In the figure, this is shown for PFTP as an example. In this process, after the HF loss, the 6-membered benzene ring rearranges into a 5-membered ring with exocyclic-CS.

This rearrangement was proposed by Ómarsson et al. [30,31] in their studies on DEA to PFP, PFA, and PFT. Similar to PFTP, effective HF loss from PFP was observed at 0 eV in those studies, while the direct HF loss from PFP, calculated at the B2PLYP/aug-*pc*-2 level of theory, was found to be endothermic by 0.59 eV. However, in better agreement with the experimental results, a rearrangement leading to a 5-membered ring structure of the anion resulted in a threshold at -0.19 eV. For comparison, we have also calculated the thresholds (ΔE_{th}) and 0K reaction enthalpies (ΔH_{0K}) for HF formation upon DEA to PFP at the B3LYP D3BJ/aug-*cc*-pVTZ level of theory and, in fact, at this level of theory, we find the direct HF loss to be exothermic. In addition to the B3LYP D3BJ/aug-*cc*-pVTZ calculations for PFTP and 2-FTP, shown in Table 1, we have also performed calculations at the ω B97X-D3/aug-*cc*-pVTZ, ω B97X-D3/aug-*cc*-pVQZ, and DLPNO-CCSD(T)/aug-*cc*-pVQZ levels of theory for HF formation upon DEA to PFTP and PFP; these give qualitatively the same results and are presented as Supporting Material in Table S1.

According to our calculations (shown in Table 1), the direct HF formation from PFTP is exothermic by 0.29 eV, and rearrangement of the charge-retaining ring only lowers the threshold to -0.35 eV. For the H and SH losses from PFTP, the calculated thermochemical thresholds were found to be 0.13 and 0.32 eV, respectively. This is in good agreement with our experimental results, where the peak intensities for PFTP are found to be at 0.0 eV for the exothermic HF loss, while the endothermic H and the HS losses are shifted to slightly higher energies. Furthermore, the high relative cross-section for the $[M-HF]^+$ formation is consistent with the higher attachment cross-section expected at threshold (~ 0.0 eV) [35].

For 2-FTP, at the B3LYP D3BJ/aug-*cc*-pVTZ level of theory, we found the thermochemical threshold for the direct HF loss, Table 1, to be 0.42 eV and considering the rearrangement of the ring we found the threshold to be 0.28 eV. The hydrogen loss is found to be energetically less favorable, i.e., endothermic by 0.84 eV. In fact, this is a 0.61 eV higher threshold than the respective threshold for hydrogen loss from PFTP. This is mainly a result of the perfluorination increasing the electron affinity of the charge-retaining fragment C_6F_4-S as compared to that for C_6H_4F-S . At the B3LYP D3BJ/aug-*cc*-pVTZ level of theory, we found the 0K adiabatic electron affinities of C_6F_5-S and C_6H_4F-S to be 2.18 eV and 1.69 eV, respectively.

Despite the fact that the HF loss from 2-FTP is energetically more favorable than the H loss, the H loss dominates the ion yields observed upon DEA to this compound. The significantly higher cross-section for H loss as compared to HF loss must thus be rooted in the dynamics of these processes. To further explore the dynamics of this process, we have performed NEB-TS calculations at the B3LYP D3BJ/aug-*cc*-pVTZ level of theory to compute the reaction paths for the HF loss from both PFTP and 2-FBT, including the potential rearrangement of the charge retaining phenyl ring as discussed here above. Figures 3 and 4 show the calculated minimum energy paths, on the B3LYP potential energy surface (PES) for the HF formation from PFTP and 2-FTP (step 3) and the subsequent rearrangement of the aromatic ring to form $C_5F_4-CS^-$ and $C_5H_4-CS^-$ (step 9), respectively, from the anionic ground states of PFTP and 2-FTP (step 1). The total energy of the neutral parent molecule, calculated at the B3LYP D3BJ/aug-*cc*-pVTZ level of theory, is set at 0 eV, and the black line extending from the *y*-axis marks the relative energy of the neutral ground states. The open circles correspond to the calculated single point energies of the system along the reaction paths, but the blue line is only meant to guide the eye.

Similar to what appears in the minimum energy path for the HF formation from the ground state of the PFP anion, calculated by Ómarsson et al. [31], the formation of the HF, hydrogen-bonded intermediate in step 3 is favored over the molecular anion. Both in the case of PFTP and 2-FTP, see step 2 in Figures 3 and 4, this process (from step 1 to 3) proceeds with an energy barrier. For PFTP it is approximately 0.4 eV and for 2-FTP it is approximately 0.55 eV, relative to the single point energies of the respective relaxed anionic ground states. However, the relaxed PFTP anionic ground state is already 0.85 eV below the respective relaxed neutral ground state of PFTP. The barrier in step 2 and the relaxed $C_6F_4S^-$ anion, shown in step 4, are thus 0.45 eV and 0.29 eV below the relaxed neutral

ground state of PFTP, respectively. Hence, with respect to the neutral, this is a barrierless exothermic reaction and may thus proceed at the 0.0 eV incident electron energy. This is what is observed in the experiments. For 2-FTP, on the other hand, the anionic ground state is 0.09 eV above the neutral ground state, and the activation barrier, shown in step 2, and the relaxed $C_6H_4S^-$ anion, shown in step 4, lies above the neutral ground state. The saddle point for this process, in step 2, is 0.64 eV above the neutral ground state. Hence, with respect to the neutral, this is a barrierless exothermic reaction and may thus proceed at the 0.0 eV incident electron energy. This is what is observed in the experiments. Furthermore, the energy barrier for the HF loss, step 2 in Figure 4, is comparable to the threshold energy for the direct hydrogen loss. The HF loss can thus only proceed at higher energy, i.e., above the threshold, and this in turn favors the faster, direct hydrogen loss, as is observed in the respective ion yields.

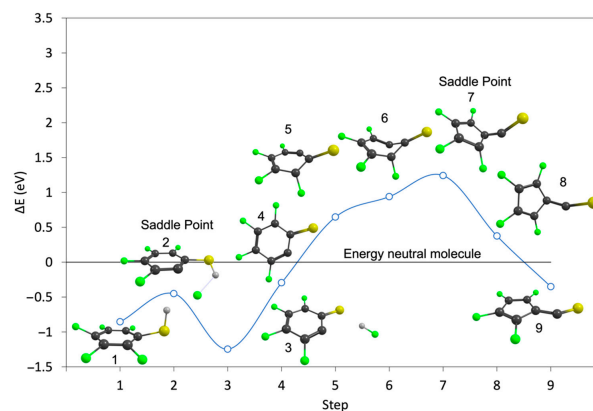


Figure 3. Minimum energy path for the direct HF loss (steps 1–4) and the formation of the 5-membered ring $C_5F_4-CS^-$ (steps 4–9) from the anionic ground state of PFTP (step 1) calculated using the NEB-TS method at the B3LYP D3BJ/aug-cc-pVTZ level of theory. Step 4 corresponds to the direct HF loss, i.e., without the rearrangement of the ring. The single point energies (open circles) along the reaction paths are relative to the energy of the neutral parent molecule, which is set to 0 eV (horizontal black line). ZPVEs and thermal energy correction for the neutral molecule were taken into account.

From step 4, the minimum energy path was further calculated considering rearrangement of the ring to form $C_5F_4-CS^-$ and $C_5H_4-CS^-$ from PFTP and 2-FTP, respectively. The same procedure was applied in Ómarsson et al. [31]. In both PFTP and 2-FTP, the ring rearrangement to the pentagonal structure (from steps 4 to 9) proceeds through a deformation of the ring with a high energy barrier. For PFTP, this reaction is slightly more exothermic than the direct HF loss; however, as can be seen in Figure 3, there is a 1.24 eV reaction barrier on this path for PFTP (from step 4 to 9). This shows that the HF formation from PFTP at 0 eV threshold energy is direct and proceeds without rearrangement of the aromatic ring. Similarly, we find a reaction barrier of approximately 2.3 eV on this reaction path for 2-FTP, showing that the low energy contribution in the $[M-HF]^-$ ion yield from 2-FTP must also be attributed to direct HF loss.

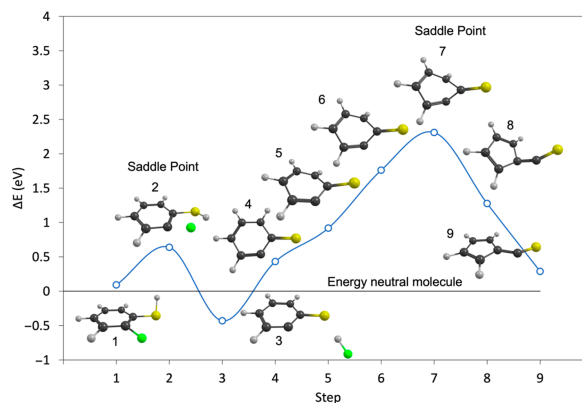


Figure 4. Minimum energy path for the direct HF loss (steps 1–4) and the formation of the 5-membered ring $C_5F_4-CS^-$ (steps 4–9) from the anionic ground state of 2-FTP (step 1), calculated using the NEB-TS method at the B3LYP D3BJ/aug-cc-pVTZ level of theory. Step 4 corresponds to the direct HF loss, i.e., without the rearrangement of the ring. The single point energies (open circles) along the reaction paths are relative to the energy of the neutral parent molecule, which is set to 0 eV (horizontal black line). ZPVEs and thermal energy correction for the neutral molecule were taken into account.

Similarly, our threshold calculations for the $[M-HF]^-$ from PFP, at the B3LYP D3BJ/aug-cc-pVTZ level of theory show that the direct HF loss is also exothermic here (-0.33 eV) and on the minimum energy path for the ring rearrangement in this molecule, Ómarsson et al. [31] found the rearrangement barrier to be close to 2 eV. Therefore, it is reasonable to assume that the $[M-HF]^-$ formation from PFP observed at the 0 eV threshold also occurs as a direct process without involving the rearrangement of the ring.

It is clear from the experiments and the calculations presented above that the perfluorination in PFTP makes the HF loss in DEA energetically more favorable as compared to 2-FTP. Hence, fluorination may potentially be used to sensitize such molecules with respect to DEA by lowering the thermochemical thresholds for these reactions and thus enabling them to proceed at very low energies where the attachment cross section is highest.

With respect to the orbital structure associated with the resonant attachment processes reflected in the ion yields of these compounds, it is worth looking at that of benzene and substituted benzenes. In electron attachment to benzene, the X^2E_{2u} anionic ground state is formed in the gas phase at 1.15 eV through single electron occupation of the doubly degenerate LUMO $e_{2u}(\pi^*)$, as has been assigned through electron transmission spectroscopy [36]. This radical anion distorts due to the Jahn–Teller effect (JT), and the symmetry of the molecule is lowered from D_{6h} to D_{2h} , splitting the degenerated $e_{2u}(\pi^*)$ LUMO into two components: 2A_u and 2B_u [37]. Similarly, the D_{6h} symmetry of the neutral benzene is also broken by substitution at the ring. A single substitution removes the degeneracy of the e_{2u} orbital and lowers the D_{6h} symmetry to C_{2v} , whereby the doubly degenerate $e_{2u}(\pi^*)$ molecular orbital (MO) splits into the components, $a_2(\pi^*)$ and $b_1(\pi^*)$ [38–40]. At the carbon carrying the substituent, the B_1 -type orbital displays maximum electron density, whilst the A_2 -type has a node at this point. The magnitude of the splitting of these orbitals is influenced by the different combination of the mesomeric and the inductive effect of the

respective substituent [41]. While the inductive effect stabilizes both the A_2 and the B_1 anion states, the mesomeric effect destabilizes the B_1 state but generally does not affect the A_2 significantly. Fluorination of aromatic rings moderately lowers the energy of the π^* MOs, but strongly lowers the σ^* MOs due to the strong inductive effect of fluorine as compared to its mesomeric effect [42,43]. This is commonly referred to as the perfluoro effect [38,39]. The geometrical structures and the nature of the ground and excited states of fluoro-substituted benzene anions have been studied, both experimentally and theoretically, for example, with electron-spin resonance techniques [44,45] and electron transmission, inner-shell electron energy loss, and magnetic circular dichroism spectroscopy [46] as well as INDO and Hartree Fock calculations [47,48]. Generally, the findings have been that the energy level of the low-lying σ^* MO decreases with increasing fluorination and, in the case of C_6F_6 , the lowest virtual MO is found to be the σ^* MO. This is visualized informatively in an energy diagram shown in reference [46]. Similar trends have also been observed in heavily fluorinated pyridine anions [49]. Furthermore, in the theoretical studies [47,48], the authors argued that the structure of the polyfluorinated benzene anions undergoes a distortion due to the pseudo-Jahn–Teller effect (pJT), resulting in a planar carbon structure with C–F bonds out of plane. The extra electron occupies a pseudo- π orbital formed by the mixing of the π^* and σ^* orbitals. The $Q_{(b_1)}$ pJT distortion [47] is given by the vibronic interaction between the totally symmetric σ^* state and ${}^2B_1-\pi$ state. As may be seen in comparison to the schematic representation in [47], we note that the $Q_{(b_1)}$ pJT distortion correlates well with the relaxed structure of the PFTP anion optimized at the B3LYP D3BJ/aug-cc-pVTZ level, shown in Figure 5.

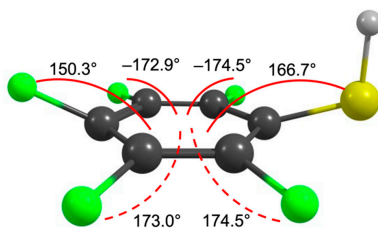


Figure 5. Relaxed geometry of the PFTP anion optimized at the B3LYP D3BJ/aug-cc-pVTZ level of theory. The angles shown in the figure are the angles between the out-of-plane C–F and C–S bonds and the plane of the ring.

Both the influence of fluorination on the order of the lowest lying π^* and σ^* orbitals and the JT distortion up on electron capture is important in DEA to these compounds as a direct dissociation along the substituent's σ^* bond to the aromatic ring is symmetry forbidden from the π^* MOs in the C_{2v} point group [50]. Hence, effective coupling between the respective π^* and σ^* states is required for such dissociation to take place. Occupation of the σ^* orbital, on the other hand, can lead to direct dissociation. This may influence the dissociation cross-section significantly, especially where there is strong competition with autodetachment, and the survival probability of the initially formed TNI is determined.

Figure 6 shows the LUMO, LUMO + 1, and LUMO + 2 of PFTP, along with the respective vertical electron attachment energies calculated using the EOM-EA-CCSD method with the B3LYP orbitals and aug-cc-pVTZ basis set. We note that their values are strongly dependent on the basis set while the order is reliable. Adhering to Jordan et al. [40], we labelled the π^* orbitals according to the C_{2v} point group. The LUMO of PFTP was found to have an σ^* character and is anti-bonding along the C–F and C–S coordinates, and there is a polarization along the S–H bond. From a hydrogen bonded $S\cdots H\cdots F$ intermediate, this provides preferential conditions for HF loss from PFTP and the formation of $[M-HF]^-$.

This is consistent with the high efficiency of the $[M-HF]^-$ formation at approximately 0 eV, assuming that it will proceed from the σ^* electronic ground state of the anion. The vertical attachment energy to this state was found to be 0.15 eV. The LUMO + 1 of PFTP has a π^* character and correlates with the b_1 (π^*) MO. The vertical attachment energy to this orbital is approximately 0.73 eV greater than the respective vertical attachment energy to the σ^* electronic ground state of the anion. This may be explained by the strong inductive effect through the perfluorination stabilizing the σ^* significantly stronger than the π^* . Additionally, the mesomeric effect of the S atom is not strong enough to destabilize the b_1 (π^*) MO and push it above the a_2 (π^*) MO. This is due to the poor overlap of the $3p_x$ orbital of the S atom with the b_1 (π) and b_1 (π^*) orbitals of the benzene ring. We attribute the asymmetry of the low energy peak in the $[M-HF]^-$ ion yield from PFTP to dissociation through single electron occupation of π^* LUMO + 1. The significantly higher intensity through the σ^* ground state may in part be due to the direct dissociation from the σ^* state, as compared to the required coupling of the π^* with the σ^* coordinate, even though such coupling should be promoted by the pJT, causing $\pi^*-\sigma^*$ mixing through the out of plane bending of the fluorine and -SH substituents, as shown in Figure 4. However, the energy dependency of the autodetachment lifetime will also play a significant role. In fact, these effects are intertwined as the DEA cross-section is defined as the product of the electron-attachment cross-section and the survival probability of the TNI [51,52]. With less coupling and increased energy, the autodetachment process becomes more significant, reducing the survival probability with respect to dissociation, which in turn is reflected in lower DEA cross-sections at higher energies. This affects the shape of the peak in the ion yield curve, which appears asymmetric with a long tail on the right side.

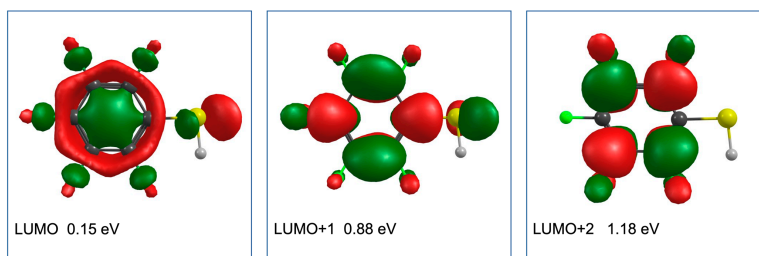


Figure 6. Contour plots of the LUMO, LUMO + 1, and LUMO + 2 of PFTP (B3LYP orbitals). The respective vertical electron attachment energy calculated using the EOM-EA-CCSD method with the B3LYP orbitals and aug-cc-pVTZ basis set are shown for each orbital. The LUMO has a σ^* character, while LUMO + 1 and LUMO + 2 have a π^* character and correlate with b_1 (π^*) and a_2 (π^*) MOs, respectively.

This interpretation is demonstrated in Figure 7, where we present a fitting of the low energy contribution in the negative ion yield curve for neutral HF loss from PFTP upon DEA using a combined fit of normal and skewed gaussian curves. The fitting has been carried out with a python script using the LMFIT library [53]. For the lower energy contribution, the energy dependence of the autodetachment lifetime is neglected (hence, the normal Gaussian) and the natural width of the underlying resonance is considered to be well below the instrumental energy resolution. The FWHM of this contribution in the ion yield should thus reflect the energy resolution of the instrument, but in praxis it is approximately 250 meV. The skewed gaussian curve is chosen for the higher energy component to take into account the asymmetry of the peaks due to the energy dependence of the attachment process and the autodetachment lifetime [16]. With this approach, where we consider

contributions from both the singly occupied LUMO and LUMO + 1, an excellent fit to the low-energy contribution in the $[M-HF]^-$ ion yield from PFTP is obtained.

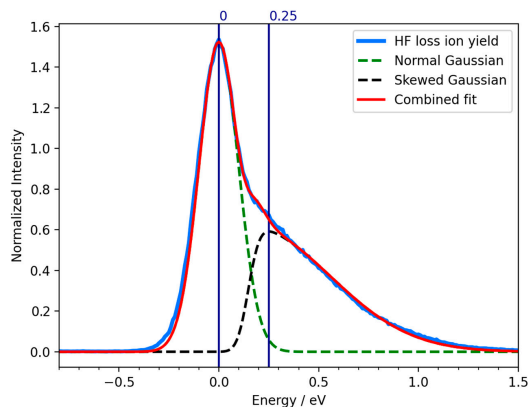


Figure 7. Combined fit of a Normal Gaussian (green dashed line) and a Skewed Gaussian (black dashed line) of the negative ion yield curve (blue line) for neutral HF loss and formation of $[M-HF]^-$ upon DEA from PFTP. The resulting fit is represented by the red line.

This is consistent with the picture in the first low-energy resonance that appears with a peak intensity at 0 eV in the ion yield curves; the unpaired electron is temporarily accommodated in the σ^* MO. In the second resonance, with a maximum contribution at 0.25 eV in the ion yield curve, the extra electron is temporarily placed in the $b_1(\pi^*)$ MO. Here, the autodetachment is significant, and the long tail on the right side of this contribution reflects the lower survival probability at higher attachment energies, due to the shorter lifetime of the respective temporary anion state.

With respect to the LUMO + 2, shown in Figure 5, this correlates with the $a_2(\pi^*)$ MO. This A_2 state has no electron density on the SH substituent, and a $S \cdots H \cdots F$ hydrogen bond formation from this state is not to be expected. Correspondingly we do not expect a contribution from the A_2 TNI to the $[M-HF]^-$ formation. Furthermore, we expect both the $[M-H]^-$ and $[M-SH]^-$ formations to be direct channels that compete with the $[M-HF]^-$ formation. These channels are slightly endothermic, as discussed above, and thus comparatively more efficient at higher energies. The ion yields for these fragments are correspondingly expected to derive their intensity from the high energy side of the σ^* resonance and the $b_1(\pi^*)$ resonance, either directly or through vibrational energy redistribution. Finally, the high-energy contribution at approximately 4.5–4.7 eV in the $[M-HF]^-$, $[M-H]^-$, and $[M-SH]^-$ ion yield curves are most likely routed from the same resonance(s).

Figure 8 shows the LUMO, LUMO + 1, and LUMO + 2 of the 2-FTP, along with the respective vertical attachment energies calculated using the EOM-EA-CCSD method with the B3LYP orbitals and the aug-cc-pVTZ basis set. Different from PFTP, both the LUMO and LUMO + 1 in 2-FTP have a π^* character and, in analogy to the nomenclature used for PFTP, they correlate with the $a_2(\pi^*)$ and $b_1(\pi^*)$ MOs, respectively. From these, the LUMO + 1 is anti-bonding along the C–F coordinate, providing a favorable condition for HF loss and the formation of $[M-HF]^-$. However, different from the direct HF formation from the σ^* SOMO in PFTP, this process is symmetry forbidden from the π^* LUMO + 1 of 2-FTP and requires effective $\pi^*-\sigma^*$ coupling. Calculated at the B3LYP D3BJ/aug-cc-pVTZ level of theory, we

find the threshold for this process to be 0.42 eV, and we anticipate that the low relative cross section for the HF formation from 2-FTP is due to inefficient coupling of the LUMO + 1 with the respective C–F σ^* state, in combination with the high threshold for this process. Hence, at these energies, autodetachment, and conceivably S^- formation, prevail over the HF formation.

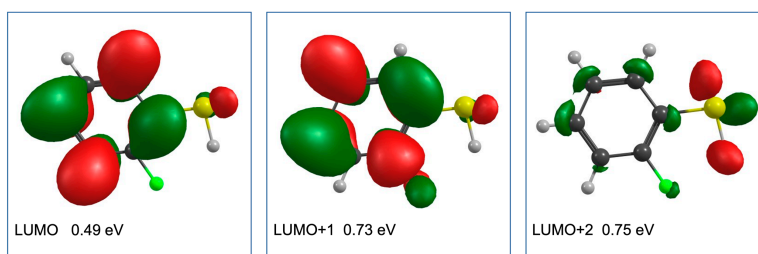


Figure 8. Contour plots of the LUMO, LUMO + 1, and LUMO + 2 of PFTP (B3LYP orbitals). The respective vertical electron attachment energy calculated using the EOM-EA-CCSD method with the B3LYP orbitals and aug-cc-pVTZ basis set are shown for each orbital. The LUMO and LUMO + 1 have a π^* character and correlate with a_2 (π^*) and b_1 (π^*) MOs, respectively, while LUMO + 2 is a partial diffuse orbital with some electron density on the S and H atoms.

The hydrogen loss from 2-FTP is by far the most efficient DEA channel for this molecule and is characterized in the ion yields by a broad asymmetric contribution peaking at 0.88 eV and tailing off towards higher energies. A shoulder at approximately 0 eV in the ion yield curve is also observed, which we attribute to ‘hot-band transitions’ or I^- ($m/z = 127$) formation from iodine containing contaminations. The thermochemical threshold for the hydrogen loss, calculated at the B3LYP D3BJ/aug-cc-pVTZ level of theory, is found to be 0.82 eV, and we anticipate that this process proceeds predominantly from the partial diffuse LUMO + 2 orbital, which has some electron density on the S and H atoms. This assignment is also supported by the single contribution fit to the ion yield curve shown in Figure 9, where an excellent agreement is obtained by a fit of a single skewed Gaussian to the hydrogen loss ion yield. For completeness, a Gaussian contribution peaking at 0.2 eV is also included to reproduce the 0 eV impurity contribution. In principle, all conditions for HF formation could also proceed from the LUMO + 2; however, at these energies the hydrogen-bonded intermediate is not stable and the direct hydrogen loss prevails as the most efficient channel.

In a sense, DEA can be compared to photo dissociation as both are effectuated by a single electron occupation of previously unoccupied antibonding orbitals. In this context, we note a recent study by Marchetti et al. [34] on near ultraviolet spectroscopy and the photodissociation dynamics of 2- and 3-substituted thiophenols. There it was shown for 2-FTP that the repulsive $S-H$ $1n\sigma^*$ state crosses the $1\pi\sigma^*$ state close to its vibrational ground state. Population transfer from the π^* to the repulsive $S-H$ σ^* may thus proceed through non-adiabatic coupling above the respective vibrational ground state, but tunnelling would be required from the ground state. In the current terminology, this may offer an alternative path for HF formation from the π^* LUMO of the TNI formed in the initial attachment process.

It is clear from the current experiments and calculations that the perfluorination in PFTP, as compared to 2-FTP, does not only lower the thermochemical threshold for the HF loss in DEA, but also lowers the lowest σ^* MO below the respective π^* MOs, providing a very favorable condition for the HF loss. Potentially, this may be taken advantage of

to promote the interaction of radiosensitizers with low-energy electrons, thus increasing their efficiency.

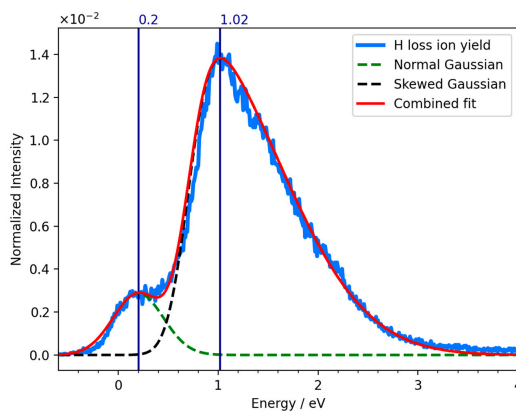


Figure 9. Single fit of a Skewed Gaussian (black dashed line) of the negative ion yield curve (blue line) for the H loss upon DEA from 2-FTP. Additionally, a Normal Gaussian peaking at 0.2 eV (green dashed line) is included to reproduce the impurity contribution at 0 eV. The red line represents the resulting fit.

3. Materials and Methods

3.1. Experimental Setup

Negative ion yield curves were recorded by means of a crossed electron-molecular beam apparatus. The experimental setup has been described in detail previously [54] and only a short description will be given here. The instrument is composed of a trochoidal electron monochromator (TEM), an effusive gas inlet system, and a quadrupole mass spectrometer (Hiden EPIC1000). The monochromator was heated to 120 °C with two internal halogen lamps to avoid condensation of the target gas on the electrical lens components. A quasi mono-energetic electron beam, generated with the TEM, crosses a molecular beam of the target gas obtained through the effusive gas inlet system. The ions resulting from the electron-molecule interactions in the collision region are then extracted through a small electric field (<1 V/cm) and analyzed by mass spectrometer. The DEA ion yield curves are recorded by scanning through the relevant electron energy at a fixed mass (m/z). The compounds were purchased from ABCR GMBH & Co. (Karlsruher, Germany), with a stated purity of 97% for PFTP and 98% for 2-FTP.

The electron energy was calibrated to the well-known 0 eV resonance for SF_6^- formation from SF_6 , and the energy resolution of the electron beam at 0 eV was determined from the FWHM and was in the range of 120–140 meV. The background pressure inside the chamber was approximately 3×10^8 mbar, while the sample gas pressure was in the range of $(2-10) \times 10^7$ mbar for PFTP and $(1-4) \times 10^6$ mbar for 2-FTP.

3.2. Theoretical Procedures

All quantum chemical calculations were carried out using ORCA version 4.2.1 [55].

Geometry optimization of all the charged fragments and neutral molecule were performed at the B3LYP [56–58] level of theory, using the aug-cc-pVTZ basis set [59,60]

and D3(BJ) dispersion correction [61,62]. For the closed shell systems, the Restricted Kohn–Sham (RKS) formalism was used, while the Unrestricted Kohn–Sham (RKS) formalism was used for open-shell systems. Harmonic vibrational frequencies were calculated at the same level of theory to derive zero-point vibrational energy (ZPVE) and thermal energy corrections. All threshold calculations refer to the single point energy of the relaxed structures, and they have been performed at the same level of theory as the geometry optimization. The reaction enthalpies at 0K (ΔH_{0K}) were calculated by subtracting the total energy of all fragments from the total energy of the parent molecule, including the respective ZPVEs. The thermally corrected thresholds (E_{th}) were obtained by subtracting the thermal energy of the parent molecule at room temperature from the reaction enthalpies at 0K.

In addition, for HF formation from PFP and PFTP, geometry optimizations and harmonic vibrational frequencies calculation were also performed at the ω B97X-D3 [61,63]/aug-cc-pVTZ level of theory, and single-point energy calculations were performed at the ω B97X-D3/aug-cc-pVQZ [59,60] and DLPNO-CCSD(T) [64–67]/aug-cc-pVQZ level on the respective ω B97X-D3 optimized geometries. In the DLPNO-CCSD(T) calculations, for open shell systems, quasi-restricted orbitals (QROs) [68] were used as a reference determinant from the UHF orbitals. ZPVEs and thermal energy correction for the neutral were obtained from the ω B97X-D3 vibrational frequencies calculation. These calculations are given as Supplementary Information in Table S1.

Vertical electron attachment energies to the virtual orbitals of PFTP and 2-FTP were calculated using the EOM-EA-CCSD method with B3LYP orbitals and aug-cc-pVTZ basis set.

The minimum energy path for the HF formation and rearrangement mechanism was calculated using the Nudged Elastic Band method with transition state (TS) optimization (NEB-TS) [69] at the B3LYP D3BJ level, using the aug-cc-pVTZ basis set. For the reactants and products, we used the optimized geometry at the B3LYP D3BJ/aug-cc-pVTZ level of theory. The transition states were checked through the calculation of harmonic vibrational frequencies, and confirmed as effective saddle points, and it was found that they had only one negative frequency (imaginary mode).

Generally, basis set superposition errors (BSSE) are small in DFT as compared to methods based on wave-function theory (WFT), due to the lower basis set sensitivity. With respect to the current study, such errors are well within the experimental energy resolution and are not taken into account.

Finally, neither spin orbit coupling nor relativistic effects were taken into account. These effects are small for the current systems and well within the limit of our experimental accuracy.

4. Conclusions

Here we presented a combined theoretical and experimental study on DEA in relation to PFTP and 2-FTP, exploring the influence of perfluorination on the susceptibility of these compounds to DEA. We reported the energy dependence of the relative DEA cross-sections for the observed fragments and the thermochemical thresholds calculated for the respective DEA processes, as well as the reaction paths computed for the formation of neutral HF up on DEA to these compounds. We also showed the nature of the LUMOs involved in the initial electron attachment process and the respective transitions energies.

We found that the perfluorination in PFTP, as compared to 2-FTP, influences significantly the DEA processes. While the dominant DEA channel in PFTP is the HF loss, direct H loss is the dominating DEA process in 2-FTP, and HF loss is insignificant. We attribute this to the exothermic nature of the HF formation from PFTP, provided not only by the energy gain through the HF formation, but also by the perfluorination. Hence, the perfluorination increases the electron affinity of the charge-retaining fragment, providing additional energy in the process. This is reflected in the respective ion yield curve for the HF loss from PFTP, which is characterized by high relative cross sections already at the 0 eV threshold. In fact, it is 5 orders of magnitude higher than the relative cross section for HF formation from

2-FTP. The key point here is that, due to the very high electron attachment cross sections at very low energies, DEA may be made very efficient by tailoring exothermic reaction channels into the respective molecules. The perfluorination also influences the molecular orbital structure, and specifically the energy ordering of the lowest lying MOs. This is due to the dominating inductive effect of fluorine providing significantly stronger stabilization for the lowest lying σ^* orbitals than the respective π^* orbitals. This is very important with respect to the DEA efficiency as effective coupling of the lowest lying orbitals with the respective dissociation coordinates is essential for DEA to be effective at low electron attachment energies. For PFTP, this is provided because the lowest lying virtual orbital is of a σ^* character, it is anti-bonding along the C–F and C–S coordinates and is polarized along the S–H bond. Hence, single electron occupation of this orbital provides all prerequisites for “direct” HF formation at very low attachment energies. The two lowest lying virtual MOs of 2-FTP, on the other hand, are antibonding π^* orbitals. Different from the direct HF formation from single electron occupation of the σ^* LUMO in PFTP, this process is symmetrically forbidden from these π^* orbitals and requires effective $\pi^*-\sigma^*$ coupling to proceed. Aided by the slight endothermicity, this puts relaxation through dissociation at a disadvantage compared to relaxation through re-emission of the electron, rendering the low energy DEA processes for 2-FTP inefficient as compared to PFTP.

It is clear from the current study, as well as from many previous DEA studies in the literature, that perfluorination enhances the susceptibility of many compounds towards low energy electrons, and rearrangement reactions such as HF formation may be used to open up exothermic DEA channels. In the context of the role of DEA in the functionality of radio sensitizers, these may be seen as important tools to promote efficient DEA reactions at low electron energies, and we argue that such tools may be valuable for a bottom-up approach in the design of efficient radiosensitizers.

Supplementary Materials: The following supporting information can be downloaded at: <https://www.mdpi.com/article/10.3390/ijms23052430/s1>.

Author Contributions: Conceptualization, M.C. and O.I.; methodology, M.C. and O.I.; validation, M.C. and O.I.; investigation, M.C. and O.I.; resources, O.I.; experimental data acquisition, M.C.; data curation, M.C.; theoretical calculations, M.C.; writing—original draft preparation, M.C.; writing—review and editing, M.C. and O.I.; visualization, M.C.; supervision, O.I.; funding acquisition, O.I. All authors have read and agreed to the published version of the manuscript.

Funding: M.C. and O.I. acknowledge support from the Icelandic Center of Research (RANNIS), grant no. 13049305(1–3). M.C. acknowledges a doctoral grant from the University of Iceland Research Fund.

Institutional Review Board Statement: Not applicable.

Informed Consent Statement: Not applicable.

Data Availability Statement: The data underlying this article will be shared on reasonable request from the corresponding author.

Conflicts of Interest: The authors declare no conflict of interest.

References

1. Boudaiffa, B.; Cloutier, P.; Hunting, D.; Huels, M.A.; Sanche, L. Resonant Formation of DNA Strand Breaks by Low-Energy (3 to 20 eV) Electrons. *Science* **2000**, *287*, 1658–1660. [[CrossRef](#)] [[PubMed](#)]
2. Kumar, A.; Becker, D.; Adhikary, A.; Sevilla, M.D. Reaction of Electrons with DNA: Radiation Damage to Radiosensitization. *Int. J. Mol. Sci.* **2019**, *20*, 3998. [[CrossRef](#)] [[PubMed](#)]
3. Ameixa, J.; Arthur-Baidoo, E.; Meißner, R.; Makurat, S.; Kozak, W.; Butowska, K.; Ferreira da Silva, F.; Rak, J.; Denifl, S. Low-energy electron-induced decomposition of 5-trifluoromethanesulfonyl-uracil: A potential radiosensitizer. *J. Chem. Phys.* **2018**, *149*, 164307. [[CrossRef](#)]
4. Meißner, R.; Feketeová, L.; Bayer, A.; Limão-Vieira, P.; Denifl, S. Formation of negative and positive ions in the radiosensitizer nimorazole upon low-energy electron collisions. *J. Chem. Phys.* **2021**, *154*, 074306. [[CrossRef](#)] [[PubMed](#)]
5. Tanzer, K.; Feketeová, L.; Puschnigg, B.; Scheier, P.; Illenberger, E.; Denifl, S. Reactions in Nitroimidazole Triggered by Low-Energy (0–2 eV) Electrons: Methylation at N1-H Completely Blocks Reactivity. *Angew. Chem. Int. Ed.* **2014**, *53*, 12240–12243. [[CrossRef](#)]

6. Ribar, A.; Fink, K.; Probst, M.; Huber, S.E.; Feketeová, L.; Denifl, S. Isomer Selectivity in Low-Energy Electron Attachment to Nitroimidazoles. *Chem. A Eur. J.* **2017**, *23*, 12892–12899. [[CrossRef](#)] [[PubMed](#)]
7. Harris, A.L. Hypoxia—A key regulatory factor in tumour growth. *Nat. Rev. Cancer* **2002**, *2*, 38–47. [[CrossRef](#)]
8. Hockel, M.; Vaupel, P. Tumor Hypoxia: Definitions and Current Clinical, Biologic, and Molecular Aspects. *JNCI J. Natl. Cancer Inst.* **2001**, *93*, 266–276. [[CrossRef](#)]
9. Wojtkowiak, J.W.; Verdusco, D.; Schramm, K.J.; Gillies, R.J. Drug Resistance and Cellular Adaptation to Tumor Acidic pH Microenvironment. *Mol. Pharm.* **2011**, *8*, 2032–2038. [[CrossRef](#)]
10. Graham, K.; Unger, E. Overcoming tumor hypoxia as a barrier to radiotherapy, chemotherapy and immunotherapy in cancer treatment. *Int. J. Nanomed.* **2018**, *13*, 6049–6058. [[CrossRef](#)]
11. Bonnet, M.; Hong, C.R.; Wong, W.W.; Liew, L.P.; Shome, A.; Wang, J.; Gu, Y.; Stevenson, R.J.; Qi, W.; Anderson, R.F.; et al. Next-Generation Hypoxic Cell Radiosensitizers: Nitroimidazole Alkylsulfonamides. *J. Med. Chem.* **2018**, *61*, 1241–1254. [[CrossRef](#)] [[PubMed](#)]
12. Wardman, P. Chemical Radiosensitizers for Use in Radiotherapy. *Clin. Oncol.* **2007**, *19*, 397–417. [[CrossRef](#)] [[PubMed](#)]
13. Park, Y.; Polska, K.; Rak, J.; Wagner, J.R.; Sanche, L. Fundamental Mechanisms of DNA Radiosensitization: Damage Induced by Low-Energy Electrons in Brominated Oligonucleotide Trimers. *J. Phys. Chem. B* **2012**, *116*, 9676–9682. [[CrossRef](#)] [[PubMed](#)]
14. Pimblott, S.M.; LaVerne, J.A. Production of low-energy electrons by ionizing radiation. *Radiat. Phys. Chem.* **2007**, *76*, 1244–1247. [[CrossRef](#)]
15. Farhataziz; Rodgers, M.A.J. *Radiation Chemistry—Principles and Applications*; VCH: New York, NY, USA, 1987.
16. Ingólfsson, O. Low Energy Electron-Induced Dissociation. In *Low-Energy Electrons*; Jenny Stanford Publishing: Delhi, India, 2019; pp. 47–120.
17. Christophorou, L.G.; Olthoff, J.K. Electron interactions with plasma processing gases: Present status and future needs. *Appl. Surf. Sci.* **2002**, *192*, 309–326. [[CrossRef](#)]
18. Kohanoff, J.; McAllister, M.; Tribello, G.A.; Gu, B. Interactions between low energy electrons and DNA: A perspective from first-principles simulations. *J. Phys. Condens. Matter* **2017**, *29*, 383001. [[CrossRef](#)]
19. Alizadeh, E.; Orlando, T.M.; Sanche, L. Biomolecular Damage Induced by Ionizing Radiation: The Direct and Indirect Effects of Low-Energy Electrons on DNA. *Annu. Rev. Phys. Chem.* **2015**, *66*, 379–398. [[CrossRef](#)]
20. Baccarelli, I.; Bald, I.; Gianturco, F.A.; Illenberger, E.; Kopyra, J. Electron-induced damage of DNA and its components: Experiments and theoretical models. *Phys. Rep.* **2011**, *508*, 1–44. [[CrossRef](#)]
21. Bald, I.; Denifl, S. The Role of Low-Energy Electrons in DNA Radiation Damage. In *Low-Energy Electrons*; Jenny Stanford Publishing: Delhi, India, 2019; pp. 285–340, ISBN 9780429058820.
22. Flosadóttir, H.D.; Ómarsson, B.; Bald, I.; Ingólfsson, O. Metastable decay of DNA components and their compositions—A perspective on the role of reactive electron scattering in radiation damage. *Eur. Phys. J. D* **2012**, *66*, 13. [[CrossRef](#)]
23. Scheer, A.M.; Aflatooni, K.; Gallup, G.A.; Burrow, P.D. Bond Breaking and Temporary Anion States in Uracil and Halouracils: Implications for the DNA Bases. *Phys. Rev. Lett.* **2004**, *92*, 068102. [[CrossRef](#)]
24. Rackwitz, J.; Kopyra, J.; Dabkowska, I.; Ebel, K.; Ranković, M.L.; Milosavljević, A.R.; Bald, I. Sensitizing DNA towards Low-Energy Electrons with 2-Fluoroadenine. *Angew. Chem. Int. Ed.* **2016**, *55*, 10248–10252. [[CrossRef](#)] [[PubMed](#)]
25. Kopyra, J.; Keller, A.; Bald, I. On the role of fluoro-substituted nucleosides in DNA radiosensitization for tumor radiation therapy. *RSC Adv.* **2014**, *4*, 6825. [[CrossRef](#)]
26. Lawrence, T.S.; Davis, M.A.; Maybaum, J.; Stetson, P.L.; Ensminger, W.D. The effect of single versus double-strand substitution on halogenated pyrimidine-induced radiosensitization and DNA strand breakage in human tumor cells. *Radiat. Res.* **1990**, *123*, 192–198. [[CrossRef](#)] [[PubMed](#)]
27. McGinn, C.J.; Shewach, D.S.; Lawrence, T.S. Radiosensitizing Nucleosides. *JNCI J. Natl. Cancer Inst.* **1996**, *88*, 1193–1203. [[CrossRef](#)]
28. Nitsche, M.; Christiansen, H.; Lederer, K.; Griesinger, F.; Schmidberger, H.; Pradier, O. Fludarabine combined with radiotherapy in patients with locally advanced NSCLC lung carcinoma: A phase I study. *J. Cancer Res. Clin. Oncol.* **2012**, *138*, 1113–1120. [[CrossRef](#)]
29. Grégoire, V.; Ang, K.K.; Rosier, J.-F.; Beauvain, M.; Garden, A.S.; Hamoir, M.; Hittelman, W.N.; Humblet, Y.; Khuri, F.R.; Milas, L.; et al. A phase I study of fludarabine combined with radiotherapy in patients with intermediate to locally advanced head and neck squamous cell carcinoma. *Radiother. Oncol.* **2002**, *63*, 187–193. [[CrossRef](#)]
30. Ómarsson, B.; Bjarnason, E.H.; Ingólfsson, O.; Haughey, S.; Field, T.A. Chemical control through dissociative electron attachment—A study on pentafluorotoluene, pentafluoroaniline and pentafluorophenol. *Chem. Phys. Lett.* **2012**, *539*–540, 7–10. [[CrossRef](#)]
31. Ómarsson, B.; Bjarnason, E.H.; Haughey, S.A.; Field, T.A.; Abramov, A.; Klüpfel, P.; Jónsson, H.; Ingólfsson, O. Molecular rearrangement reactions in the gas phase triggered by electron attachment. *Phys. Chem. Chem. Phys.* **2013**, *15*, 4754. [[CrossRef](#)]
32. Ómarsson, B.; Björnsson, R.; Ingólfsson, O. Proton Shuttling and Reaction Paths in Dissociative Electron Attachment to *o*- and *p*-Tetrafluorohydroquinone, an Experimental and Theoretical Study. *J. Phys. Chem. A* **2017**, *121*, 5580–5585. [[CrossRef](#)]
33. Dabkowska, I.; Flosadóttir, H.D.; Orzol, M.; Ptasinska, S.; Bald, I.; Ingólfsson, O.; Illenberger, E. Reactions in gas phase and condensed phase C6F5X (X = NCO, CH2CN) triggered by low energy electrons. *Phys. Chem. Chem. Phys.* **2009**, *11*, 5323. [[CrossRef](#)]

34. Marchetti, B.; Karsili, T.N.V.; Cipriani, M.; Hansen, C.S.; Ashfold, M.N.R. The near ultraviolet photodissociation dynamics of 2- and 3-substituted thiophenols: Geometric vs. electronic structure effects. *J. Chem. Phys.* **2017**, *147*, 013923. [[CrossRef](#)] [[PubMed](#)]
35. Klar, D.; Ruf, M.-W.; Hotop, H. Dissociative electron attachment to CCl₄ molecules at low electron energies with meV resolution. *Int. J. Mass Spectrom.* **2001**, *205*, 93–110. [[CrossRef](#)]
36. Sanche, L.; Schulz, G.J. Electron transmission spectroscopy: Resonances in triatomic molecules and hydrocarbons. *J. Chem. Phys.* **1973**, *58*, 479–493. [[CrossRef](#)]
37. Chowdhury, S.; Grimsrud, E.P.; Heinis, T.; Kebarle, P. Electron affinities of perfluorobenzene and perfluorophenyl compounds. *J. Am. Chem. Soc.* **1986**, *108*, 3630–3635. [[CrossRef](#)]
38. Hinde, A.L.; Poppinger, D.; Radom, L. Ab initio study of the benzene radical anion. *J. Am. Chem. Soc.* **1978**, *100*, 4681–4685. [[CrossRef](#)]
39. Birch, A.J.; Hinde, A.L.; Radom, L. A theoretical approach to the Birch reduction. Structures and stabilities of the radical anions of substituted benzenes. *J. Am. Chem. Soc.* **1980**, *102*, 3370–3376. [[CrossRef](#)]
40. Jordan, K.D.; Michejda, J.A.; Burrow, P.D. Electron transmission studies of the negative ion states of substituted benzenes in the gas phase. *J. Am. Chem. Soc.* **1976**, *98*, 7189–7191. [[CrossRef](#)]
41. Christophorou, L.G.; McCorkle, D.L.; Carter, J.G. Compound-negative-ion-resonant states and threshold-electron-excitation spectra of monosubstituted benzene derivatives. *J. Chem. Phys.* **1974**, *60*, 3779–3786. [[CrossRef](#)]
42. Brundle, C.R.; Robin, M.B.; Kuebler, N.A.; Basch, H. Perfluoro effect in photoelectron spectroscopy. I. Nonaromatic molecules. *J. Am. Chem. Soc.* **1972**, *94*, 1451–1465. [[CrossRef](#)]
43. Brundle, C.R.; Robin, M.B.; Kuebler, N.A. Perfluoro effect in photoelectron spectroscopy. II. Aromatic molecules. *J. Am. Chem. Soc.* **1972**, *94*, 1466–1475. [[CrossRef](#)]
44. Yim, M.B.; Wood, D.E. Free radicals in an adamantane matrix. XII. EPR and INDO study of $\sigma^*-\pi^*$ crossover in fluorinated benzene anions. *J. Am. Chem. Soc.* **1976**, *98*, 2053–2059. [[CrossRef](#)]
45. Wang, J.T.; Williams, F. ¹³C Hyperfine interaction in the hexafluorobenzene radical anion. *Chem. Phys. Lett.* **1980**, *71*, 471–475. [[CrossRef](#)]
46. Hitchcock, A.P.; Fischer, P.; Gedanken, A.; Robin, M.B. Antibonding σ^* valence MOs in the inner-shell and outer-shell spectra of the fluorobenzenes. *J. Phys. Chem.* **1987**, *91*, 531–540. [[CrossRef](#)]
47. Shchegoleva, L.N.; Bilkis, I.I.; Schastnev, P.V. Geometrical and electronic structure of fluoro-substituted benzene radical anions based on quantum chemical analysis of hyperfine interactions. *Chem. Phys.* **1983**, *82*, 343–353. [[CrossRef](#)]
48. Shchegoleva, L.N.; Beregovaya, I.V.; Schastnev, P.V. Potential energy surface of C₆F₆⁻ radical anion. *Chem. Phys. Lett.* **1999**, *312*, 325–332. [[CrossRef](#)]
49. Yim, M.B.; DiGregorio, S.; Wood, D.E. Free radicals in an adamantane matrix. 13. Electron paramagnetic resonance study of $\sigma^*-\pi^*$ orbital crossover in fluorinated pyridine anions. *J. Am. Chem. Soc.* **1977**, *99*, 4260–4263. [[CrossRef](#)]
50. Skalický, T.; Chollet, C.; Pasquier, N.; Allan, M. Properties of the π^* and σ^* states of the chlorobenzene anion determined by electron impact spectroscopy. *Phys. Chem. Chem. Phys.* **2002**, *4*, 3583–3590. [[CrossRef](#)]
51. Schulz, G.J.; Asundi, R.K. Isotope Effect in the Dissociative Attachment in H₂ at Low Energy. *Phys. Rev.* **1967**, *158*, 25–29. [[CrossRef](#)]
52. Krishnakumar, E.; Denifl, S.; Čadež, I.; Markelj, S.; Mason, N.J. Dissociative Electron Attachment Cross Sections for H₂ and D₂. *Phys. Rev. Lett.* **2011**, *106*, 243201. [[CrossRef](#)]
53. Newville, M.; Stensitzki, T.; Allen, D.B.; Ingargiola, A. LMFIT: Non-Linear Least-Square Minimization and Curve-Fitting for Python (0.8.0). *Zenodo* **2014**. [[CrossRef](#)]
54. Bjarnason, E.H.; Ómarsson, B.; Engmann, S.; Ómarsson, F.H.; Ingólfsson, O. Dissociative electron attachment to titanium tetrachloride and titanium tetraisopropoxide. *Eur. Phys. J. D* **2014**, *68*, 121. [[CrossRef](#)]
55. Neese, F. Software update: The ORCA program system, version 4.0. *WIREs Comput. Mol. Sci.* **2018**, *8*, e1327. [[CrossRef](#)]
56. Becke, A.D. Density-functional thermochemistry. III. The role of exact exchange. *J. Chem. Phys.* **1993**, *98*, 5648–5652. [[CrossRef](#)]
57. Lee, C.; Yang, W.; Parr, R.G. Development of the Colle-Salvetti correlation-energy formula into a functional of the electron density. *Phys. Rev. B* **1988**, *37*, 785–789. [[CrossRef](#)]
58. Stephens, P.J.; Devlin, F.J.; Chabalowski, C.F.; Frisch, M.J. Ab Initio Calculation of Vibrational Absorption and Circular Dichroism Spectra Using Density Functional Force Fields. *J. Phys. Chem.* **1994**, *98*, 11623–11627. [[CrossRef](#)]
59. Kendall, R.A.; Dunning, T.H.; Harrison, R.J. Electron affinities of the first-row atoms revisited. Systematic basis sets and wave functions. *J. Chem. Phys.* **1992**, *96*, 6796–6806. [[CrossRef](#)]
60. Woon, D.E.; Dunning, T.H. Gaussian basis sets for use in correlated molecular calculations. III. The atoms aluminum through argon. *J. Chem. Phys.* **1993**, *98*, 1358–1371. [[CrossRef](#)]
61. Grimme, S.; Antony, J.; Ehrlich, S.; Krieg, H. A consistent and accurate ab initio parametrization of density functional dispersion correction (DFT-D) for the 94 elements H-Pu. *J. Chem. Phys.* **2010**, *132*, 154104. [[CrossRef](#)] [[PubMed](#)]
62. Grimme, S.; Ehrlich, S.; Goerigk, L. Effect of the damping function in dispersion corrected density functional theory. *J. Comput. Chem.* **2011**, *32*, 1456–1465. [[CrossRef](#)] [[PubMed](#)]
63. Chai, J.-D.; Head-Gordon, M. Long-range corrected hybrid density functionals with damped atom–atom dispersion corrections. *Phys. Chem. Chem. Phys.* **2008**, *10*, 6615. [[CrossRef](#)]

64. Riplinger, C.; Neese, F. An efficient and near linear scaling pair natural orbital based local coupled cluster method. *J. Chem. Phys.* **2013**, *138*, 034106. [[CrossRef](#)]
65. Riplinger, C.; Pinski, P.; Becker, U.; Valeev, E.F.; Neese, F. Sparse maps—A systematic infrastructure for reduced-scaling electronic structure methods. II. Linear scaling domain based pair natural orbital coupled cluster theory. *J. Chem. Phys.* **2016**, *144*, 024109. [[CrossRef](#)]
66. Riplinger, C.; Sandhoefer, B.; Hansen, A.; Neese, F. Natural triple excitations in local coupled cluster calculations with pair natural orbitals. *J. Chem. Phys.* **2013**, *139*, 134101. [[CrossRef](#)]
67. Saitow, M.; Becker, U.; Riplinger, C.; Valeev, E.F.; Neese, F. A new near-linear scaling, efficient and accurate, open-shell domain-based local pair natural orbital coupled cluster singles and doubles theory. *J. Chem. Phys.* **2017**, *146*, 164105. [[CrossRef](#)]
68. Neese, F. Importance of Direct Spin–Spin Coupling and Spin-Flip Excitations for the Zero-Field Splittings of Transition Metal Complexes: A Case Study. *J. Am. Chem. Soc.* **2006**, *128*, 10213–10222. [[CrossRef](#)]
69. Ásgerðsson, V.; Birgisson, B.O.; Björnsson, R.; Becker, U.; Neese, F.; Riplinger, C.; Jónsson, H. Nudged Elastic Band Method for Molecular Reactions Using Energy-Weighted Springs Combined with Eigenvector Following. *J. Chem. Theory Comput.* **2021**, *17*, 4929–4945. [[CrossRef](#)]

Supplementary Information

Table S1. Calculated thermally corrected thresholds of HF formation upon DEA to PFP and PFTP. The calculations are performed at the ω B97X-D3/ aug-cc-Pvtz, ω B97X-D3/ aug-cc-pVQZ and DLPNO-CCSD(T) aug-cc-pVQZ levels of theory. Geometry optimization was carried out at the ω B97X-D3/ aug-cc-pVTZ. ZPVEs and thermal energy correction for the parent neutral molecule were obtained from the frequencies calculation performed at the same level of theory that was used for the optimization.

Fragment	ω B97X-D3/ aug-cc-pVTZ	ω B97X-D3/ aug-cc-pVQZ	DLPNO-CCSD(T)/ aug-cc-pVQZ
PFP			
[M - HF]/C ₃ F ₄ CO *	-0.45	-0.45	-0.50
[M - HF]/C ₃ F ₄ O	-0.047	-0.050	-0.18
PFTP			
[M - HF]/C ₃ F ₄ CS *	-0.21	-0.23	-0.35
[M - HF]/C ₃ F ₄ S	-0.16	-0.16	-0.34

* Calculated threshold considering the rearrangement of the ring after the HF formation

Article IV

HF and CO₂ loss from pentafluorobenzoic acid upon Dissociative Electron Attachment.

Maicol Cipriani and Oddur Ingólfsson

Submitted to the International Journal of Molecular Sciences for possible open access publication

This is an open access article distributed under the Creative Commons Attribution License CC BY 4.0

Maicol Cipriani actively participated in developing the research concept and carried out measurements. He conducted all computational work and a major part of data analysis. He wrote the first draft of the manuscript and contributed to editing until publication

HF and CO₂ loss from pentafluorobenzoic acid upon Dissociative Electron Attachment.Maicol Cipriani ¹ and Oddur Ingólfsson ^{1,*}¹ Department of Chemistry and Science Institute, University of Iceland, Dunhagi 3, 107 Reykjavik, Iceland; mac31@hi.is; odduring@hi.is

* Correspondence: odduring@hi.is

Copyright: © 2022 by the authors. Submitted for possible open access publication under the terms and conditions of the Creative Commons Attribution (CC BY) license (<https://creativecommons.org/licenses/by/4.0/>).

Abstract: Radiosensitizers reactions with low energy electrons, generated within malignant tissue in radiotherapy, may play a significant role in the efficacy of chemoradiotherapy. Specifically, in situ dissociative electron attachment (DEA) to such radiosensitizers may cause effective fragmentation and the formation of reactive species that, in turn, may cause DNA damage and cell death. In the current study we explore the potential of sensitizing molecular systems towards DEA, using the model compound pentafluoro benzoic acid. Dissociative electron attachment is studied experimentally and quantum chemical calculations are used to determine the threshold energies for the observed processes and to explore the vertical attachment energies and underlying orbital structures. We find that perfluorination significantly alters the fragmentation pattern of benzoic acid and enables efficient HF and CO₂ loss at very low attachment energies, leading to the formation of the complementary radical and closed shell anions. The efficiency of these processes is discussed in context to the respective thermochemistry and orbital structure and in the context of the potential of fluorination as means to tailor effective radiosensitizers.

1. Introduction

The interaction of low-energy electrons with biologically relevant molecules has caught significant attention since the benchmark work by Abdoul-Carime, H. et al. [1] showed that low energy electrons, generated by high energy radiation, are capable of causing single and double strand breaks in DNA. This is of high relevance as DNA damage through high-energy radiation can cause cancer, but also as high-energy radiation is used in both radiotherapy and chemoradiation therapy of such malignance. In the interaction of high energy radiation with biological tissues low-energy electrons (LEEs) are produced through ionizing processes. The energy distribution of these LEEs (<20 eV) peaks at or below 10 eV with an appreciable contribution close to 0 eV, and a tail extending to higher energies [2,3]. At these low energies single and double-strand breaks are induced through dissociative electron attachment (DEA)[4], and the same process can be very efficient in inducing fragmentation of electron-affinic radiosensitizers, which in turn yields radical species that can damage DNA [5,6]. It is thus of interest to explore means to enhance the sensitivity of radiosensitizers towards fragmentation through DEA as a potential path to increase their sensitivity.

The formation and decay of negative ion resonances in benzene and its derivatives under single collision conditions and in clusters has been the subject of a number of studies in the past decades, e.g., [7–14]. Of special interest in this context is the influence of substitution at the

aromatic ring on the susceptibility of these molecular entities to fragmentation up on their interaction with low energy electrons, i.e., dissociative electron attachment [7–12]. In that context, Zawadzki et al. [15], pointed out that the fragmentation mechanism of an aromatic ring molecule, under low-energy electron interactions, can be strongly influenced by the nature of the substitution at the ring. In that study the authors investigated DEA to the native benzoic acid (BA) -the aromatic benzene ring with a carboxylic acid group. They found five main dissociation channels, $[M-H]^-$, $C_6H_5^-$, OH^- , $COOH^-$, and O^- , which are all related to the fragmentation of the $COOH$ group. The influence of perfluorination of substituted benzenes has also been studied in this context, specifically the perfluorination of the ring along with single substitution [7–10]. Through the strong inductive effect of the fluorine as compared to its mesomeric effect, fluorination stabilizes the lowest lying σ^* MO stronger than the π^* ground state and in perfluorinated benzene, C_6F_6 , the lowest virtual MO is found to be the σ^* MO as compared to the π^* LUMO in the native benzene [16]. This also applies to other aromatic systems as has been observed in heavily fluorinated pyridine anions [17]. With respect to DEA such $\pi^*-\sigma^*$ inversion may be of significance as the energetically lowest dissociation channels are mostly associated with the loss of a substituent along the respective σ^* coordinate. Such a dissociation may proceed directly through single electron occupation of the respective σ^* orbital while it is symmetry forbidden from the respective π^* orbitals at the ring, requiring effective $\pi^*-\sigma^*$ coupling for the process to proceed. This is important as the survival probability of the transient negative ion (TNI) in DEA is given by $e^{-t/\tau_{AD}}$, [18,19] whereby τ_{AD} is the autodetachment lifetime. Thus, any delay in the dissociation process from the vertical attachment point, i.e., longer dissociation time (t) favors relaxation of TNI through re-emission of the electron (autodetachment) over dissociation. The thermochemical threshold is also determining for the efficiency of the DEA processes as at electron energies close to 0 eV the initial attachment cross section is inversely dependent to $e^{1/2}$, i.e., the square root of the attachment energy [20]. Hence, relaxation through dissociation is most efficient for TNI with open, direct exothermic channels that may already proceed at threshold i.e., at 0 eV incident electron energy. This has been demonstrated for the pentafluoro-substituted derivatives, C_6F_5X with $X = Cl, Br, \text{ and } I$, in which case the dissociation of the TNI along the C_6F_5-X coordinate is exothermic for $X = I$, close to thermochemical neutral for Br and endothermic for Cl . In both C_6F_5Cl and C_6F_5Br under single collision conditions, the metastable parent anion is observed within the mass spectrometric time scale of microseconds as well as the DEA channels $C_6H_5^- + X$ and $C_6H_5 + X^-$. In C_6F_5I , where the thermochemical threshold is lower, however, only the decay products are observed within this time [9,10].

DEA processes can also involve the rupture and formation of multiple bonds. In that case, generation of new chemical bonds can additionally affect the fragmentation mechanism. In recent years, several studies have been conducted on dissociative electron attachment (DEA) reactions leading to neutral HF formation from substituted benzenes [21–24]. The formation of HF feeds 5.9 eV to the system and can promote reaction channels that involve the rupture of multiple bonds already at about 0 eV incident electron energy. In this process, the polarization of the $X-H$ plays an important role through the intramolecular hydrogen bond $X-H \cdots F$. Benzene derivatives have a wide range of applications in biology and pharmacology [25,26]. The interaction of low-energy electrons with ring molecules also plays an important role in radiotherapy and chemoradiation therapy, where high-energy radiation applied to biological tissues produces low-energy electrons (LEEs). In this contribution we extend previous DEA

studies on benzoic acid to pentafluorobenzoic (PFBA), a good candidate for HF formation. We report the partial DEA cross-section for the main reaction channels, and we explore the effect of perfluorination on the nature of the SOMOs involved in the initial electron attachment process. We further discuss our findings in the context of HF formation in DEA as a potential path to increase the efficacy of radiosensitizers applied in chemoradiotherapy.

2. Results

Figure 1 shows the relative cross-sections for the most efficient DEA channels observed in dissociative electron attachment to pentafluorobenzoic acid (PFBA) in the energy range from about 0 eV to 10 eV. These are the loss of neutral HF leading to the formation of $[M - HF]^-$ (m/z 192), the neutral CO_2 loss leading to the formation of $[M - CO_2]^-$ (m/z 184) and loss of both HF and CO_2 leading to the formation of $[M - HF - CO_2]^-$ (m/z 164). For better comparison, the relative cross sections are normalized with respect to the target gas pressure and the relative intensity of SF_6^- formation from SF_6 at 0 eV incident electron energy recorded before each measurement. Hydrogen loss is also observed (not shown here), but with about four orders of magnitude lower intensity, when compared to that of $[M - HF - CO_2]^-$, and peaking at around 1 eV.

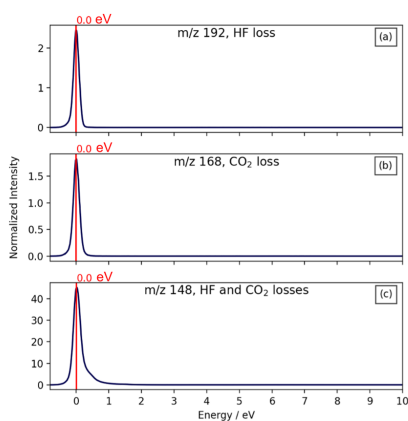


Figure 1. DEA ion yield curves from PFBA for the channels: (a) H loss, (b) HF loss, and (c) SH loss. The intensities are normalized with respect to the target gas pressure and the formation of SF_6^- from SF_6 at 0 eV incident electron energy.

All the curves show a pronounced peak at or close to 0 eV. On the contrary, in the previous study on DEA to BA [15], with the exception of the ion yield curve for H loss peaking at around 1.34 eV, all other ion yield curves peak at energies above 5 eV. In that study, the ion yield curve for the $[M - H]^-$ shows the highest intensity. The second highest intense fragment observed in DEA to BA is attributed to the loss of the carboxylic acid from the aromatic ring, i.e., the formation of $[M - COOH]^-$. Also, the complementary DEA channel, the formation of $COOH^-$ is observed in DEA to BA.

In the current DEA to PFBA, the HF formation is significantly more efficient than the H loss (not shown here), which we attribute to the strong intramolecular hydrogen bond $COO-H \cdots F$ promoting the HF formation, while sterically hindering the direct hydrogen loss.

In DEA to PFBA, the maximum cross-section for $[M - HF - CO_2]^-$ is an order of magnitude higher than those for $[M - HF]^-$ and $[M - CO_2]^-$. Furthermore, the $[M - HF - CO_2]^-$ ion yield curve is broader with a shoulder towards higher energies while such high energy contribution is not observed in the ion yields for $[M - HF]^-$ and $[M - CO_2]^-$. We attribute this contribution to a second low energy resonance contributing to the $[M - HF - CO_2]^-$ ion yield as is visualized with a combined fit of a normal Gaussian lower energy contribution and a skewed Gaussian to the higher energy contribution, shown in Figure 2. A skewed Gaussian is chosen for the higher energy contribution as the autodetachment process becomes more significant at higher energies, resulting in a lower survival probability with respect to dissociation. This, in turn, gives asymmetric peaks, tailing off towards higher energies in the DEA ion yield curves. This effect is not considered to be significant close to 0 eV, therefore a normal Gaussian for the fit of that contribution.

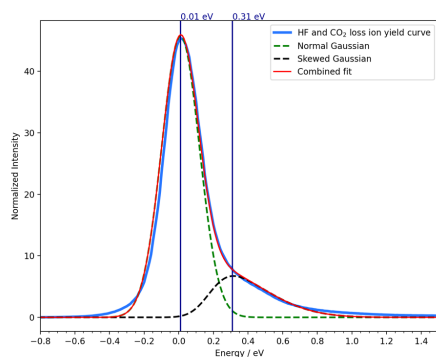
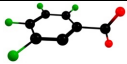


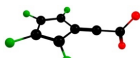
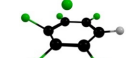
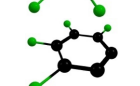
Figure 2. Combined fit of a Normal Gaussian (green dashed line) and a Skewed Gaussian (black dashed line) of the negative ion yield curve (blue line) for neutral HF and CO₂ loss upon DEA from PFTP. The resulting fit is represented by the red line.

The high intensity of the [M – HF – CO₂]⁻ contribution in the DEA ion yield from PFBA and its asymmetry towards higher energy as compared to the lower intensity and symmetric [M – HF]⁻ and [M – CO₂]⁻ contributions, can be explained considering the thermochemistry of these DEA processes. For the direct formation of [M – CO₂]⁻, [M – HF]⁻ and [M – HF – CO₂]⁻, without rearrangement of the aromatic ring, we derive thresholds of -1.48 eV, -0.81 eV and -0.21 eV, respectively, calculated at the B3LYP D3BJ/aug-cc-pVTZ level of theory. This is shown in Table 1 along with the minimum energy structure of the respective anionic fragments. Additionally, Table 1 shows the threshold value and the resulting minimum energy structure of the anionic fragment when considering rearrangement of the aromatic ring after HF loss, as will be discussed here below. In the current experiment the extraction time from the interaction region is on the order of 10 μs and the flight time through the QMS on the order of 50 μs. Thus, only DEA products are observed that are formed within the first 10 μs and are stable enough to survive the 50 μs flight through the QMS. At the 0 eV threshold, the [M – CO₂]⁻ and [M – HF]⁻ ions formed have a maximum internal energy that is 1.69 eV and 1.02 eV above the threshold for further fragmentation to [M – HF – CO₂]⁻, respectively. Thus, the excess energy in these fragments makes their survival probability low, with respect to further HF and CO₂ loss, respectively, and we attribute the [M – HF – CO₂]⁻ formation primarily to further metastable fragmentation of these fragments. With increasing incident electron energy, the survival probability is further reduced, exhibited in the rapid drop in the [M – CO₂]⁻ and [M – HF]⁻ ion yields above the 0 eV threshold and the lack of any contribution to these ion signals through the higher lying resonance.

For the HF formation we additionally considered a rearrangement of the benzene ring to a 5-membered ring with exocyclic –CCOO substituent (see Table 1). This rearrangement was proposed by Ómarsson et al. [21,22] for pentafluorophenol (PFP) to rationalize the effective HF loss from this molecule at 0 eV. For the direct HF loss, they calculated a threshold of 0.59 eV at the B2PLYP/aug-cc-pc-2 level of theory, while the rearrangement of the ring into a 5 membered ring resulted in a threshold of -0.19 eV, in better agreement with the experimental results. For PFBA, on the other hand, we find the direct HF loss to be exothermic with a threshold of -0.81 eV, while a subsequent rearrangement of the ring makes the process endothermic with a threshold of 0.54 eV.

Table 1. Calculated threshold values (ΔE_{rxn}) for the most efficient DEA processes observed along with the optimized geometries of the anions. The calculations have been performed at the B3LYP D3BJ/aug-cc-pVTZ level of theory

m/z	DEA process	Optimized geometry of the anion	ΔE_{rxn} (eV)
192	$\text{C}_6\text{F}_5\text{COOH} + e^- \rightarrow \text{C}_6\text{F}_5\text{COO}^- + \text{HF}$		-0.81

192	$C_6F_5COOH + e^- \rightarrow C_6F_5CCOO^- + HF$ ¹		0.54
168	$C_6F_5COOH + e^- \rightarrow C_6F_5H + CO_2$		-1.48
148	$C_6F_5COOH + e^- \rightarrow C_6F_4COO^- + HF + CO_2$		-0.21

¹ Calculated threshold considering the rearrangement of the ring after the HF formation.

With respect to initially formed PFBA transient negative ions formed, we find the SOMO to be of π^* character and antibonding along the C–F and C–O coordinates but not along the C–CO₂H coordinate. Adhering to Jordan et al. [14], we labelled this MO as b_1 (π^*). The SOMO+1, on the other hand, is found to be of a σ^* character, antibonding along the C–F coordinate. At the B3LYP D3BJ/aug-cc-pVTZ level of theory, the vertical attachment energy (VAE) for the anion ground state, the SOMO, was found to be –0.52 eV, while for the first excited anion state, the SOMO+1, we derived a value of 0.4 eV using a Δ SCF approach. The respective SOMOs are shown in Figure 3. In general, one would expect the perfluorination to lower the σ^* LUMO +1 of benzene below the π^* LUMO due to the strong inductive effect of fluorine. This is clearly not the case here, and we attribute that to strong coupling of the carbonyl π^* orbital with the conjugated π^* orbitals of the aromatic ring, i.e., mesomeric stabilization of the π^* orbital through the carboxylic group. Accordingly, in our combined fit of the $[M - HF - CO_2]^-$ ion yield curve, see Figure 2, we attribute the low energy contribution to the π^* SOMO while the higher lying contribution is attributed to dissociation from the σ^* SOMO+1. However, while C–F dissociation can proceed directly from the σ^* SOMO+1, it is symmetry forbidden from the SOMO in C_{2v} group. The high intensity in the $[M - HF]^-$ channel must thus be provided through effective coupling of the π^* SOMO with the σ^* C–F. In fluorinated benzene derivatives this is provided by the pseudo Jahn Teller effect [27,28].

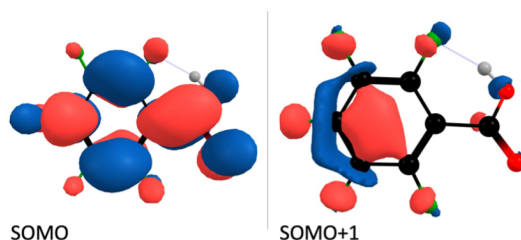


Figure 3. Contour plot of SOMO and SOMO+1 of PFBA.

Now considering the perfluorination and the enabling of HF formation in DEA as means to sensitize compounds towards low energy interaction, the comparison of the current study with the previous study on DEA to BA, clearly shows the potential of these approaches. In DEA to the native benzoic acid (BA) the main dissociation channels are hydrogen loss $[M - H]^-$, loss of the carboxylic group; $C_6H_5^-$ and $COOH^-$, and cleavage of one of the C-O bonds; O^- and OH^- , which are all related to the fragmentation of the COOH group. Though neither the current study, nor that on BA presents absolute cross sections, it is clear that with the exception of the hydrogen loss from BA, the efficiency of the fragmentation of PFBA upon DEA as compared to that of BA is significantly higher. Furthermore, in the previous BA study [15], the authors found the lowest DEA threshold, the hydrogen loss, to have a threshold of 1.02 eV, calculated at the B3LYP/aug-cc-pVTZ level of theory. At the same level of theory, they found the thresholds for the complementary DEA channels $[M - COOH]^-$ and $COOH^-$ to be 3.25 eV and 2.78 eV, respectively and for the $[M - COOH]^-$ channel, considering a further dissociation of COOH into CO_2 and H, they derived a threshold of 3.31 eV. Furthermore, the $[M - CO_2]^-$ channel, which is very efficient in DEA to PFBA, where it leads to the formation of the pentafluorobenzene radical anion, is not observed in DEA to BA. This is not surprising as the native benzene has negative electron affinity (-1.15 eV) [29,30].

As we have discussed in a previous study comparing pentafluorothiophenol and 2-fluorothiophenol [31], and demonstrated here, the combination of enabling exothermic dissociation channels and providing the prerequisites for electron attachment at 0 eV incident energy is a viable path to enhance the DEA efficiency and direct the fragmentation in a preferable way. This is based on the inverse energy dependence of the attachment cross section providing for very high values at the 0 eV threshold, in combination with opening up a doorway for relaxation through dissociation already at these very low attachment energies. We have previously demonstrated this approach in a comparative study on pentafluorothiophenol and 2-fluorothiophenol, where we argue that this may offer a viable path for rational design of effective radiosensitizers. Here we have extended these studies to a compound with a very hydrophilic substituent and though these are all model compound it is clear that their susceptibility to fragmentation through DEA may be tailored by targeted fluorination and current introduction of the carboxylic acid group further shows that other important parameters such as water solubility, and eventually tolerability may also be addressed by suitable molecular design.

4. Materials and Methods

4.1. Experimental Set up

The negative ion yield curves were recorded with a crossed electron-molecule beam apparatus. This instrument has been previously described [32], and only a brief description is given here. The instrument consists of a trochoidal electron monochromator (TEM), an effusive gas inlet system and a commercial quadrupole mass spectrometer (HIDEN EPIC 1000). The TEM generates a quasi mono-energetic electron that crosses an effusive molecular beam of the target gas. The ions formed in this collision region are extracted by applying a weak electric field (<1 V/cm) and directed to the entrance of the mass spectrometer to be analyzed. The negative ion yield curves are recorded by scanning through the electron energy at a fixed mass (m/z).

The TEM and the ion extraction elements are maintained at 120 °C during measurements to avoid target gas condensation on the electrical lens components

The typical background pressure inside the chamber is on the order of 4×10^{-8} mbar. The measurements were performed with a target gas pressure of around 2.9×10^{-7} mbar in order to assure single collision condition. The energy scale was calibrated by the well documented SF_6^- formation from SF_6 at 0 eV [33] recorded before and after each measurement. The energy resolution was estimated from the FWHM of that signal and was found to be 100–170 meV for the current measurements. Pentafluoro benzoic acid was with a stated purity of 99%, was purchased from ABCR GMBH & Co. (Karlsruher, Germany) and used as delivered.

4.2 Quantum chemical calculations

All quantum chemical calculations were performed with the quantum chemistry package ORCA 4.2.1 [34]. All the molecular geometries were optimized at the B3LYP [35–37] level of theory, using the aug-cc-pVTZ basis set [38,39] and D3(BJ) dispersion correction [40,41]. Single-point energy calculations and harmonic vibrational frequencies were calculated at the same level of theory used for the geometry optimization. The vibrational frequencies were confirmed to be positive and were used to derive the zero-point vibrational energy (ZPVE), for the neutral molecule and all the fragment, and thermal energy correction for the neutral parent molecule at 25 °C.

5. Conclusions

In the context of increasing the susceptibility of molecular entities towards low energy electron induced fragmentation, by fluorination, we have conducted a combined experimental and theoretical study on pentafluoro benzoic acid (PFBA). Specifically, we have studied the fragmentation of this model compound through dissociative electron attachment. This is an extension on our previous study where we compare low energy electron induced fragmentation of pentafluorothiophenol and 2-fluorothiophenol in the context of a bottom-up approach for rational design of more effective radiosensitizers for use in chemoradiotherapy. In DEA to PFBA we find the formation of $[\text{M} - \text{HF}]^-$, $[\text{M} - \text{CO}_2]^-$ and $[\text{M} - \text{HF} - \text{CO}_2]^-$, to be highly efficient at very low incident electron energies, i.e., at around the 0 eV threshold. At the B3LYP D3BJ/ aug-cc-pVTZ level of theory we find all these channels to be exothermic with a thermochemical threshold of -1.48 eV, -0.81 eV and -0.21 eV. While $[\text{M} - \text{HF}]^-$ and $[\text{M} - \text{CO}_2]^-$ are only observed through a narrow contribution at 0 eV, the ion yield of $[\text{M} - \text{HF} - \text{CO}_2]^-$ shows an additional higher energy contribution peaking at 0.31 eV. We attribute the low energy contribution to the π^* SOMO while the higher lying contribution is attributed to dissociation from the σ^* SOMO +1. Considering the exothermicity of these processes, the $[\text{M} - \text{HF} - \text{CO}_2]^-$ fragment is ascribed to further metastable fragmentation of $[\text{M} - \text{HF}]^-$ and $[\text{M} - \text{CO}_2]^-$ within time scale of the observation window, rather than a direct process.

In PFBA we do not observe the π^* - σ^* crossover, between the SOMO and SOMO+1, expected from the stabilization of the σ^* through the strong inductive effect of fluorine, i.e., the perfluoro effect. We attribute this to the negative mesomeric effect of the carboxylic acid group strongly stabilizes the b_1 (π^*) MO.

In the context of rational design of more effective radiosensitizers, the current study confirms the potential of HF formation and fluorination to increase the susceptibility of molecular entities to low energy electron induced fragmentation. Furthermore, the introduction of the very hydrophilic carboxylic acid group does not negatively effect these DEA channels, and may thus offer a way to increase the water solubility of such highly fluorinated compounds.

Funding: M.C. and O.I. acknowledge support from the Icelandic Center of Research (RANNIS), grant no. 185346-05 M.C. acknowledges a doctoral grant from the University of Iceland Research Fund.

References

1. Abdoul-Carime, H.; Gohlke, S.; Illenberger, E. Site-Specific Dissociation of DNA Bases by Slow Electrons at Early Stages of Irradiation. *Phys. Rev. Lett.* **2004**, *92*, 168103, doi:10.1103/PhysRevLett.92.168103.
2. LaVerne, J.A.; Pimblott, S.M. Electron Energy-Loss Distributions in Solid, Dry DNA. *Radiat. Res.* **1995**, *141*, 208, doi:10.2307/3579049.
3. Pimblott, S.M.; LaVerne, J.A. Production of low-energy electrons by ionizing radiation. *Radiat. Phys. Chem.* **2007**, *76*, 1244–1247, doi:10.1016/j.radphyschem.2007.02.012.
4. Boudaiffa, B.; Cloutier, P.; Hunting, D.; Huels, M.A.; Sanche, L. Resonant Formation of DNA Strand Breaks by Low-Energy (3 to 20 eV) Electrons. *Science (80-.)*. **2000**, *287*, 1658–1660, doi:10.1126/science.287.5458.1658.
5. Chomicz, L.; Zdrowicz, M.; Kasprzykowski, F.; Rak, J.; Buonaugurio, A.; Wang, Y.; Bowen, K.H. How to Find Out Whether a 5-Substituted Uracil Could Be a Potential DNA Radiosensitizer. *J. Phys. Chem. Lett.* **2013**, *4*, 2853–2857, doi:10.1021/jz401358w.
6. Ameixa, J.; Arthur-Baidoo, E.; Meißner, R.; Makurat, S.; Kozak, W.; Butowska, K.; Ferreira da Silva, F.; Rak, J.; Denifl, S. Low-energy electron-induced decomposition of 5-trifluoromethanesulfonyl-uracil: A potential radiosensitizer. *J. Chem. Phys.* **2018**, *149*, 164307, doi:10.1063/1.5050594.
7. Naff, W.T.; Compton, R.N.; Cooper, C.D. Attachment of Electrons to Substituted Benzenes. *J. Chem. Phys.* **1971**, *54*, 212–222, doi:10.1063/1.1674596.
8. Fenzlaff, H.-P.; Illenberger, E. Low energy electron impact on benzene and the fluorobenzenes. Formation and dissociation of negative ions. *Int. J. Mass Spectrom. Ion Process.* **1984**, *59*, 185–202, doi:10.1016/0168-1176(84)85094-6.
9. Ingólfsson, O.; Weik, F.; Illenberger, E. The reactivity of slow electrons with molecules at different degrees of aggregation: gas phase, clusters and condensed phase. *Int. J. Mass Spectrom. Ion Process.* **1996**, *155*, 1–68, doi:10.1016/S0168-1176(96)04392-3.

10. Kalcher, J. Chapter 5. Gas-phase stabilities of small anions. *Annu. Reports Sect. "C" (Physical Chem.* **1996**, *93*, 147, doi:10.1039/pc9969300147.
11. Heni, M.; Illenberger, E. Electron attachment by saturated nitriles, acrylonitrile (C₂H₃CN), and benzonitrile (C₆H₅CN). *Int. J. Mass Spectrom. Ion Process.* **1986**, *73*, 127–144, doi:10.1016/0168-1176(86)80014-3.
12. Milhaud, J. Dissociate electron attachment to monohalogenated benzenes. *Chem. Phys. Lett.* **1985**, *118*, 167–173, doi:10.1016/0009-2614(85)85291-X.
13. Christophorou, L.G.; Goans, R.E. Low-energy (< 1 eV) electron attachment to molecules in very-high pressure gases: C₆H₆. *J. Chem. Phys.* **1974**, *60*, 4244–4250, doi:10.1063/1.1680895.
14. Jordan, K.D.; Michejda, J.A.; Burrow, P.D. Electron transmission studies of the negative ion states of substituted benzenes in the gas phase. *J. Am. Chem. Soc.* **1976**, *98*, 7189–7191, doi:10.1021/ja00439a014.
15. Zawadzki, M.; Wierzbicka, P.; Kopyra, J. Dissociative electron attachment to benzoic acid (C₇H₆O₂). *J. Chem. Phys.* **2020**, *152*, 174304, doi:10.1063/1.5135383.
16. Brundle, C.R.; Robin, M.B.; Kuebler, N.A. Perfluoro effect in photoelectron spectroscopy. II. Aromatic molecules. *J. Am. Chem. Soc.* **1972**, *94*, 1466–1475, doi:10.1021/ja00760a008.
17. Yim, M.B.; DiGregorio, S.; Wood, D.E. Free radicals in an adamantane matrix. 13. Electron paramagnetic resonance study of .sigma*-.pi* orbital crossover in fluorinated pyridine anions. *J. Am. Chem. Soc.* **1977**, *99*, 4260–4263, doi:10.1002/chin.197739042.
18. Schulz, G.J.; Asundi, R.K. Isotope Effect in the Dissociative Attachment in H₂ at Low Energy. *Phys. Rev.* **1967**, *158*, 25–29, doi:10.1103/PhysRev.158.25.
19. Krishnakumar, E.; Denifl, S.; Čadež, I.; Markelj, S.; Mason, N.J. Dissociative Electron Attachment Cross Sections for H₂ and D₂. *Phys. Rev. Lett.* **2011**, *106*, 243201, doi:10.1103/PhysRevLett.106.243201.
20. Vogt, E.; Wannier, G.H. Scattering of Ions by Polarization Forces. *Phys. Rev.* **1954**, *95*, 1190–1198, doi:10.1103/PhysRev.95.1190.
21. Ómarsson, B.; Bjarnason, E.H.; Ingólfsson, O.; Haughey, S.; Field, T.A. Chemical control through dissociative electron attachment – A study on pentafluorotoluene, pentafluoroaniline and pentafluorophenol. *Chem. Phys. Lett.* **2012**, *539–540*, 7–10, doi:10.1016/j.cplett.2012.04.059.
22. Ómarsson, B.; Bjarnason, E.H.; Haughey, S.A.; Field, T.A.; Abramov, A.; Klüpfel, P.; Jónsson, H.; Ingólfsson, O. Molecular rearrangement reactions in the gas phase triggered

- by electron attachment. *Phys. Chem. Chem. Phys.* **2013**, *15*, 4754, doi:10.1039/c3cp44320e.
23. Ómarsson, B.; Björnsson, R.; Ingólfsson, O. Proton Shuttling and Reaction Paths in Dissociative Electron Attachment to o - and p -Tetrafluorohydroquinone, an Experimental and Theoretical Study. *J. Phys. Chem. A* **2017**, *121*, 5580–5585, doi:10.1021/acs.jpca.7b05010.
 24. Dąbkowska, I.; Flosadóttir, H.D.; Orzol, M.; Ptasinska, S.; Bald, I.; Ingólfsson, O.; Illenberger, E. Reactions in gas phase and condensed phase C6F5X (X = NCO, CH2CN) triggered by low energy electrons. *Phys. Chem. Chem. Phys.* **2009**, *11*, 5323, doi:10.1039/b820670h.
 25. Hansch, C.; Gao, H. Comparative QSAR: Radical Reactions of Benzene Derivatives in Chemistry and Biology. *Chem. Rev.* **1997**, *97*, 2995–3060, doi:10.1021/cr9601021.
 26. Polêto, M.D.; Rusu, V.H.; Grisci, B.I.; Dorn, M.; Lins, R.D.; Verli, H. Aromatic Rings Commonly Used in Medicinal Chemistry: Force Fields Comparison and Interactions With Water Toward the Design of New Chemical Entities. *Front. Pharmacol.* **2018**, *9*, doi:10.3389/fphar.2018.00395.
 27. Shchegoleva, L.N.; Bilkis, I.I.; Schastnev, P.V. Geometrical and electronic structure of fluoro-substituted benzene radical anions based on quantum chemical analysis of hyperfine interactions. *Chem. Phys.* **1983**, *82*, 343–353, doi:10.1016/0301-0104(83)85239-2.
 28. Shchegoleva, L.N.; Beregovaya, I.V.; Schastnev, P.V. Potential energy surface of C6F6– radical anion. *Chem. Phys. Lett.* **1999**, *312*, 325–332, doi:10.1016/S0009-2614(99)00944-6.
 29. Nenner, I.; Schulz, G.J. Temporary negative ions and electron affinities of benzene and N -heterocyclic molecules: pyridine, pyridazine, pyrimidine, pyrazine, and s -triazine. *J. Chem. Phys.* **1975**, *62*, 1747–1758, doi:10.1063/1.430700.
 30. Sanche, L.; Schulz, G.J. Electron transmission spectroscopy: Resonances in triatomic molecules and hydrocarbons. *J. Chem. Phys.* **1973**, *58*, 479–493, doi:10.1063/1.1679228.
 31. Cipriani, M.; Ingólfsson, O. HF Formation through Dissociative Electron Attachment—A Combined Experimental and Theoretical Study on Pentafluorothiophenol and 2-Fluorothiophenol. *Int. J. Mol. Sci.* **2022**, *23*, 2430, doi:10.3390/ijms23052430.
 32. Bjarnason, E.H.; Ómarsson, B.; Engmann, S.; Ómarsson, F.H.; Ingólfsson, O. Dissociative electron attachment to titatinum tetrachloride and titanium tetraisopropoxide. *Eur. Phys. J. D* **2014**, *68*, 121, doi:10.1140/epjd/e2014-50091-9.
 33. Braun, M.; Marienfeld, S.; Ruf, M.-W.; Hotop, H. High-resolution electron attachment to

- the molecules CCl₄ and SF₆ over extended energy ranges with the (EX)LPA method. *J. Phys. B At. Mol. Opt. Phys.* **2009**, *42*, 125202, doi:10.1088/0953-4075/42/12/125202.
34. Neese, F. Software update: the ORCA program system, version 4.0. *WIREs Comput. Mol. Sci.* **2018**, *8*, doi:10.1002/wcms.1327.
 35. Becke, A.D. Density-functional thermochemistry. III. The role of exact exchange. *J. Chem. Phys.* **1993**, *98*, 5648–5652, doi:10.1063/1.464913.
 36. Lee, C.; Yang, W.; Parr, R.G. Development of the Colle-Salvetti correlation-energy formula into a functional of the electron density. *Phys. Rev. B* **1988**, *37*, 785–789, doi:10.1103/PhysRevB.37.785.
 37. Stephens, P.J.; Devlin, F.J.; Chabalowski, C.F.; Frisch, M.J. Ab Initio Calculation of Vibrational Absorption and Circular Dichroism Spectra Using Density Functional Force Fields. *J. Phys. Chem.* **1994**, *98*, 11623–11627, doi:10.1021/j100096a001.
 38. Kendall, R.A.; Dunning, T.H.; Harrison, R.J. Electron affinities of the first-row atoms revisited. Systematic basis sets and wave functions. *J. Chem. Phys.* **1992**, *96*, 6796–6806, doi:10.1063/1.462569.
 39. Woon, D.E.; Dunning, T.H. Gaussian basis sets for use in correlated molecular calculations. III. The atoms aluminum through argon. *J. Chem. Phys.* **1993**, *98*, 1358–1371, doi:10.1063/1.464303.
 40. Grimme, S.; Antony, J.; Ehrlich, S.; Krieg, H. A consistent and accurate ab initio parametrization of density functional dispersion correction (DFT-D) for the 94 elements H–Pu. *J. Chem. Phys.* **2010**, *132*, 154104, doi:10.1063/1.3382344.
 41. Grimme, S.; Ehrlich, S.; Goerigk, L. Effect of the damping function in dispersion corrected density functional theory. *J. Comput. Chem.* **2011**, *32*, 1456–1465, doi:10.1002/jcc.21759.